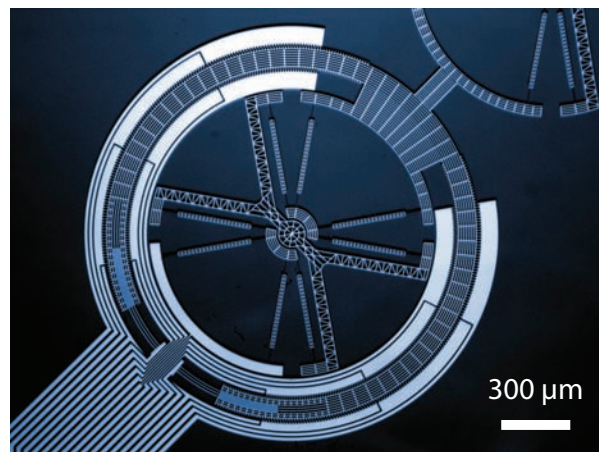


Frictionless Electrostatic Rotary Stepper Micromotor for Microrobotic Applications

MASTER THESIS (Winter 2010)
Section of Microengineering



Marc STRANCZL

Under the supervision of:
Dr. Christophe YAMAHATA, LMIS 2
Prof. Martin GIJS, LMIS 2

Submitted on January 21st, 2011

Project statement

Monolithic micromotor for microrobotic applications

Keywords: Micromotor, Flexure mechanism, Silicon-On-Insulator (SOI)

In the Laboratory of Microsystems (LMIS 2, EPFL), we have recently developed a monolithic rotary stepper micromotor in silicon. This micromotor employs a flexural suspension of the rotor to avoid mechanical friction during operation.

In this Master, we offer to pursue the current researches and use two of these 3-phase stepper micromotors as active joints for a microrobotic arm. The prototype will be fabricated by deep Reactive Ion Etching in a SOI wafer. This project will be conducted in collaboration with Dr. Edin Sarajlic (University of Twente, MESA+ Institute).

Assistant: Christophe Yamahata (LMIS 2, EPFL)

Professor: Martin Gijs (LMIS 2, EPFL)

Abstract

We present the modeling and experimental characterization of a monolithic 3-phase rotary stepper micromotor which employs a flexure suspension to guide the rotor. The monolithic structure avoids any frictional contact during operation, providing a precise, repeatable and reliable bidirectional stepping motion without feedback control.

We have performed finite element analysis (FEA) simulations of the mechanical static and dynamic properties. These studies are consistent with the extensive experimental characterization performed in the quasi-static, transient, and dynamic regimes. Dynamic nonlinearities have been observed and compared to a complete mathematical model including the electrostatic actuation and the mechanical properties of the system. The analytic model is consistent with the simulations and the experiments.

The monolithic 3-phase rotary stepper micromotor has been modified to increase its torque and we have included a differential capacitive angular sensor. The implementation of this micromotor in a microgripper has also been studied and designed. These designs have been fabricated in a single-crystal silicon, using a simple single-mask process, based on standard Silicon-On-Insulator technology.

The fabrication was performed in the cleanroom of the EPFL Center of MicroNano-Technology (CMi) and has conducted to the preliminary experimental characterization of prototypes which validated the single-mask process.

Part of the results presented in this Master Project have been published in *Proc. 24th IEEE Int. Conf. on Micro Electro Mechanical Systems (MEMS)*: M. Stranczl *et al.*, “Modal Analysis and Modeling of a Frictionless Electrostatic Rotary Stepper Micromotor”, pp. 1257-1260, Cancún, Mexico, January 23-27, 2011.

Contents

Project statement	i
Abstract	ii
1 Introduction	1
2 State of the art review	3
2.1 Flexure beams	4
2.1.1 Advantages and limitations of flexure beams	4
2.1.2 Linear guidings	6
2.1.3 Rotational flexural bearing	8
2.2 Electrostatic stepper micromotors	11
2.2.1 Micromotors for skew angle compensation in HDD	11
2.2.2 Micromotors for microrobotic applications	13
2.2.3 Initial project state	19
3 Finite Element Analysis	21
3.1 Flexural bearing simulations	22
3.1.1 Analytic model and RCC pivot simulations comparison	22
3.1.2 Analytic model and butterfly pivot simulation comparison	25
3.1.3 Silicon orthotropic properties study	27
3.1.4 Buckling simulations	28
3.2 Finite Element Modal Analysis	30
3.3 Simulation Discussion	32
4 Measurement method	33
4.1 Review of optical measurement methods	34
4.2 Polytec Micro System Analyzer (MSA-400)	35
4.3 Temporally aliased video analysis	39
4.3.1 Discrete Fourier Analysis of video recording	39
4.3.2 Aliasing and the sampling theorem	40
4.3.3 Temporally aliased video analysis	40
4.3.4 Signal and camera synchronization	42
5 Dynamic characterization of the stepper micromotor	43
5.1 Case I: Sine excitation with a DC offset	44
5.1.1 Driving signals	44

5.1.2	Experimental measurements	45
5.2	Case II: Pure sine excitation	46
5.2.1	Driving signals	46
5.2.2	Experimental measurements	47
5.2.3	Nonlinearities	48
5.3	Case III: Electrostatic stiffening	50
5.3.1	Driving signals	50
5.3.2	Experimental measurements	50
5.3.3	FEA simulations	51
6	Mathematical model of the 3-phase stepper micromotor	53
6.1	Modeling of the micromotor	54
6.1.1	Geometrical model	54
6.1.2	Actuation model	54
6.1.3	Equation of motion	56
6.1.4	Dynamic model	56
6.1.5	Energetic representation	57
6.2	Interpretation of the model using Maple 13	59
6.2.1	Equation of motion	59
6.2.2	Nondimensionalization	59
6.2.3	Numerical application	61
6.2.4	Case II: Nonlinearity simulation	61
6.2.5	Case III: Simulation of the electrostatic stiffening effect	63
6.2.6	Case I: Driving voltage simulation results	64
6.2.7	Interpretation of the results	65
6.3	Modeling conclusion	66
7	Design and fabrication of a micromotor with a differential capacitive sensor	67
7.1	Versions of the micromotors	68
7.1.1	Micromotor v.1	68
7.1.2	Micromotor v.2.0	68
7.1.3	Micromotor v.2.1	68
7.2	Design modifications	69
7.2.1	Capacitive measurement of the angular position	69
7.2.2	Design modification studies in order to increase the torque	70
7.2.3	AFM-like torque measurement	71
7.3	Potential applications and design of a demonstrator	72
7.3.1	Optical MEMS	72
7.3.2	Vertical stage for a profilometer	73
7.3.3	Monolithic planar 3-DOF parallel micromanipulator	73
7.3.4	Microgripper: Design of a demonstrator	74
7.4	Fabrication results	75
7.4.1	Micromotor v.1	75
7.4.2	Micromotor v.2.0	75
7.4.3	Microrobot fabrication results	76

7.4.4	Micromotor v.2.1	76
7.4.5	Discussion of the fabrication results	76
8	Conclusion and Outlook	77
	Acknowledgments	78
	Bibliography	80
A	Appendix	85
A.1	Influence of the rigid element on the butterfly stiffness	85
A.2	Reinforced RCC pivot stiffness	86
A.3	Silicon properties	87
A.4	Region of interest (ROI), temporally aliased video microscopy	88
A.5	High-speed camera measurement	89
A.6	Variable substitution from linear to rotational model	90
A.7	Newton's law equation	90
A.8	Nondimensionalization	91
A.9	Maple code	92
	A.9.1 Case I	92
	A.9.2 Case II	93
A.10	Micromotor dimensions	94
	A.10.1 v.1	94
	A.10.2 v.2.0	94
	A.10.3 v.2.1	95
A.11	Micromotor v.1	96
	A.11.1 Micromotor v.1	96
	A.11.2 Fabrication process considerations	97
A.12	Motor v.2	98
	A.12.1 Micromotor v.2.0	98
	A.12.2 Micromotor v.2.0 with a torque sensor	99
	A.12.3 Fabrication process considerations	100
A.13	Demonstrator	101
	A.13.1 Demonstrator design	101
	A.13.2 Fabrication process considerations	102
A.14	Micromotor v.2.1	104
	A.14.1 Micromotor v.2.1	104
	A.14.2 Micromotor v.2.1 with a torque sensor	105
	A.14.3 Differential capacitive	106
A.15	Process flow and Runcard	107

Chapter 1

Introduction

This Master Project was conducted in the frame of a research performed in the Laboratory of Microsystems (LMIS2, EPFL) and consists in the development of monolithic micromotors for microrobotic applications. The Master project is a follow-up to the work performed during the Semester Project: “A monolithic microrobotic arm in silicon” [21].

The purpose of this Master Project is to characterize the static and dynamic behavior of the micromotor and to establish a mathematical model of the complete system. Furthermore, the design of an improved version of the micromotor and a demonstrator will be provided. Finally, we will fabricate the prototypes in the EPFL Center of MicroNanoTechnology (CMi), using a simplified single-mask process.

A mathematical model of the micromotor has been established and compared with the experiments performed in the quasi-static, transient and dynamic regimes. In addition, the Finite Element Analysis (FEA) simulations are consistent with both the mathematical model and the experimental characterization. The realized prototypes validate the single-mask process.

In Chapter 2, we will first establish the state of the art. The simulations performed on the micromotor’s flexible structure will be exposed in Chapter 3, followed by the presentation of the measurement method in Chapter 4. Chapter 5 will present the dynamic characterization of the micromotor. Then, the mathematical modeling of the micromotor will be developed in Chapter 6. Chapter 7 will finally discuss the improved design of the micromotor and the demonstrator, including the fabrications results.

Chapter 2

State of the art review

The purpose of this chapter is to provide an overview of the state of the art on the two main aspects of the project:

- The **flexure beams**, with a particular emphasis on monolithic flexures, used for high precision robotics (Section 2.1);
- The **electrostatic stepper micromotors** based on flexural pivots, used for skew angle compensation and microrobotic applications (Section 2.2).

The **initial project state** will briefly be exposed in §2.2.3. Indeed, this Master Project is a follow-up to the work performed during the Semester Project: “ A monolithic microrobotic arm in silicon” [21]. For this reason, we need to clarify the initial project state.

This chapter is intentionally kept succinct. For a thorough insight, the reader is referred to the publications in reference.

2.1 Flexure beams

Monolithic flexural guidings have been employed since the second half of the 20th century in response to the demand for very accurate guiding. Indeed, the classical mechanical hinges, consisting of multiple elements, are difficult to miniaturize. Their use in vacuum and clean environment is limited by dust emission and their motion presents hysteresis (or backlash due to clearance between the components) [9]. Flexural hinges, which are based on the elastic deformation of the material before plastic deformation, overcome these limitations. They have found many applications in precision engineering [14], metrology or aerospace fields [10] and can be found at scale ranging from centimeter down to micrometer.

2.1.1 Advantages and limitations of flexure beams

Monolithic flexural hinges present many advantages compared with classical mechanical hinges, composed of multiple elements (*e.g.* ball bearing). Flexural hinges also have some limitations [9]. In the following list, we will discuss their properties in more detail.

- a The friction less based pivots present **no wear**. This major advantage implies the following positive consequences: **No dust** is created in this type of structure, there is **no risk of jamming** and **no lubricant** is needed. This property is particularly attractive in micromechanics applications, where dust and lubricant limitations are very critical. This also opens a path for vacuum-compatible applications.
- b Secondly, these bearings do not have **any backlash** due to clearance between the components. This backlash-free displacement implies the **absence of hysteresis** compared to conventional mechanical bearings. The displacement of the monolithic structure is then **accurate, precise and repeatable**.
- c **Flexural bearings somewhat have a limited displacement**. The limited displacement is indeed a limitation if a large displacement is needed but a well studied design can have large strokes, as we will discuss in §2.1.3.3 [24]. Also, the energy used to deform the matter can be advantageously stored. Indeed, the only dissipation is due to the internal friction of the matter. In a well designed system, this aspect is advantageous because this energy can be re-used: the device is self-returning, self-centering to its initial position.
- d An important aspect is the **high radial, axial and transversal rigidity** of this type of bearing. The stiffness of the locked degrees of freedom is very important compared with the free ones and it leads to very good compliance properties.

For a more detailed discussion on the properties of flexure hinges, the reader is referred to the Ph.D thesis of Simon Henein [9].

Example of a Flexure hinge: The cartwheel hinge

Let's discuss these different aspects through the study of a four degree of freedom (DOF) device: A two DOF xy -table guided by classical mechanical bearings with two additional DOF provided by flexural bearings, as illustrated in Figure 2.1 [1].

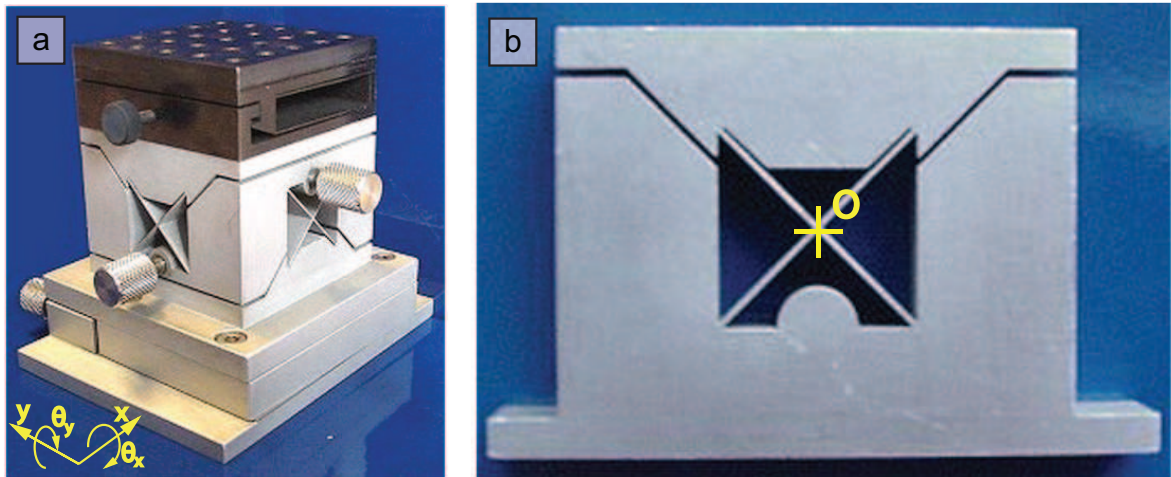


Figure 2.1: Example of a compliant mechanism [1]: (a) xy -stage with two DOF (x , y) and two additional rotational DOF obtained using flexural bearing (θ_x , θ_y); (b) detail of the cartwheel hinge: the center of rotation is situated approximately in the middle of the flexible metal cross

We will focus more specifically on the compliant element, composed of two crossing beams (see Figure 2.1 (b)) called “cartwheel hinge”. It can be deformed in a predictable pseudo-rotative displacement whose center of rotation O is located in the middle of the X shape [14]. In this particular case, the limited displacement range is sufficient and the transversal rigidity appropriate.

Compared with the xy -stage, the compliant hinge does not have any hysteresis in its movement: it does not need to overcome a static friction threshold. Furthermore, the hinge is much more simple in its fabrication and assembly. Indeed, Figure 2.1 (b) the cartwheel hinge has been realized using electric discharge machining (EDM). The planar nature of the hinge makes it suitable for other manufacturing processes, such as LIGA¹ at micrometer scale, 3-axis milling, stamping, vertical etching of material or any other vertical extrusion process. The EDM process is largely used in robotics, as discussed by Simon Henein in his Ph.D [9]. For micrometer scale, etching processes are preferred.

Figure 2.2 is a schematic of the cartwheel hinge. The axis of rotation presents a parasitic center shift and, as exposed in §2.1.1, this displacement can be calculated using material strength theory. The angular stroke of the beams is restrained by stops in order to remain in the elastic deformation domain of material.

¹German acronym for Lithographie, Galvanoformung, Abformung (Lithography, Electroplating, and Molding)

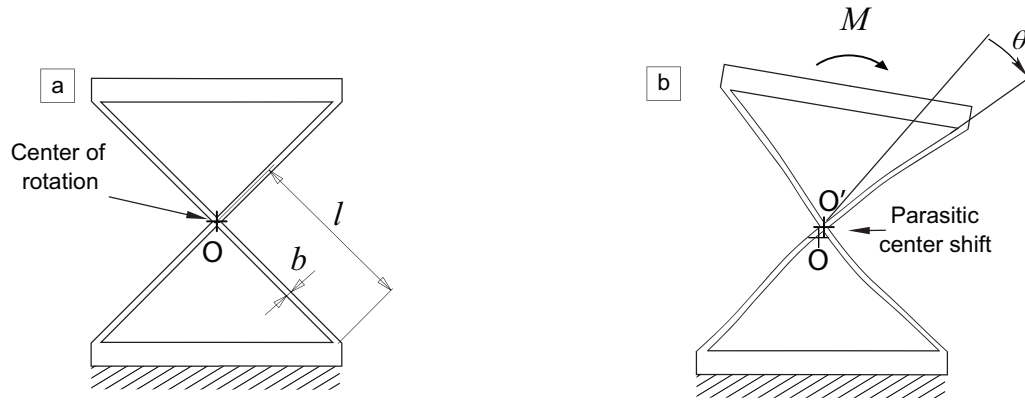


Figure 2.2: Schematic of the cartwheel hinge: (a) Cartwheel hinge with flexure beams of length l and width b ; (b) Cartwheel hinge rotated by an angle θ due to a torque M .

At micrometer scale, the potential of such bearing is fully exploited, as their high precision and cleanness is relevant. A lot of applications are found in Micro Electro Mechanical Systems, MEMS.

In the following sections, we will introduce the linear guidings (§2.1.2.1) and the rotational guidings (§2.1.3).

2.1.2 Linear guidings

In this section, we will present two types of linear guidings. The description of the linear guidings is kept succinct and will serve as an introduction to more complex rotational bearings.

2.1.2.1 Basic linear guiding

The working principle of a basic linear guiding is schematically described in Figure 2.3. A rigid element, bloc B, is guided by two flexural beams in a parabolic trajectory: The displacement can be decomposed in a horizontal translation Δx and a parasitic vertical displacement Δy .

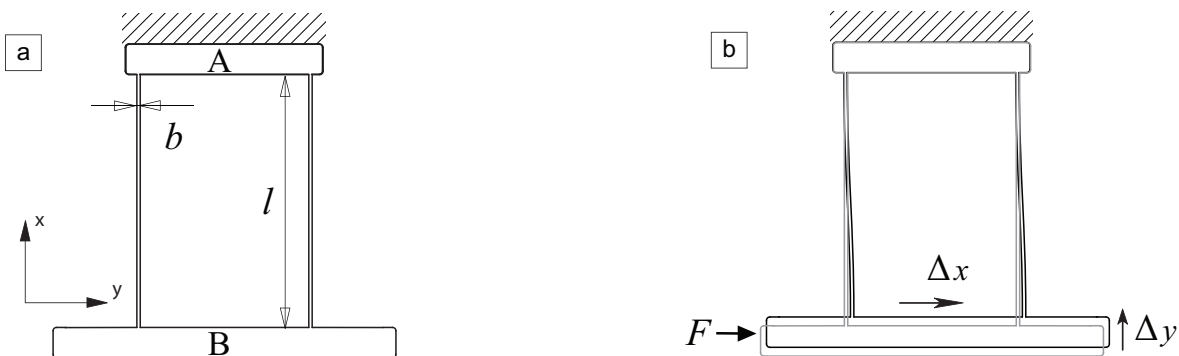


Figure 2.3: Basic linear guiding: (a) Flexible linear guiding consisting of two beams of width b and length l with an out-of-plane height h ; (b) Flexible linear guiding under constrain: A force F causes a displacement Δx and a parasitic displacement Δy . Block A is fixed, while block B is mobile.

2.1.2.2 Double-parallelogram linear guiding

A more complex linear guiding has been developed to cancel the parasitic displacement Δy . Known as “four beam guiding” or “folded beam flexure”, it is composed of two linear guidings that are linked in series in order to reduce the parasitic motion along the y axis.

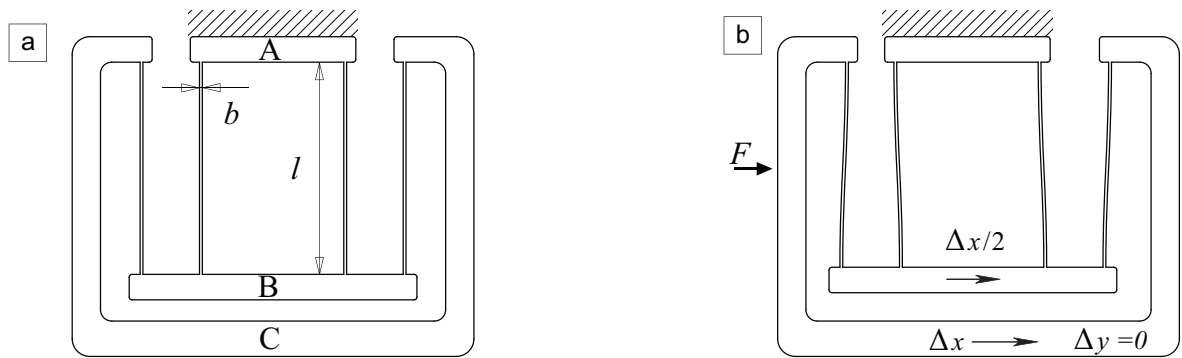


Figure 2.4: Folded beam flexure : (a) Double-parallelogram linear guiding consisting of four beams. The geometrical parameters of the beams are the same as in Figure 2.3; (b) Double-parallelogram linear guiding under constraints. Block A is fixed, the intermediate stage B is displaced by $\Delta x/2$, while block C is displaced by Δx .

Figure 2.5 shows an example of a linear stepper micromotor realized in silicon using folded beams flexure for the guiding of the micromotor [17]. Stages B and C from Figure 2.4 are the meshed structures.

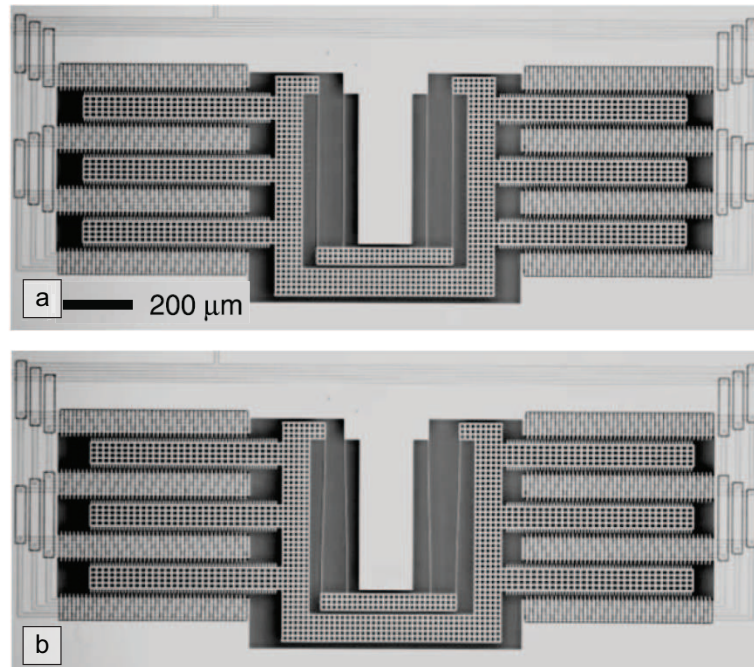


Figure 2.5: Micrographs of a linear micromotor in silicon using folded beam guiding, fabricated using vertical trench isolation technology [17]. (a) Linear micromotor at its resting position; (b) Linear micromotor displaced to the right.

2.1.3 Rotational flexural bearing

Having introduced the linear guidings, we can now focus on the rotational pivot. We present here a short review of a particular type of flexure pivot: The four-beam flexural pivot [18, 21, 22] and the butterfly pivot [9, 10].

2.1.3.1 Four-beam flexural pivot

The four-beam flexural pivot is illustrated in Figure 2.6. It is the homologous version of the folded beam flexure.

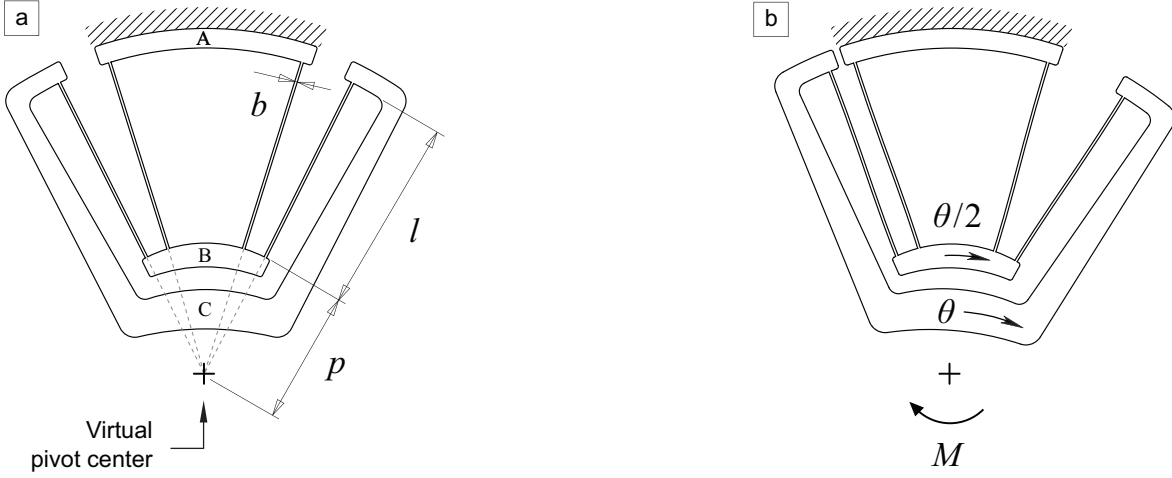


Figure 2.6: Four-beam flexural pivot:(a) Four-beam flexural pivot composed of four beams of width b and length l with an out-of-plane height h ; (b) Four-beam flexural pivot under constrain: the torque M induces a rotation θ . Block A is fixed, the intermediate stage B is displaced by $\theta/2$, while block C is displaced by θ .

S. Henein *et al.* and E. Sarajlic *et al.* [9, 18] studied and established the equation of the deformation, using material strength theory.

The **four-beam pivot stiffness** K is [18]:

$$K = \frac{M}{\theta} = \frac{4EI}{l} \left(1 + 3\frac{p}{l} + 3\frac{p^2}{l^2}\right), \text{ with } I = \frac{hb^3}{12} \quad (2.1)$$

Where E is the Young modulus of the beam material, h is the out-of-plane height, b is the width of the flexure hinges, l the length of the beam and p the distance to the virtual pivot center. I is the moment of inertia of the beam.

The **maximum angular displacement** θ_{adm} before plastic deformation of the beam, is the following:

$$\theta_{adm} = \frac{2\sigma_Y l^2}{Eb(2l + 3p)}, \quad (2.2)$$

where σ_Y is the yield strength of the material [18].

2.1.3.2 Four-beam flexural pivot with reinforced beam

The study of this guiding has been pursued by M. Stranczl *et al.* who further modified the four-beam pivot, by adding a reinforced beam of length a in the flexural elements in order to create a new design with a higher out-of-plane stiffness and a more robust structure [21, 22].

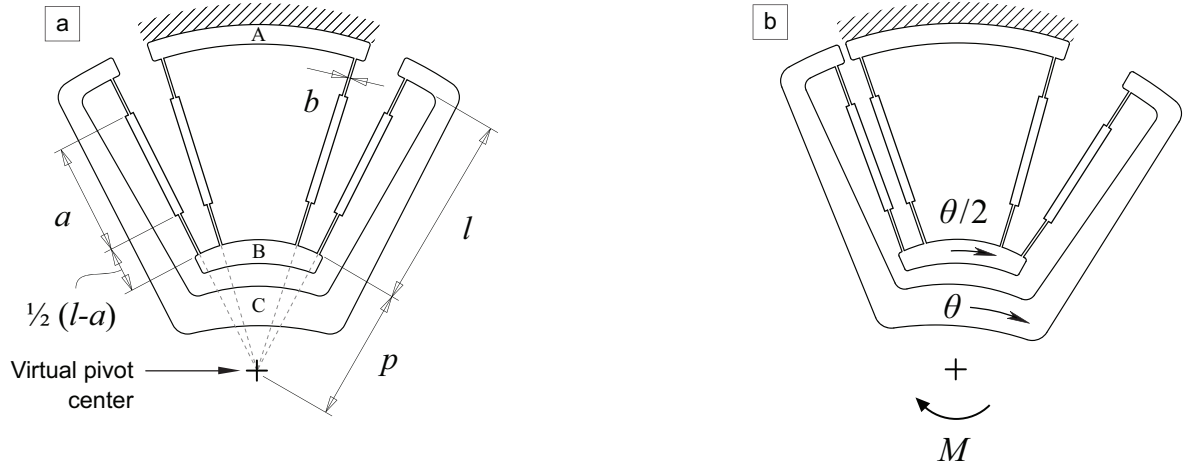


Figure 2.7: Four-beam flexural pivot with reinforced beams:(a) Four-beam flexural pivot with reinforced beam: The geometric parameters are the same as for the four-beam flexural pivot, with the additional parameter a , the length of the central reinforced structure; (b) Four-beam flexural pivot with reinforced beams under constrain: the torque M induces a rotation θ [21, 22]. The block A is fixed, the intermediate stage B is displaced by $\theta/2$, while the block C is displaced by θ .

The **four-beam pivot with reinforced beams stiffness** K_r , calculated using Castigliano and Menabrea theory [21], is:

$$K_r = EI \frac{a^2 + al + 4(l^2 + 3lp + 3p^2)}{(l-a)(a^2 + al + l^2)}, I = \frac{hb^3}{12} \quad (2.3)$$

The index “ r ” refers to reinforced beams. The **maximum angular displacement** $\theta_{r,adm}$ is [21]:

$$\theta_{r,adm} = \frac{4\sigma_Y(l-a)(a^2 + al + l^2)}{Eb(a^2 + al + 2l(2l + 3p))} \quad (2.4)$$

We can easily verify the validity of these equations in their border limits ($a \rightarrow 0$ and $p \rightarrow \infty$) with the equations of the four-beam pivot [18] and equation (2) and (3) of [18].

These equations have been calculated using the following approximation: the reinforced beam can be considered as a non-deformable rigid body. The validity of this approximation will be confirmed in Chapter 3 (§3.1).

2.1.3.3 Butterfly pivot

The “butterfly pivot” devised by S. Henein [10] is a pivot designed to guide pointing and scanning devices in aerospace mechanisms. It is composed of two four-beam flexural pivot in series.

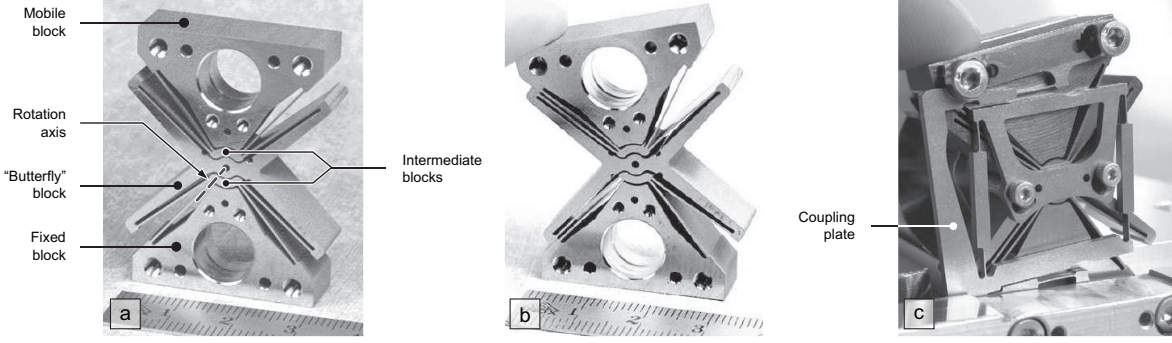


Figure 2.8: Flexural pivot: (a) Butterfly pivot; (b) Butterfly pivot under constraints; (c) Butterfly pivot with the internal part guided.

The design has been realized in Titanium (TiAl6V4) and manufactured by wire EDM. The authors have conducted different studies on the parasitic center shift compensation, on the load capabilities, on the fatigue life cycling and on the resonance frequencies of the structure [10]. Moreover, Henein *et al.* suppressed the internal degree of freedom of the butterfly at the cost of a second assembled piece, *the coupling plate*, in order to control the internal eigenmodes (see Figure 2.8).

The monolithic flexural structure in Figure 2.8 (b) reaches a parasitic center translation of axis lower than $2 \mu\text{m}$ over a $\pm 10^\circ$ motion range for a pivot of 5 cm height.

As explained before, the butterfly is the connection of two four-beam pivots in series. Therefore, the resulting stiffness of the butterfly pivot is:

$$K_{\otimes} = \frac{K}{2}; K_{\otimes,r} = \frac{K_r}{2}, \quad (2.5)$$

where the index \otimes symbolizes the butterfly pivot. The maximum angular displacement $\theta_{\otimes,adm}$ of the butterfly pivot and the reinforced butterfly pivot $\theta_{\otimes,r,adm}$ is:

$$\theta_{\otimes,adm} = 2 \cdot \theta_{adm}; \theta_{\otimes,r,adm} = 2 \cdot \theta_{r,adm} \quad (2.6)$$

The parameters are the same for the four-beam flexural pivot.

The rigid elements increase the stiffness of the butterfly pivot depending on its length.

This effect has been studied in [21]. We report in Figure A.1 of Appendix A.1, the reinforced butterfly pivot stiffness $K_{\otimes,r}$ as function of the ratio a/l .

2.2 Electrostatic stepper micromotors

In this section, we briefly present the previous studies performed on electrostatic stepper micromotors. We will first focus on micromotors designed for skew angle compensation in hard disk drive HDD. We will then provide an overview of a project performed at EPFL on microrobotics, using such types of stepper micromotors.

2.2.1 Micromotors for skew angle compensation in HDD

Skew angle compensation is a critical point in data storage: the density of data stored depends on this parasitic angle. The implementation of a micromotor in the read/write head can correct this angle, as illustrated in Figure 2.9. For more details on micromotors for skew angle compensation, the reader is referred to [18].

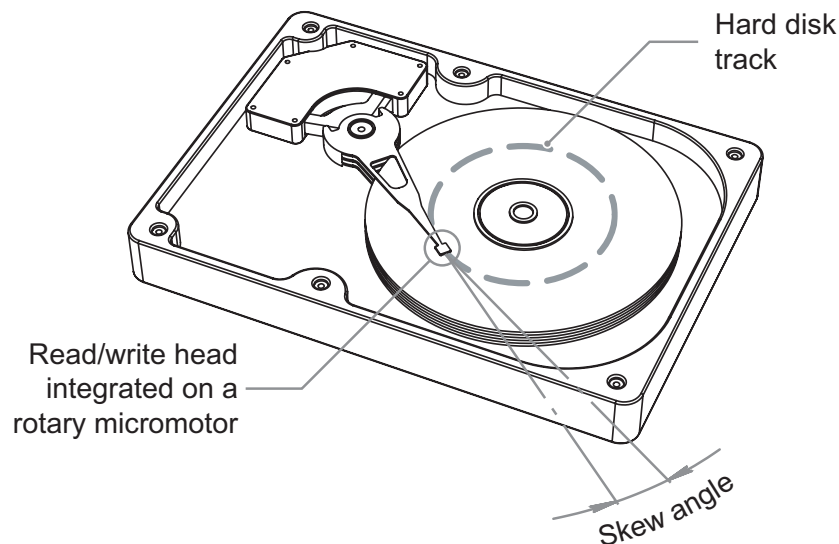


Figure 2.9: Hard disk drive: Skew angle compensation by a micromotor between the track and the read/write head. Figure reproduced from [18].

Many types of motors exist at micrometer scale which can be implemented for skew angle compensation. This state of the art will only concentrate on a specific development: the monolithic electrostatic stepper micromotor in silicon developed by Sarajlic *et al.*. We will more precisely focus on a project initiated a few years ago in Japan, supported by the Storage Research Consortium (SRC), in which Sarajlic *et al.* developed a micromotor based on a butterfly pivot fabricated in silicon using vertical etching [18].

The three-phase electrostatic stepper micromotor with flexural mechanisms is presented in Figure 2.10.

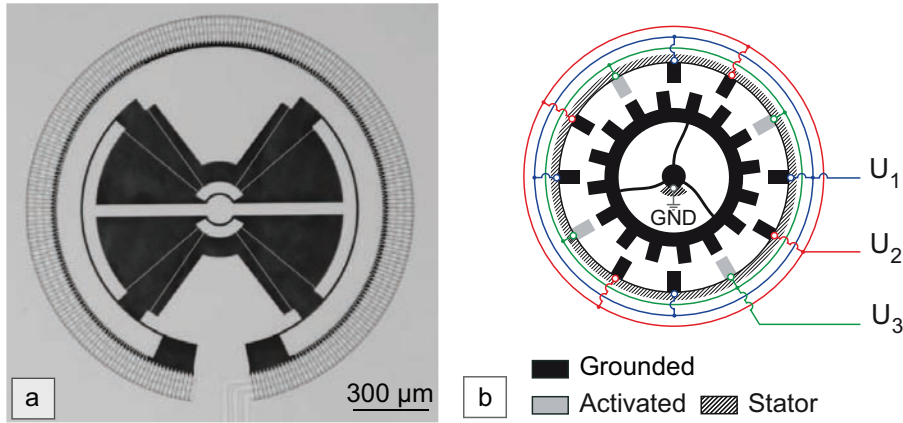


Figure 2.10: Electrostatic stepper micromotor: (a) Micrograph of the micromotor; (b) Schematic of the micromotor and working principle of the three-phase electrostatic rotary stepper micromotor with flexural mechanisms. Figure partially reproduced from [18].

2.2.1.1 Working principle

Figure 2.10 (b) shows the working principle and the main elements of the electrostatic stepper micromotor. The motor consists of a 3-phase stator and a grounded rotor which is suspended by a flexural mechanism [10]. This frictionless bearing enables a rotational degree of freedom with a certain torsional stiffness. The stator electrodes are symmetrically and alternatively located around the rotor (see Figure 2.10 (b)). Each phase can be activated independently (voltages U_1 , U_2 and U_3). In the initial position, the electrodes of the first phase are perfectly aligned with the opposite electrodes on the rotor. The stator electrodes of the two other phases have a misalignment which is equal to $1/3$ of the pitch of the rotor electrodes.

2.2.1.2 Micromotor design

The angular displacement θ of the micromotor depends on the electrostatic torque generated and on the flexural suspension stiffness:

$$\theta = M_{el}/K_{\otimes}, \quad (2.7)$$

where M_{el} is the electrostatic torque, K_{\otimes} the butterfly pivot stiffness.

The electrostatic Torque for one phase can be approximated using the parallel plate capacitor approximation and its simplified expression is [18]:

$$M_{el} = \frac{1}{2}n\varepsilon_0r\frac{h}{g}U^2, \quad (2.8)$$

where n is the number of active teeth per phase, ε_0 the permittivity of air, h the height of the teeth (eight of the planar micromotor), g the gap between the electrodes teeth and U the voltage applied on the corresponding phase.

The flexural pivot stiffness equation has already been presented in §2.1.3.

The butterfly pivot is used for several reasons. First of all, this flexure pivot has been chosen for its monolithic structure, its absence of wear and reliability. Secondly, it works as a support for electric connections for the read/write head of the HDD. Furthermore, the butterfly pivot has a large radial stiffness. Indeed, as previously mentioned, this is a critical point: the radial symmetry should be respected, otherwise the rotor sticks to the stator due to electrostatic forces.

2.2.1.3 Experimental results

The micromotor developed in the frame of the Storage Research Consortium, having a diameter of 1,4 mm, has been realized by vertical trench isolation technology [18] with a 5-mask process. It is important to notice that the rotor is suspended in air, contrary to the design presented hereafter in §2.2.2. The micromotor presents an angular displacement of $26^\circ (\pm 13^\circ)$ for 75 V square-wave driving voltage and a maximum speed of $1,67^\circ/\text{ms}$. The motion depends quadratically on the voltage as expected, but was limited at 75V due to electrostatic discharges in the tracks' insulations. The butterfly pivot showed good radial stiffness and did not suffer from “sticktion” to the stator. Some additional studies have been performed on the driving signals and a $1/48^\circ$ resolution has been archived with microstepping driving voltage instead of a $1/6^\circ$ resolution with a simple square driving signal. Further details can be found in reference [18].

2.2.2 Micromotors for microrobotic applications

C. Yamahata offered in a semester student project at EPFL Lausanne, to develop a SOI micromotor of a similar type, as previously described. The semester project has been completed by M. Stranczl and we briefly summarize here the results. More details can be found in [21, 22].

2.2.2.1 Micromotor design

The electrostatic stepper micromotor has first been modified in order to be fabricated using silicon on insulator (SOI) wafers. With this technological choice, the fabrication process could be significantly simplified (1-mask or 2-mask instead of a 5-mask process) to a single mask process.

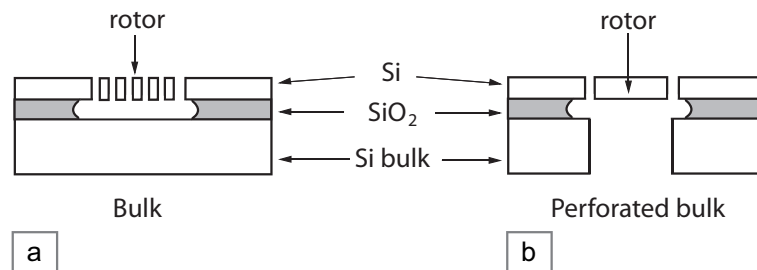


Figure 2.11: Silicon-on-insulator structure: (a) Single-mask process: perforated micromotor for oxide etching access; (b) Two-mask process: micromotor with bulk perforated to avoid the accumulation of capacitive charges

Indeed, the monolithic micromotor structure can be structured in the thin silicon layer using a vertical etching process and released by etching the oxide layer using a selective etching process, as shown in Figure 2.11 (a). This design follows the process used by E. Sarajlic [19] for the fabrication of a single-mask SOI micromotor.

However, E. Sarajlic has dealt with an accumulation of charges in the bulk, resulting in the sticking of the rotor to the bulk by electrostatic forces. For this reason, some devices have the bulk etched in the rotor region, see Figure 2.11 (b). This optional step requires a second mask.

The design of the micromotor is illustrated in Figure 2.12.

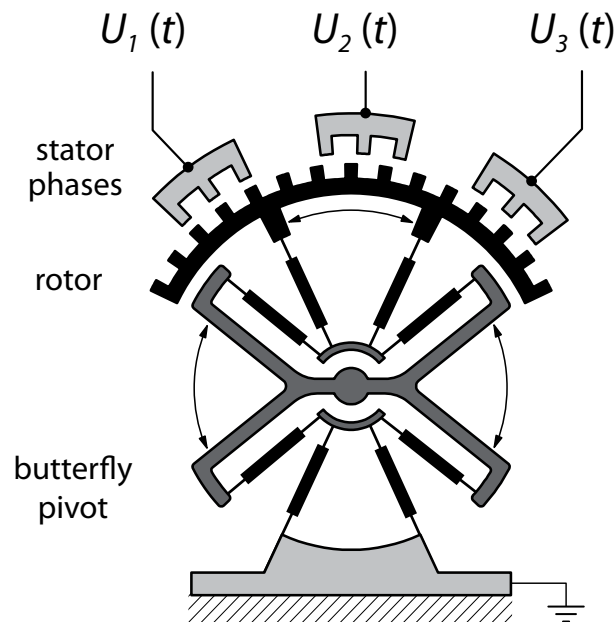


Figure 2.12: Monolithic micromotor: Schematic principle of the 3-phase electrostatic stepper motor (actuated with voltages U_1 , U_2 , U_3). The internal butterfly structure mechanically connects the rotor to the chassis.

We can see several modifications comparing Figure 2.10 (a) with Figure 2.11 (b).

The connection path has been simplified by grouping the teeth of each phase in pairs, as shown in Figure 2.12. The butterfly structure has an X shape instead of an H shape in order to reduce the inertia of this internal element. An opening in the stator, which enables the inclusion on an arm required for microrobotic applications, has also been added.

In parallel to the work performed at EPFL, actuation simulations were performed in Japan by Junji Sone *et al.* [20]. Numerical studies have been realized on capacitance variation depending on the displacement, on the resonant frequencies, on the effects of the damping and on the driving signal shape and amplitude influence on the performances. These aspects will be discussed in Chapter 6.

2.2.2.2 Experimental results

The devices have been fabricated using two types of processes: The single mask process and the two masks processes. Notice that the micromotors fabricated using a single mask process have a mesh-like structure for the mobile elements. This is due to the etching access needed in order to release the oxide, as illustrated in Figure 2.11.

Single-mask process – The mesh-like devices present an angular motion of $8^\circ (\pm 4^\circ)$ for 35-40 V with a square drive voltage actuation (see Figure 2.14). The devices were stopped in their motion due to the electrostatic sticking of the rotor to the bulk even with design precautions: The bulk is connected to the ground and the silicon bulk is more conductive than the previous design.

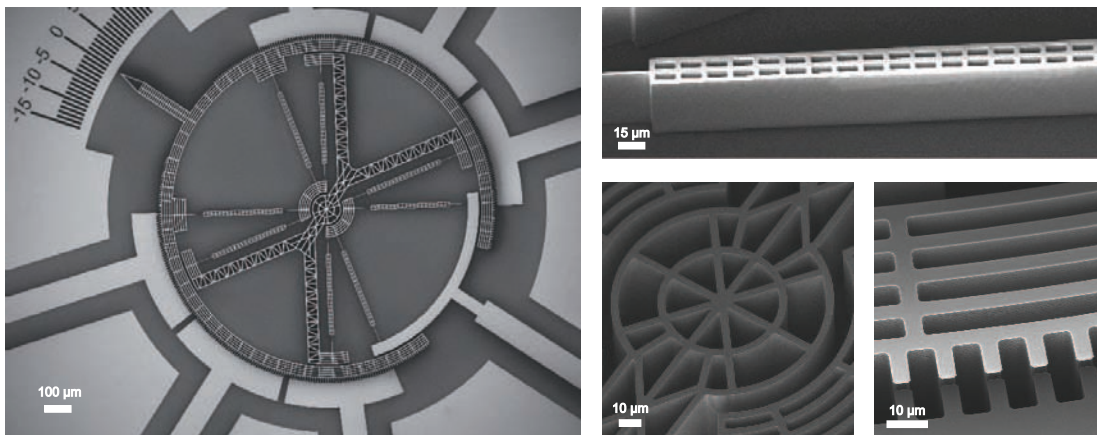


Figure 2.13: Single-mask process micromotor: Scanning electron microscopy micrographs of a 3-phase electrostatic stepper micromotor fabricated with SOI technology. The mobile parts are perforated (mesh structure)

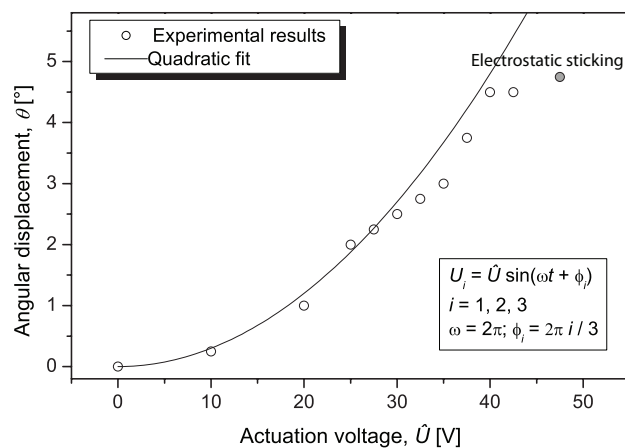


Figure 2.14: Maximum angular displacement of the SOI single-mask stepper motor as a function of the driving voltage (3-phase sinusoidal excitation of 1 Hz). Data are for positive displacements only: The displacement range is double. The motion is limited to 40 V (4°) due to the sticking of the rotor to the bulk by electrostatic charges

Two-masks process – The perforated bulk devices have a motion of $30^\circ (\pm 15^\circ)$ for 65 V actuation, as illustrated in Figure 2.16. These quasi-static results reach the motion objective of the project.

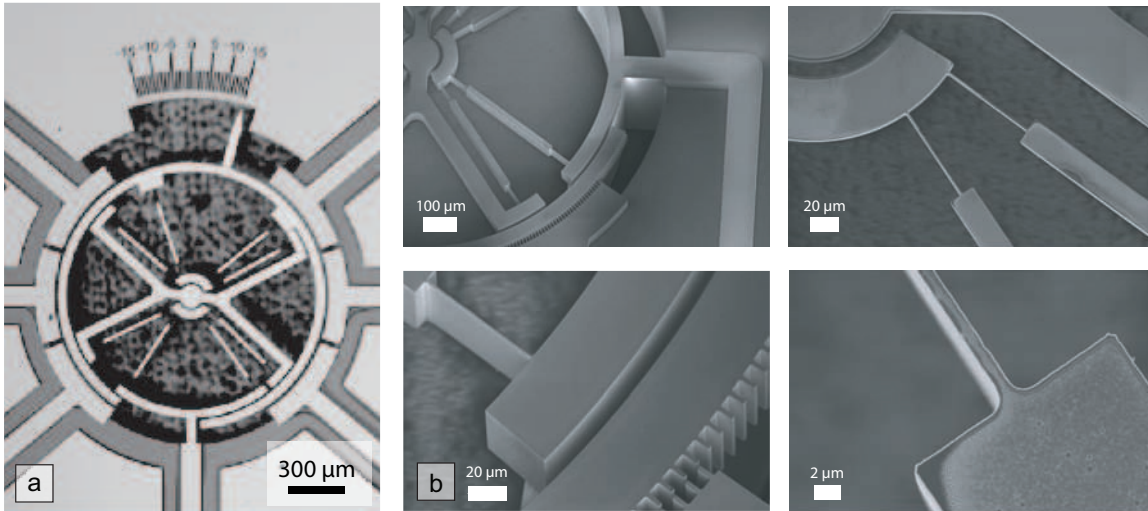


Figure 2.15: Two-mask process micromotor: (a) Micrograph of the fabricated SOI micromotor rotated clockwise by $+15^\circ$; (b) Scanning electron microscopy micrographs of a 3-phase electrostatic stepper micromotor fabricated with SOI technology. The bulk is perforated in the rotor region. The rotor does not need a mesh-like structure.

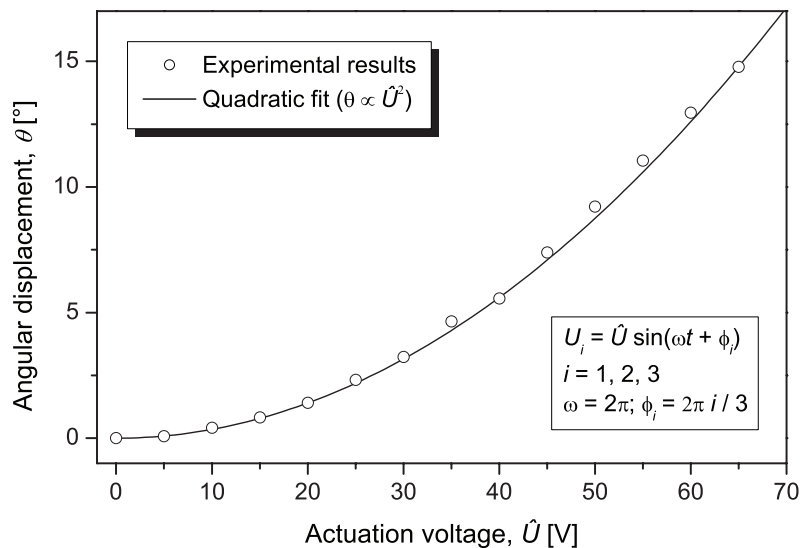


Figure 2.16: Maximum angular displacement of the SOI two-mask stepper motor as a function of the driving voltage (3-phase sinusoidal excitation of 1 Hz). Data are for positive displacements only: The displacement range is double [22].

Thanks to the very good performances of the micromotors, we have performed many additional measurements in the quasi-static and dynamic ranges. The measurement methods will be presented in Chapter 4.

Quasi-static and transient responses - In Figure 2.16, we show quasi-static measurements performed with a 3-phase sinusoidal driving sequence at 1 Hz. The maximum angular displacement increases quadratically with the applied voltage, as expected for an electrostatic actuator [18]. Figure 2.17 presents the transient response obtained by releasing the rotor from a small angle to its resting position. The damping coefficient and the first in-plane resonant frequency have been extracted from these data. Figure 2.18 exhibits a typical motion of the rotor rotated from 0° to $+9^\circ$. An angular speed of $1^\circ/\text{ms}$ could be reached with a driving signal of 600 Hz and 70 V amplitude. The measurements shown in Figures 2.17 and 2.18 were performed with a high-speed camera (Mikrotron CMOS high-speed camera, EoSens MC1363), using the algorithm described in [29].

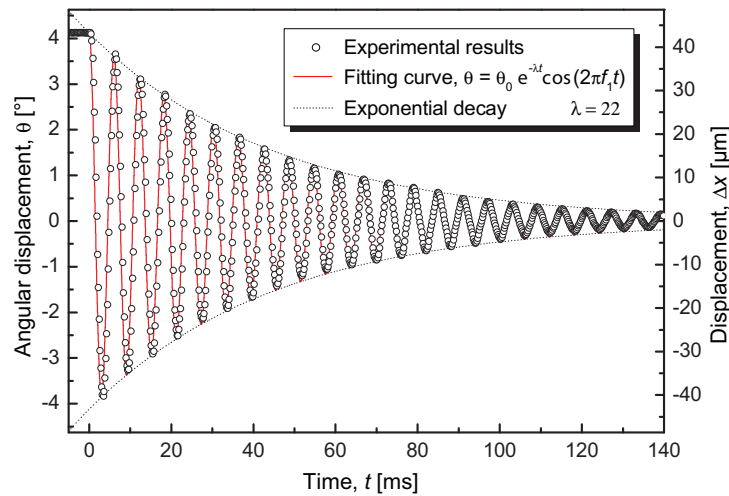


Figure 2.17: Transient response of the rotor. The measurements were performed on the rotor's external ring. The first resonant frequency of 163 Hz can be extracted from the Fourier transform of these data. [22]

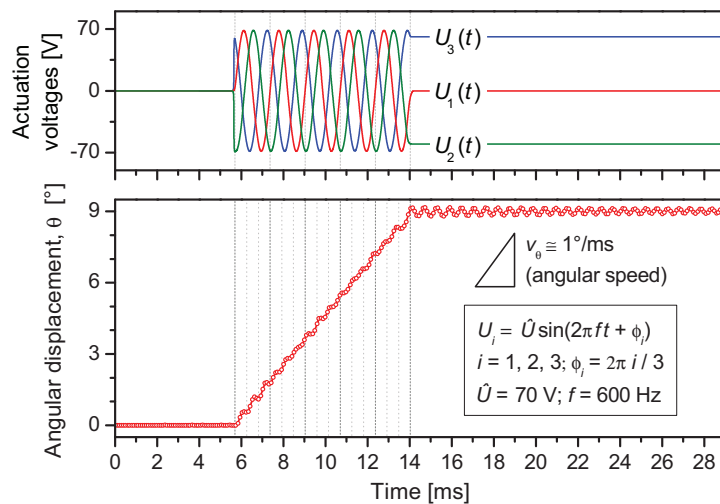


Figure 2.18: Typical recording of the angular displacement as a function of time. A 3-phase sinusoidal driving signal at 600 Hz and 70 V was applied, as illustrated in the upper part of the graph. With these settings, an angular speed of $1^\circ/\text{ms}$ was reached. Reproduced from [22]

Experimental modal analysis – Thorough in-plane and out-of plane modal analysis of the structure have been performed with the Polytec Micro System Analyzer MSA-400. Figure 2.19 illustrates the in-plane data recorded by stroboscopic video microscopy, under application of a sine excitation signal on phase 2, while the other phases were grounded.

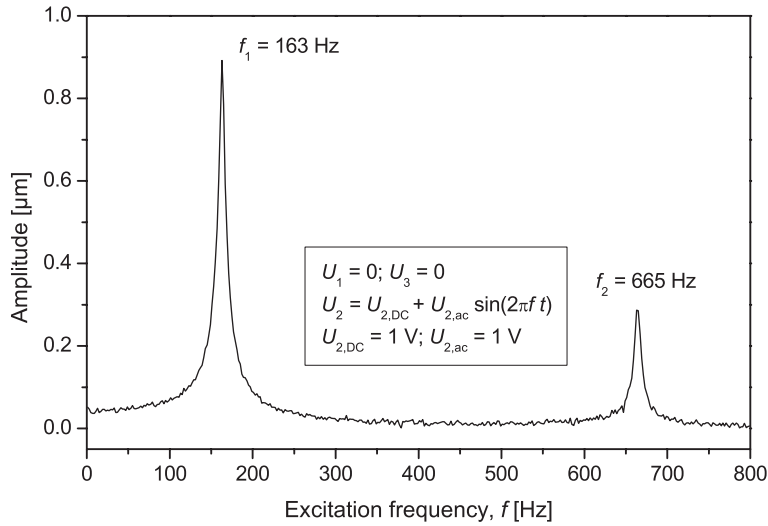


Figure 2.19: In-plane modal analysis of the micromotor rotor recorded by stroboscopic video microscopy (Polytec MSA-400). These results are in line with the transient measurement of Figure 2.17. The first resonant peak appears at 163 Hz and the second at 665 Hz. Data reproduced from [22].

The out-of-plane response was obtained by Laser-Doppler vibrometry. Figure 2.20 and 2.21 shows the eigenmode measured with the Polytec Micro System Analyzer MSA-400.

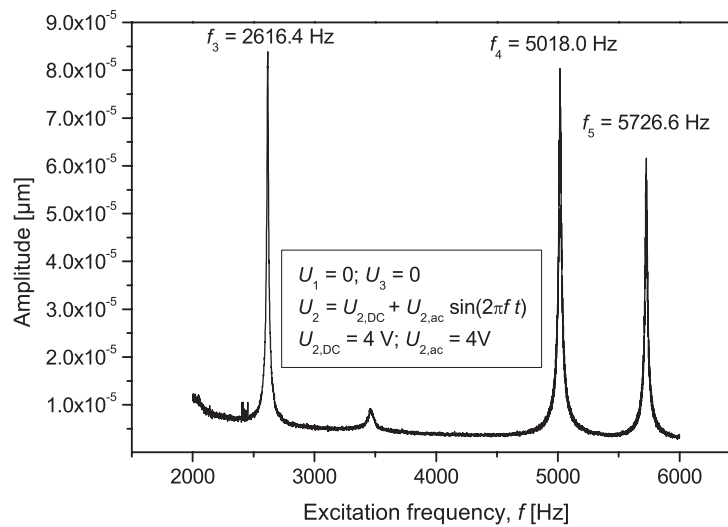


Figure 2.20: Out-of-plane modal analysis of the micromotor recorded by Laser-Doppler vibrometry (Polytec MSA-400). The third resonant peak appears at 2616.4 Hz, the fourth at 5018.0 Hz and the fifth at 5726.6 Hz (unpublished graph [22]).

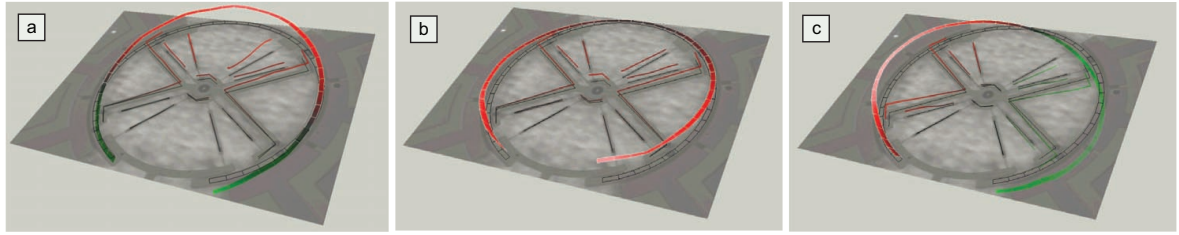


Figure 2.21: Out-of-plane measurements performed with Polytec MSA-400. The third resonant peak (a) occurs at 2616.4 Hz , the fourth peak (b) at 5018.0 Hz and the fifth (c) at 5726.6 Hz (unpublished graph [22]).

2.2.3 Initial project state

This Master Project continues the work performed on the “micromotor for microrobotic application project” [21] and we need then to establish the state of the global project at the end of Summer 2010, before the Master Project’s beginning. The results and measurements presented above precede the Master Project and have been the subject of a conference article, written during the Master Project by M. Stranczl and C. Yamahata [22]. However, the interpretation of the results and more particularly the electrostatic stiffening are entirely part of the Master Project. Reference [22] summarizes part of the results obtained at the beginning of the Master Project (October and November 2010).

Chapter 3

Finite Element Analysis

In this chapter, we present the Finite Element Analysis (FEA) simulations performed on the micromotor presented in §2.2.2. They have been performed with SolidWorks Simulation software (SolidWorks 2009 SP5.0). Note that these simulations focus on the mechanical properties only. The electrostatic actuation modeling is another important aspect which will be considered later in Chapter 6.

In this chapter, we will focus on the following points:

- We will first simulate the **RCC¹ pivot** structure. The analytical equations presented in Chapter 2 (Eq.2.1 and 2.3) will be compared to the simulations (load-dependent deformation).
- We will perform additional load simulations on the whole **butterfly pivot** in order to confirm some deformation characteristics.
- The **buckling** of the beams, and more particularly the effect of the rigid block, will be studied. The complete butterfly structure will also be tested up to its buckling charge limit.
- To complete this chapter, **modal analysis** simulations will be performed and the effects of **silicon anisotropy** will be studied.

All the simulations have been performed on the micromotor designed for a two-mask process, since it does not have a perforated structure. These solid structures can be more easily simulated with FEA softwares, and compared with the analytical model [22].

For all the FEA simulations performed in this chapter, the geometrical parameters correspond to “two-mask” micromotors (Appendix A.1), unless otherwise specified.

¹RCC is an acronym for Remote Center of Compliance. This pivot is described in §3.1.1.

3.1 Flexural bearing simulations

3.1.1 Analytic model and RCC pivot simulations comparison

RCC pivot – The first simulations have been performed on the Remote Center of Compliance (RCC) pivot, see Figure 3.1. Indeed, the butterfly pivot is composed of four RCC pivot in series, as illustrated in Figure 3.1 [18].

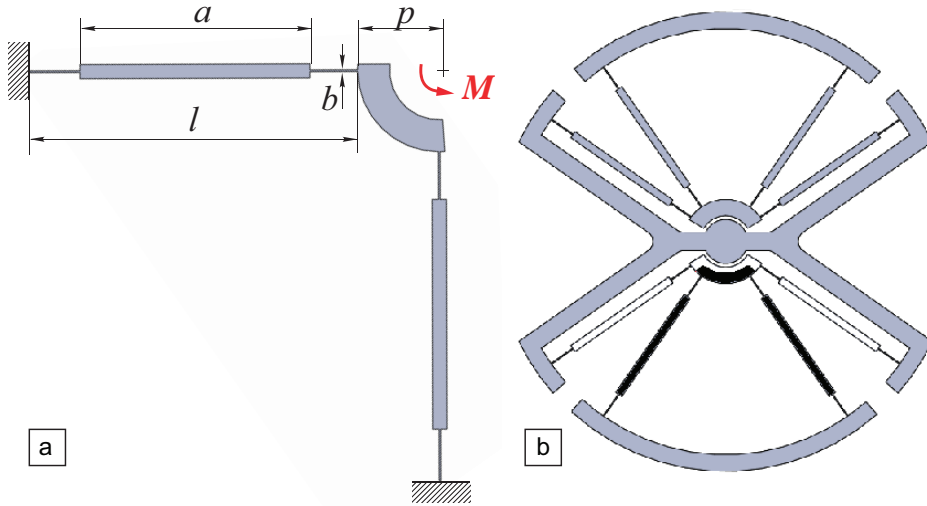


Figure 3.1: Butterfly pivot and RCC pivot: (a) RCC pivot: The parameters are similar as the folded beam flexure (§2.1.3); (b) Butterfly pivot with two of the four RCC pivots highlighted in white and in black.

The RCC pivot stiffness is related to the butterfly pivot stiffness with a factor four (see Appendix A.2):

$$K_{\otimes} = \frac{K_{RCC}}{4}; K_{\otimes,r} = \frac{K_{RCC,r}}{4}, \quad (3.1)$$

where the index RCC refers to the RCC pivot.

RCC pivot simulations parameters – The deformation of the RCC pivot for a torque M has been simulated depending on the beam width b . The applied torque on the RCC pivot has been calculated with the equations 2.1, 2.3 and 3.1, in order to reach an approximative rotation of $+5^\circ$ and $+10^\circ$. In the next two pages, this theoretical rotation of $+5^\circ$ and $+10^\circ$ has been compared to the simulated rotation and the percentage of error calculated relative to the theoretical value. The simulations have been performed on RCC pivot with simple beams and with reinforced beams.

The following simulations have been realized considering the material as an isotropic material as we want to compare the results with the theoretical one which considers the material isotropic. The material properties of silicon are listed in the Appendix A.3.

Displacement simulations for $\theta = +5^\circ$					
Parameters			Theoretical rotation	Simulated rotation	Error
Beam Type	b [μm]	M [Nm]	θ_{th} [$^\circ$]	θ_{sim} [$^\circ$]	$\epsilon = \frac{\theta_{sim} - \theta_{th}}{\theta_{th}}$ ϵ
reinforced	2	$2,7 \cdot 10^{-8}$	4,996	4,66	-6.7 %
reinforced	3	$0,91 \cdot 10^{-7}$	4,990	4,61	-7.6 %
reinforced	4	$2,16 \cdot 10^{-7}$	4,996	4,78	-4.3 %
reinforced	5	$4,22 \cdot 10^{-7}$	4,998	4,81	-3.8 %
simple	2	$1,54 \cdot 10^{-8}$	4,994	4,63	-7.2 %
simple	3	$0,52 \cdot 10^{-7}$	4,997	4,90	-1.9 %
simple	4	$1,23 \cdot 10^{-7}$	4,986	4,83	-3.2 %
simple	5	$2,405 \cdot 10^{-7}$	4,992	4,83	-3.3 %

Table 3.1: Angular displacement simulation compared with theory. The material is supposed isotropic, with $E = 160$ GPa. The simulated moment, applied on the pivot M , has been calculated depending on the beam width b in order to obtain a 5° rotation (Theoretical rotation θ_{th}). This value is compared to the simulated one (Simulated value θ_{sim}). The percentage of error is relative to the theoretical value.

These simulations highlight a good conformity of the simulated displacement and the calculated one. The percentage of error is quite low (and also lower than the theoretical value $\epsilon < 0$) and increases with the beam width reduction. This is normal as the beams reaches the mesh limitation ($2[\mu\text{m}]$).

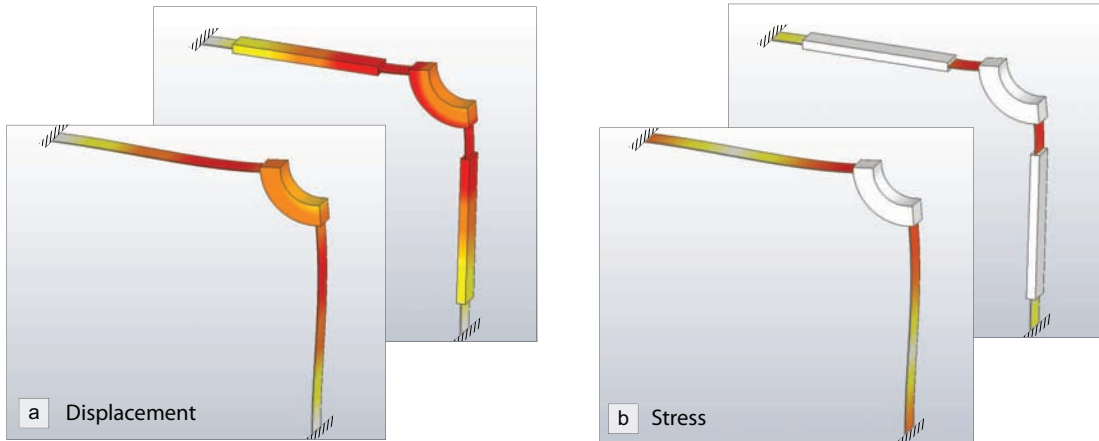


Figure 3.2: SolidWorks finite element analysis of the RCC reinforced pivot deformation for a 5° rotation: (top) reinforced beam, (bottom) simple beam. (a) Displacement simulations: the color levels describe the displacement magnitude relative to the anchor, white = $0 \mu\text{m}$, red = $14 \mu\text{m}$; (b) Stress simulations: the color levels describe the von Mises stress magnitude, white = 0 N/m^2 , red = $3,1 \cdot 10^8 \text{ N/m}^2$.

In Figures 3.2 and 3.3, we present the deformation of the RCC pivot (a) and the stress distribution along the beams (b) for the corresponding deformation. The displacement is composed of a pure rotation. The stress distribution for the simple beams are located along the whole beam and the highest stresses are located in the extremity of the beams. The reinforced beam stress simulations highlight two main points. First, it comforts the

hypothesis that the rigid body can be considered as a rigid element, as assumed in §2.1.3.2. Secondly, the stress magnitude in the reinforced pivot is of the same order as in the simple beams.

Displacement simulations for $\theta = +10^\circ$					
Parameters			Theoretical rotation	Simulated rotation	Error
Beam Type	b [μm]	M [Nm]	θ_{th} [$^\circ$]	θ_{sim} [$^\circ$]	$\epsilon = \frac{\theta_{sim} - \theta_{th}}{\theta_{th}}$ ϵ
reinforced	2	$5,40 \cdot 10^{-8}$	9,993	9,15	-8.4 %
reinforced	3	$1,82 \cdot 10^{-7}$	9,979	9,21	-7.7 %
reinforced	4	$4,32 \cdot 10^{-7}$	9,993	9,46	-5.5 %
reinforced	5	$8,44 \cdot 10^{-7}$	9,996	9,56	-4.4 %
simple	2	$3,08 \cdot 10^{-8}$	9,989	9,33	-6.6 %
simple	3	$1,04 \cdot 10^{-7}$	9,994	9,34	-6.5 %
simple	4	$2,46 \cdot 10^{-7}$	9,973	9,32	-6.6 %
simple	5	$4,81 \cdot 10^{-7}$	9,984	9,48	-5.1 %

Table 3.2: Angular displacement simulation. Simulation of a 10° rotation compared to the theoretical value. The material is supposed isotropic, $E=160\text{GPa}$. The simulated moment, applied on the pivot M , has been calculated depending on the beam width b in order to obtain a 10° rotation (Theoretical rotation θ_{th}). This value is compared to the simulated one (Simulated value θ_{sim}). The percentage of error is relative to the theoretical value.

These simulations show the good validity range of the stiffness equation of the simple and reinforced RCC pivots. In comparison to the previous 5° rotation simulation, the percentage of error is kept low and at the same order of magnitude. As for the previous simulations, the error increases as the beam width reduces.

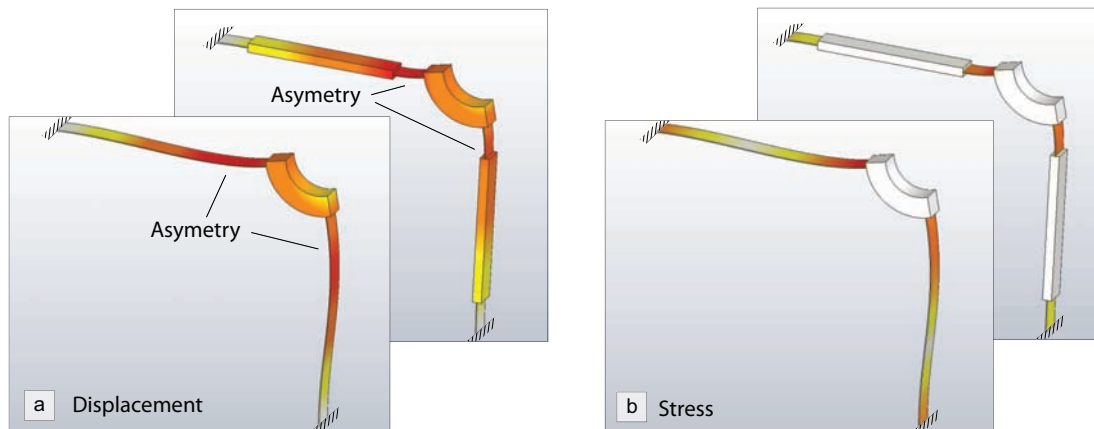


Figure 3.3: SolidWorks finite element analysis of the RCC reinforced pivot deformation for a 10° rotation (top) reinforced beam, (bottom) simple beam. (a) Displacement simulations: the color levels describe the displacement magnitude relative to the anchor, white= $0 \mu\text{m}$, red= $28 \mu\text{m}$; (b) Stress simulations: the color levels describe the von Mises stress magnitude, white= 0N/m^2 , red = $6,4 \cdot 10^8 \text{N/m}^2$.

In Figure 3.3, the stress distribution is the same as for the 5° rotation simulations. We

can notice that the beam's internal stress is kept under the yield strength of silicon, which is of $\sigma_Y = 7$ GPa [15]. The large rotation range of the butterfly pivot is confirmed by the simulations. However, the 10° simulation's rotation highlight a parasitic translation in addition to the rotation of the RCC pivot. This is particularly visible in Figure 3.3 on the reinforced RCC pivot displacement: the horizontal beam is more displaced than the vertical one. This observation is confirmed by S.Henein *et al.* [10] who states that the butterfly pivot is composed of four RCC pivots, where each one of these pivot motions can be described as a rotation and a parasitic translation.

S. Henien asserts that the key advantage of the butterfly pivot is the distribution of the total stroke over the four RCC pivot stages, and the center shift compensation between the stages. Indeed, the pairs of RCC pivots are arranged in a manner that makes their respective parasitic center shift compensate one another. This property of the butterfly pivot is studied in the following section.

3.1.2 Analytic model and butterfly pivot simulation comparison

After the simulations of the butterfly pivot's elementary component, we have simulated the static deformation of the whole butterfly pivot in order to confirm the parasitic center shift compensation of the serial RCC pivot, and to study the equations (2.1) and (2.3).

Here again, the simulated material's properties are assumed isotropic, as the equation does not take into account the anisotropy properties of silicon.

Butterfly angular displacement simulation					
Parameters			Theoretical rotation	Simulated rotation	Error
Beam Type	b [μm]	M [Nm]	θ_{th} [$^\circ$]	θ_{sim} [$^\circ$]	$\epsilon = \frac{\theta_{sim} - \theta_{th}}{\theta_{th}}$ ϵ
reinforced	2	$0,5 \cdot 10^{-8}$	3,70	3,40	-8.1 %
reinforced	2	$1 \cdot 10^{-8}$	7,40	6,77	-8.5 %
reinforced	2.5	$0,5 \cdot 10^{-8}$	1,89	1,76	-6.9 %
reinforced	2.5	$1 \cdot 10^{-8}$	3,79	3,51	-7.4 %
simple	2	$0,5 \cdot 10^{-8}$	6,49	6,29	-3.1 %
simple	2	$1 \cdot 10^{-8}$	12,97	12,39	-4.5 %
simple	2.5	$0,5 \cdot 10^{-8}$	3,32	3,24	-2.4 %
simple	2.5	$1 \cdot 10^{-8}$	6,64	6,46	-2.7 %

Table 3.3: Butterfly angular displacement simulation: Comparison of the simulated value with the value calculated. The material is supposed isotropic, with $E = 160$ GPa. The simulated moment applied on the pivot M is of $0.5 \cdot 10^{-8}$ Nm or $1 \cdot 10^{-8}$ Nm, with the two beam parameter width b of $2 \mu\text{m}$ and $2.5 \mu\text{m}$. The theoretical rotation (θ_{th}) obtained with this parameters (equations (2.1) and (2.3)) is compared to the simulated one (θ_{sim}). The percentage of error is relative to θ_{th} .

The torque M is fixed at $0.5 \cdot 10^{-8}$ Nm and $1 \cdot 10^{-8}$ Nm. The simulations of the reinforced beams differ more than in the case of simple beams, but they keep a good

conformity with the calculated values. It is however interesting to notice that the simulations fit well with the calculations, as the mesh could have been problematic. Indeed, the structure with high element size ratios are difficult to simulate, and such long structures are critical to simulate.

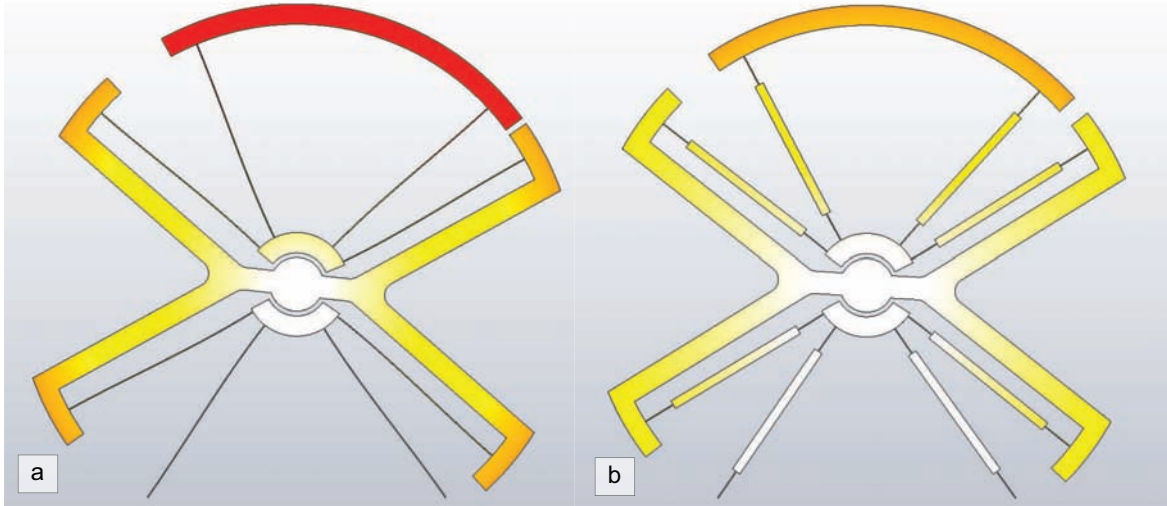


Figure 3.4: Butterfly angular displacement simulation: Deformation of a butterfly pivot with simple beams (a) and with reinforced beams (b) for a same applied torque of $1 \cdot 10^{-8}$ Nm. The beam width is $b = 2 \mu\text{m}$. The color levels describe the displacement magnitude relative to resting position, white = $0 \mu\text{m}$ and red = $135 \mu\text{m}$.

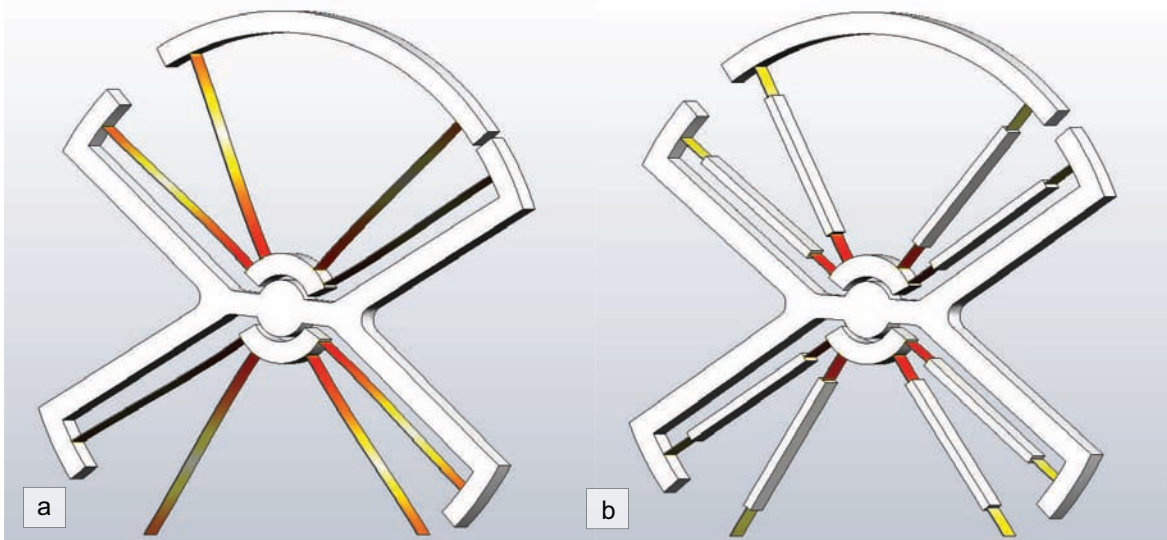


Figure 3.5: Butterfly angular stress distribution: Internal stresses of a butterfly pivot with simple beam (a) and with reinforced beam (b) for a same applied torque of $1 \cdot 10^{-8}$ Nm. The beam width is $b = 2 \mu\text{m}$. The color levels describe the von Mises Stresses magnitude relative to no stress, white = 0 N/m^2 , red = $1 \cdot 10^8 \text{ N/m}^2$.

Figure 3.4 shows the deformation of the butterfly pivot for the two types of beams. The deformation of the butterfly is, in both cases, a rotation with no parasitic translation. The parasitic center shift compensation between the RCC pivot advanced by S. Henein is confirmed by the simulations.

We can also observe that the stroke of the reinforced pivot is smaller than the simple one for a given torque. This was expected as we saw in §2.1.3.3 the reinforced beam increases the stiffness.

Figure 3.5 exposes the small effect of reinforced beams on the stress distribution. As the stress is concentrated in the extremity of the beams, the reinforced beam does not affect much the stiffness compared to the reduction of the active flexure beams. We will observe the effect of the reinforced beam on the buckling charge in §3.1.4.

3.1.3 Silicon orthotropic properties study

All the simulations shown in §3.1 and §3.1.2 have been realized with the material assumed isotropic, since we refer to theoretical equations for isotropic material. In the following section, we compare simulations of the whole butterfly pivot performed under the assumption that the material is either isotropic or orthotropic. Indeed, the silicon properties depend on the crystal orientation. The orthotropic properties (see Appendix A.3) and the simulations parameters have been defined following the simulations recommendation of Matthew A. Hopcroft in his article entitled “What is the Young’s Modulus of Silicon” [11]: The study is for (100) oriented silicon. The simple beam simulations have not been performed as the solver failed.

Orthotropic reinforced butterfly angular displacement simulation					
Parameters		Isotropic	Orthotropic	Error	$\epsilon = \frac{\theta_{iso} - \theta_{ortho}}{\theta_{ortho}}$
b [μm]	M [Nm]	θ_{iso} [$^\circ$]	θ_{ortho} [$^\circ$]		ϵ
2	$0,5 \cdot 10^{-8}$	3,40	4,10		-17.1 %
2	$1 \cdot 10^{-8}$	6,77	8,14		-16.8 %
2.5	$0,5 \cdot 10^{-8}$	1,76	2,12		-17.0 %
2.5	$1 \cdot 10^{-8}$	3,51	4.23		-17.0 %

Table 3.4: Orthotropic reinforced butterfly angular displacement simulation: Comparison of the simulated value with an orthotropic material with the value calculated for an isotropic material. The simulated moment applied on the pivot M is of $0.5 \cdot 10^{-8}$ Nm or $1 \cdot 10^{-8}$ Nm, with the two beam parameter width b of 2 μm and 2.5 μm . The simulated rotation angle θ_{iso} , with the isotropic material properties ($E = 160$ GPa), is compared to the simulated value θ_{ortho} , defined with orthotropic material. The percentage of error is relative to the orthotropic value.

The percentage of error is too large to be considered negligible. The influence of the orthotropic properties of silicon is important and must be taken into account. The stiffness equations of the butterfly pivot (equations (2.1) and (2.3)) and the resulting displacement depending on a load must be considered as an approximation in the case of single-crystalline silicon.

3.1.4 Buckling simulations

In this section, we present the buckling simulation performed on the beams and on the butterfly pivot.

Buckling simulations of the beams

The aim of this section is to observe and quantify the effect of the reinforced beam on the buckling factor of the butterfly pivot. The first simulations were performed on the beams itself. The simple beams and the reinforced one have been compared and we also change the material properties (isotropic or orthotropic).

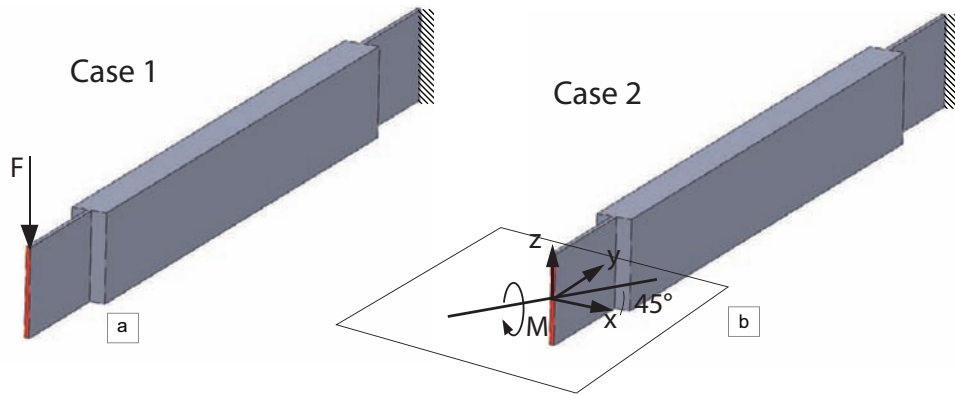


Figure 3.6: Buckling simulation: definition of the charges applied on the beam. (a) A force F is applied vertically on the beam. (b) The moment M is applied with an angle of 45° angle relative to the neutral axis of the beam.

The maximum force applied on the beam and the maximum torque before the buckling of the structure are summarized in Table 3.5.

Buckling simulations of the beam			
Parameters		Maximal Force	Maximal Torque
Beam Type	Material properties	F_{max} [μN]	M_{max} [Nm]
reinforced	isotropic	461,93	0
reinforced	orthotropic	489,65	0
reinforced	isotropic	0	$9,83 \cdot 10^{-8}$
reinforced	orthotropic	0	$9,89 \cdot 10^{-8}$
simple	isotropic	129,58	0
simple	orthotropic	141,51	0
simple	isotropic	0	$2,11 \cdot 10^{-8}$
simple	orthotropic	0	$2,13 \cdot 10^{-8}$

Table 3.5: Buckling simulations: Comparison of the maximum torque M_{max} and the maximum force F_{max} applied before buckling, depending on the beam type and on the material properties.

The results of the simulations highlight the positive effects of the reinforcement of the beams on the buckling charge: there is a factor four on the maximum torque, or

force applied, on the reinforced beams compared to the simple beams. The material anisotropy has a limited influence on the buckling charge limit.

Buckling simulations of the butterfly pivot

The buckling limit charge has also been simulated on the butterfly pivot. The simulation of this parameter is time consuming (in term of computing time) and the butterfly pivot with simple beams could not be simulated, as the solver failed. However, the reinforced butterfly pivot simulations ran well. The results are summarized in Table 3.6, depending on the material properties.

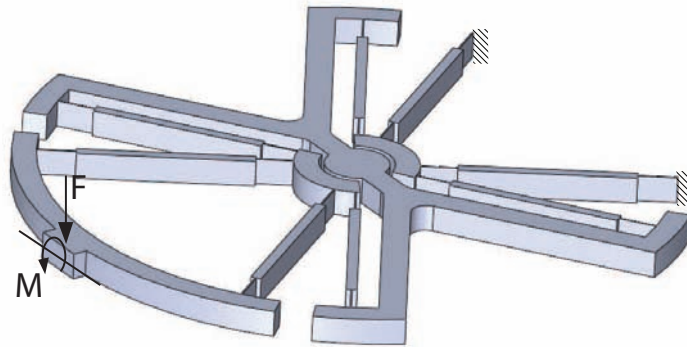


Figure 3.7: Buckling simulation: definition of the charges applied on the butterfly. A moment M is applied or a force F

Buckling simulations of the reinforced butterfly pivot		
Parameters	Maximal Force	Maximal Torque
Material properties	F_{max} [μN]	M_{max} [Nm]
isotropic	517,07	0
orthotropic	471,12	0
isotropic	0	$1,91 \cdot 10^{-7}$
orthotropic	0	$1,69 \cdot 10^{-7}$

Table 3.6: Buckling simulations: Comparison of the maximum torque M_{max} and the maximum force applied F_{max} before buckling depending on the beam type and on the material properties.

The influence of the material properties are not too strong as the buckling charge limit is of the same order of magnitude. The maximum torque before buckling is twice the buckling charge limit of the beam with the same parameters. As the butterfly structure weakest link is composed of two beams in parallel, this value is normal. However, the maximum force before the buckling of the butterfly does not respect this expectation. The value must be taken as an order of magnitude and not as an exact value.

These buckling load values, with respect to scaling laws, correspond to large loads at such scale. They indicates that the micromotor can be used in microrobotic applications.

3.2 Finite Element Modal Analysis

Having measured the dynamic behavior of the micromotor, we have simulated the frequency response of the complete micromotor. The eigenmode and the deformation shape of each modes have been extracted from the simulations.

The eigenmode results of the FEA simulations and the experimental modal analysis performed with the Polytec Microsystem Analyser MSA-400 are summarized in Table 3.7. This table highlights the high conformity of the simulations for the first 5 modes (with a discrepancy lower than 10%).

Modal simulation compared to experimental analysis			
Mode	FEA simulations	Experimental analysis	Remarks
1	170 Hz	163 Hz	In-plane see, Figure 2.19
2	683 Hz	665 Hz	In-plane, see Figure 2.19
3	2810 Hz	2616.4 Hz	Out-of-plane, see Figure 2.20
4	5350 Hz	5018.0 Hz	Out-of-plane, see Figure 2.20
5	6110 Hz	5726.6 Hz	Out-of-plane, see Figure 2.20

Table 3.7: Modal properties of the micromotor: comparison of the FEA simulations with the Polytec Micro System Analyser MSA-400 measurements. The comparison highlights a good similitude between simulations and experimentation (discrepancy lower than 10%).

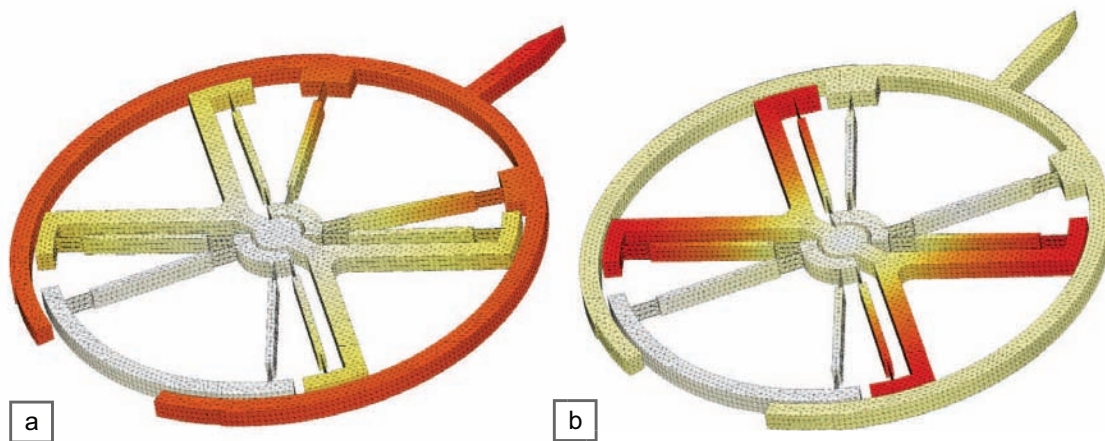


Figure 3.8: SolidWorks finite element modal analysis of the rotor's mechanical structure. The color levels describe the displacement magnitude relative to the anchor. We show the first eigenmodes occurring at 170 Hz (a), and 683 Hz (b). The first mode corresponds to the in-plane vibration of the rotor ring, while the second mode corresponds to the in-plane vibration of the internal butterfly pivot.

The results of the modal analysis study are shown in Figure 3.8. For these simulations, we have considered flexure beams with a width of $1.15 \mu\text{m}$. This dimension, which is within the optical measurement uncertainty, was chosen so as to obtain the best match between the simulated result and the experimental data for the first eigenfrequency. With this parameter, the first mode occurs around 170 Hz and corresponds

to the in-plane vibration of the rotor ring, while the second mode occurs around 683 Hz and corresponds to the in-plane vibration of the internal butterfly pivot.

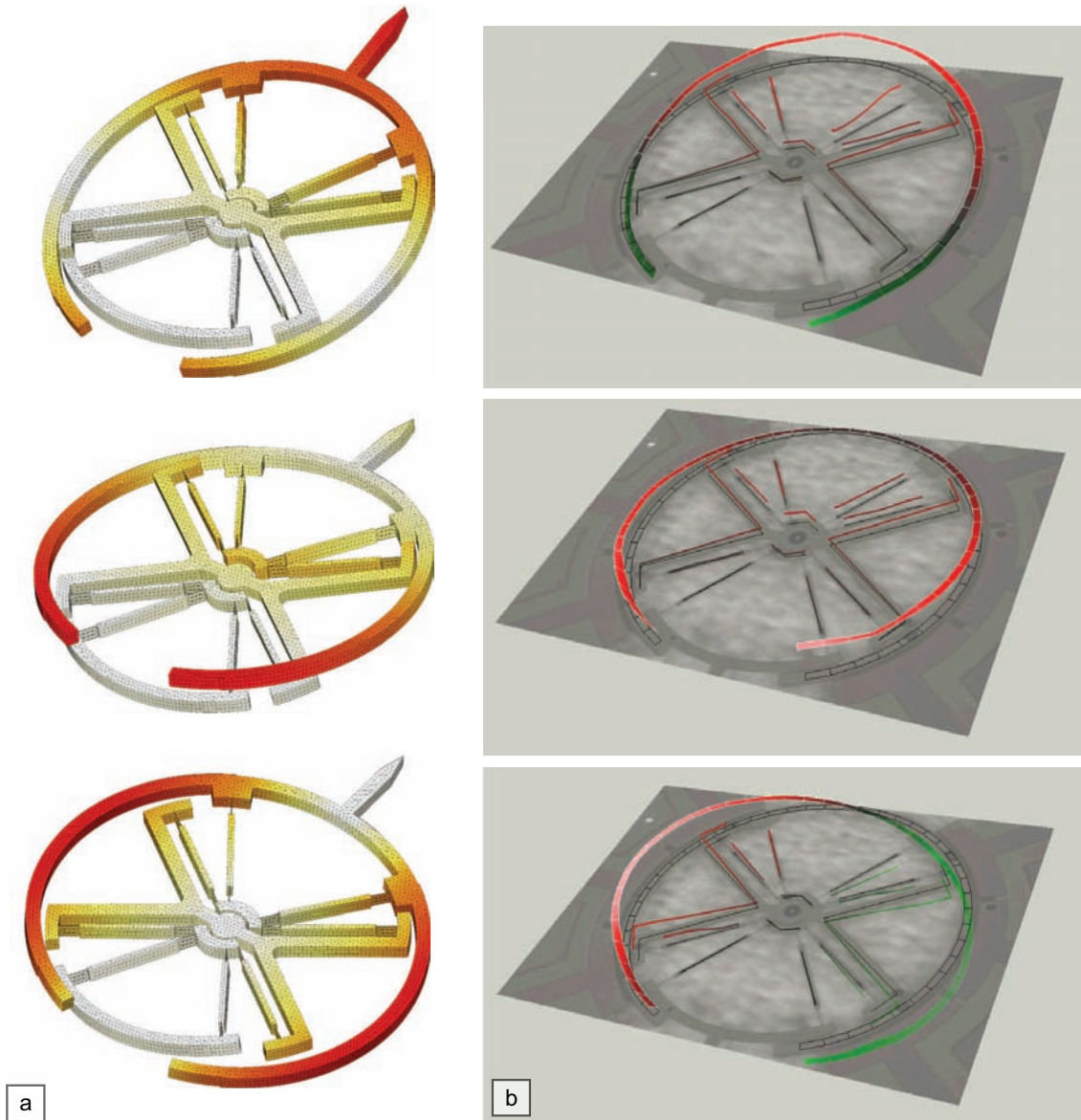


Figure 3.9: Modal analysis: (a) SolidWorks finite element modal analysis of the rotor's mechanical structure. The color levels describe the displacement magnitude relative to the anchor; (b) Out-of-plane measurements performed with Polytec MSA-400, reproduced from Figure 2.21. From top to bottom, we show the third, fourth and fifth eigenmode respectively.

The results of the FEA out-of-plane simulations are compared to the out-of-plane response obtained by Laser-Doppler vibrometry in Figure 3.9. These results exhibit the very good correspondence between the simulation and the experimental analysis.

3.3 Simulation Discussion

In this chapter, we have compared the simulation of different components of the butterfly pivot, and it appears that the equations (2.1) and (2.3) fit well with the simulations. However, the anisotropic properties of the silicon limit the application of this analytical equation, which should be considered as an approximation of the stiffness for anisotropic materials. Furthermore, the parasitic center shift compensation between the RCC pivot advanced by S. Henein is confirmed by the simulations.

The buckling simulations confirm the need of using reinforced beams: the internal stress is concentrated in the small flexure element without increasing significantly the density of stress. It results in an increase of the buckling charge limit. The simulations also confirmed the hypothesis considered in §2.1.3.2 to establish the analytical model. These buckling simulations indicate that the micromotor can be used in microrobotic applications.

Finally, the modal analysis exhibits a perfect concordance between the simulations and the experimental results.

Chapter 4

Measurement method

This chapter introduces the different measurement methods used in Chapter 5 for the dynamic characterization of the micromotors.

In this chapter, we will focus on the following points:

- In Section 4.1, we will give a succinct overview of the most common **optical measurement methods** used for MEMS characterization.
- In Section 4.2, we will describe the Polytec Micro System Analyzer (MSA-400) which has been used for several dynamic measurements. **Stroboscopic video microscopy** will be studied in detail because some limitations of the method have been encountered during experimental measurements.
- Section 4.3 will introduce the “**temporally aliased video analysis**¹”. This introduction is non-exhaustive. The reader is referred to [28] for additional details.

¹This denomination is taken from [28].

4.1 Review of optical measurement methods

We introduce in this section a succinct overview of the most commonly used optical measurement methods for MEMS characterisation. For a complete review of the optical measurement method, we refer the reader to the review article from Bosseboeuf *et al.* [5], used to establish this short review:

Optical profilometers (out-of-plane measurement, 2D or 3D profiles measurement) – The principle of this method is based on the detection of the focusing variation of a laser when a sample is scanned in xy -directions. A close-loop control of the position of sample is usually included in the system to increase the vertical resolution to 1-10 nm. The lateral resolution depends on the x and y stages.

Microscopic interferometry (out-of-plane measurement, 2D or 3D profiles measurement) – These measuring devices use the interferometry principle and can reach nanometer resolution. The samples are usually scanned using a piezoelectric stage. The vertical resolution achieved is in the range of tens of nm and the horizontal resolution is in the submicron range.

Laser deflection (out-of-plane vibration) – This measurement principle, used in Atomic Force Microscopy, is quite simple: a laser beam is focused on the oscillating element and the angle of reflected beam is measured. This is a very sensitive method well suited for resonant frequency measurement and low vibration amplitude measurement.

Laser Doppler vibrometry (out-of-plane vibration) – The laser Doppler vibrometry measures the phase shift and/or the optical frequency shift, induced by the Doppler effect, of a light beam reflected on the structure to be measured. This measurement method can achieve a detection limit of 10 pm.

High-speed camera image processing (in-plane vibrations) – The image processing of microscope recording is a common way to measure the in-plane motion. High frequencies can be measured with high-speed cameras as their frame rate respects the Sampling theorem (see §4.3.2). The resolution depends on the camera used and on the magnification.

Stroboscopic measurement (in-plane vibrations) – In stroboscopic oscillation measurement, short light pulses are synchronized with the excitation signal of the structure with a short variation Δf of the frequency. The apparent movement of the structures appeared to be at the frequency which correspond to the frequency difference Δf . Knowing the stroboscopic frequency, the oscillation frequency of the structure can be deduced.

Analysis of blurred images (in-plane vibrations) – In this method, the oscillating structure is recorded at a frame rate much lower than the oscillating frequency in order to obtain a blurred image. The eigenmodes are detected when the blurred amplitude is maximum.

4.2 Polytec Micro System Analyzer (MSA-400)

We introduce here the Polytec Micro System Analyzer (MSA-400, see Figure 4.1) as several measurements have been performed with this device.

This Micro System Analyzer is a state-of-the-art instrument composed of three different measuring devices combined in one measuring station. The three detection methods are:

- Surface profilometry by **laser interferometry**
- Out-of-plane vibration analysis by scanning laser Doppler vibrometry
- In-plane motion detection by **stroboscopic video microscopy**

The scanning laser vibrometry has been used to detect, measure and visualize the out-of-plane eigenmodes of the micromotor (see Figure 2.21 and 2.19) and the stroboscopic detection method to establish the in-plane frequency response of the micromotor, see Figure 2.19.



Figure 4.1: Polytec MSA-400: All-in-one state-of-the-art instrument dedicated to MEMS and microstructures' analysis. Figure reproduced from [8].

Stroboscopic video microscopy

We briefly remind here the measurement principle of the stroboscopic measurement, relevant during the interpretation of the results. This section will focus on a particular basic case of stroboscopic video microscopy and is not a complete theoretic review.

In a stroboscopic video microscopy measurement, the device to measure is excited at a frequency $f_{excitation}$ and the sample oscillates at a frequency f_{sample} . In this basic particular case study, the measurement instrument emits light pulses synchronized with the excitation frequency at a frequency $f_{pulse} = f_{excitation} + \Delta f$, slightly different of Δf from the excitation frequency $f_{excitation}$. During these light pulses, the camera shutter is opened and the image recorded. On the video recorded, the structure appears to move at a frequency $f_{stroboscopic} = \Delta f$ which corresponds to the frequency shift Δf between the excitation frequency and light pulses frequency [5].

For example, for an excitation frequency $f_{excitation} = 100Hz$ and the light pulses frequency at $f_{pulse} = 101Hz(f_{excitation} + \Delta f)$, the device motion “seems ” to oscillate at $f_{stroboscopic} = 1Hz(\Delta f)$.

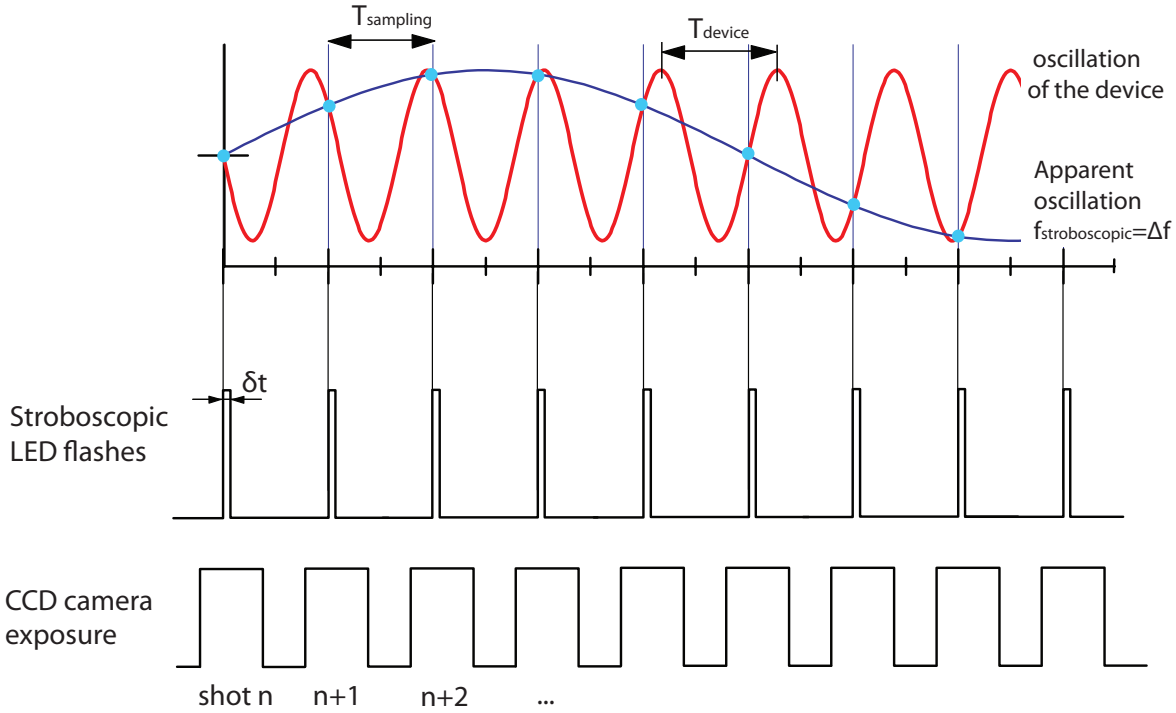


Figure 4.2: Stroboscopic measurement principle: The structure to measure oscillates at a frequency f_{sample} (of a period T_{sample}) supposed to be the same as the excitation frequency $f_{excitation}$ (of a period $T_{excitation}$). A stroboscopic light emits light pulses at a frequency $f_{stroboscopic}$ (of period $T_{stroboscopic}$) slightly different from the excitation frequency $f_{excitation}$. A CCD camera records the images of the stroboscopic illumination. The apparent oscillation frequency $f_{stroboscopic} = \Delta f$ is equal to the frequency shift between the excitation and the illumination.

Polytec Microsystem Analyser stroboscopic working principle

Figure 4.3 shows the working principle of the stroboscopic imaging implemented in the MSA-400, based on the principle presented above. The sample is excited with a sine of frequency $f_{excitation}$ to generate a periodic in-plane motion. Synchronised with the device in-plane motion, short LED light pulses freeze the object's position at precise phase angles φ .

In practice, the stroboscopic video microscopy of the Polytec Microsystem Analyser MSA-400 slightly differs from the principle since it needs enough time exposure (*e.g.* the sum of the light pulses) to illuminate the CCD camera. However, the measurement principle remains the same.

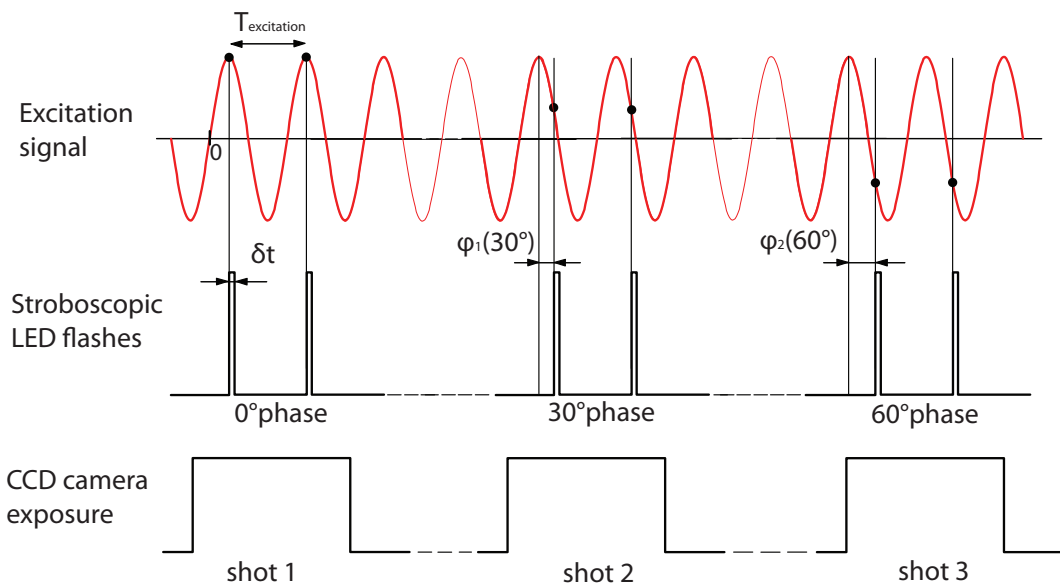


Figure 4.3: Timing diagram of the stroboscopic imaging method of the Polytec Microsystem Analyser MSA-400 used for in-plane motion analysis.

The Polytec Microsystem Analyser MSA-400 can automatically perform in-plane modal analysis of the structure following the procedure described in the following lines²:

1. A stroboscopic video recording of the device is performed at each frequency, defined by the user in a certain bandwidth, with a given number of steps.
2. Each video obtained for each frequency is analyzed by image processing to define the displacement
3. The signal obtained (position/time) is compared to a sine of frequency $f_{stroboscopic} = \Delta f$. **The amplitude for the frequency $f_{stroboscopic} = \Delta f$ of the signal (position/time) is extracted.**
4. The amplitude of motion depending on the frequency (amplitude modal analysis) is reconstructed from the previous point.

²Source: Polytec technical support [8], Polytec presentation and discussion, Polytec engineer, Sven Frank, (Workshop EPFL), the 25th August 2010.

Limitation of MSA stroboscopic method

The measurement method of the Polytec MSA-400 supposes that the structure oscillates at the frequency of excitation $f_{excitation} = f_{sample}$. However, if the structure oscillates at an other frequency, at frequency twice the excitation frequency for example, the procedure described above fails at step 3. Indeed, as illustrated in Figure 4.4, the amplitude at the frequency $f_{stroboscopic}$ contains within a signal at twice the excitation frequency does not correspond to the correct amplitude of the signal. This can be compared to the study case as the MSA-400 is based on this principle.

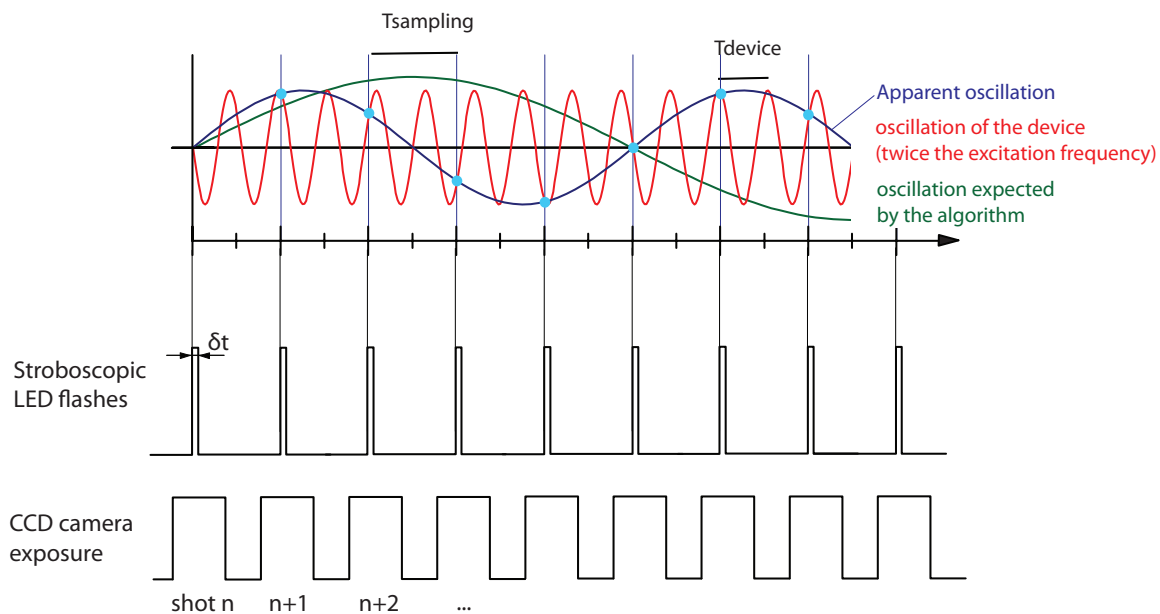


Figure 4.4: Stroboscopic measurement for a device oscillating at twice the excitation frequency.

4.3 Temporally aliased video analysis

This section presents a measurement method based on **temporally aliased** video analysis [28]. The purpose of this chapter is to introduce the measurement principle and this can not be considered as a complete explanation of the method. This section is included to the Master project's report as the temporally aliased video analysis measurement method is not yet published. For more informations, we refer to [28]. In order to explain the method, we introduce the program used to analyze videos in 4.3.1, then the aliasing notion in §4.3.2.

4.3.1 Discrete Fourier Analysis of video recording

We present here the tool used to analyze the video recording: an image processing algorithm to detect motion in video microscopy. The image processing is performed by a MATLAB-based dedicated software in which in-plane linear displacements of microelectromechanical systems are measured with subnanometer accuracy by observing the periodic micropatterns with a charge-coupled device (CCD) camera attached to an optical microscope. The translation of the microstructure is retrieved from the video by phase-shift computation, using discrete Fourier transform analysis [29]. This discrete Fourier transform analysis has been demonstrated for quasi-static motion and high speed camera recording. In both cases, the Sampling theorem is respected.

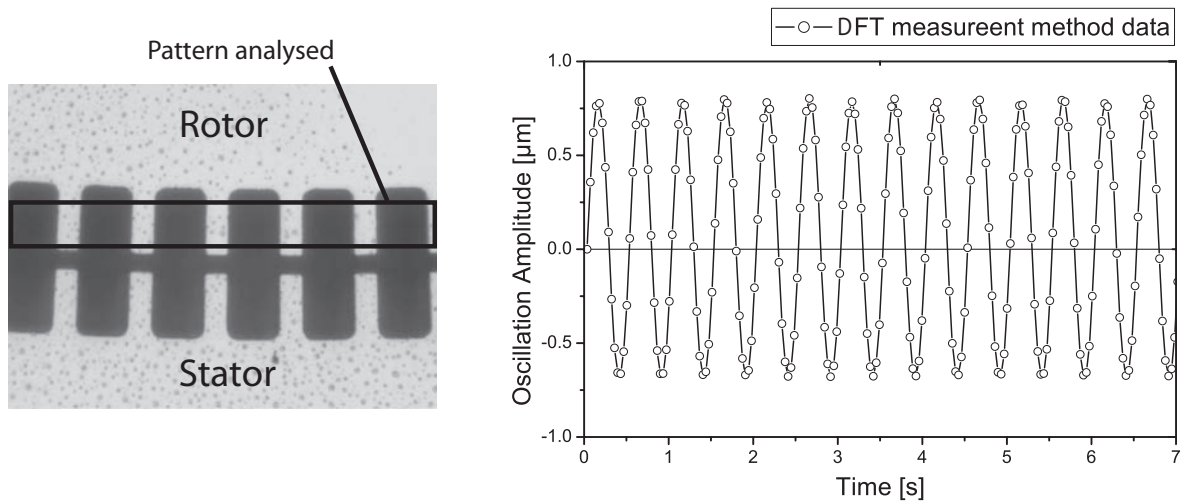


Figure 4.5: Discrete Fourier Analysis of video recording: A CCD camera attached to a microscope records a moving periodic pattern, in this case the rotor's teeth of the micromotor. The recorded video is analyzed and the displacement of the structure depending on the time is extracted [29]. The shutter opening time of the CCD camera must be short enough to obtain a non blurred image.

Figure 4.5 shows a typical Discrete Fourier Analysis of video recording, named DFT in the frame of this project. A pattern is recorded and analyzed using DFT analysis. The displacement of the structure depending on the time is extracted, in this case with a sampling rate respecting the Sampling theorem.

4.3.2 Aliasing and the sampling theorem

We present in this section the aliasing and the sampling theorem. The aliasing occurs when two signals become indistinguishable after sampling. In other words, the signal can not be reconstructed from its discrete (sampled) signal and is non distinguishable from another, as illustrated in Figure 4.6.

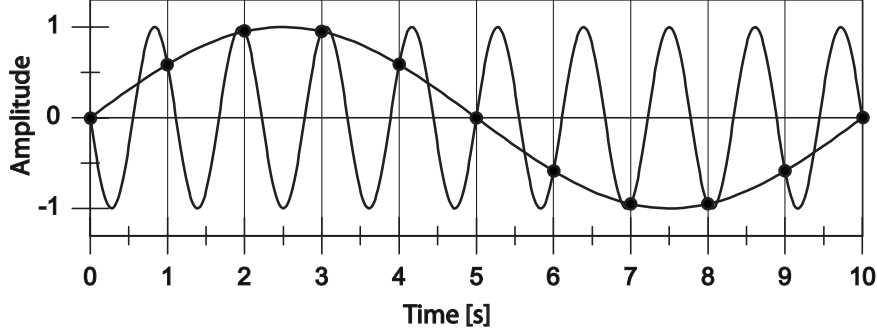


Figure 4.6: Aliasing example: The two signals, blue and red, are non distinguishable after sampling.

The Nyquist rate f_N - can be defined as the minimum sampling rate required to avoid aliasing. The Nyquist rate f_N is equal to twice the highest frequency $f_{signal,max}$ contained within the signal (for a bandlimited signal of $BW=0-B, f_N = 2B$) [13]:

$$f_N = 2f_{signal,max} = 2B \quad (4.1)$$

The sampling theorem states that the sampling frequency $f_{sampling}$ of a signal must be higher than the Nyquist rate f_N in order to reconstruct this signal from the samples [13]:

$$f_{sampling} > f_N \quad (4.2)$$

In classical video motion analysis, the sampling theorem is respected as the frame rate, which corresponds to the sampling frequency, is twice higher than the motion frequency. Figure 4.5 is an example of classical video analysis.

When the Sampling theorem is not respected, the signal is said *undersampled*.

4.3.3 Temporally aliased video analysis

The temporally aliased video analysis consists of using the algorithm described above in order to compute undersampled motion recording. In the frame of this project, we focus on the use of this method for modal analysis: the device to measure is excited with a swept frequency and the motion is recorded with a frame rate $f_{sampling} = f_s$ which does not respect the Sampling theorem. The shutter of the camera is opened during a time $t_{shutter} = 1/5000$ s short enough to obtain a net picture of each frame. A simple way to “comprehend” this method is the following: the “random” position of an oscillating device is measured within its maximum motion amplitude range for a known excitation frequency.

We introduce in Figure 4.7, an example: the data obtained for a sine chirp of voltage $V(t)$ from a frequency $f_{start} = 1$ Hz to $f_{stop} = 1$ KHz in a time $t_{sweep} = 4$ minutes. The device measured is a push-pull actuator [2].

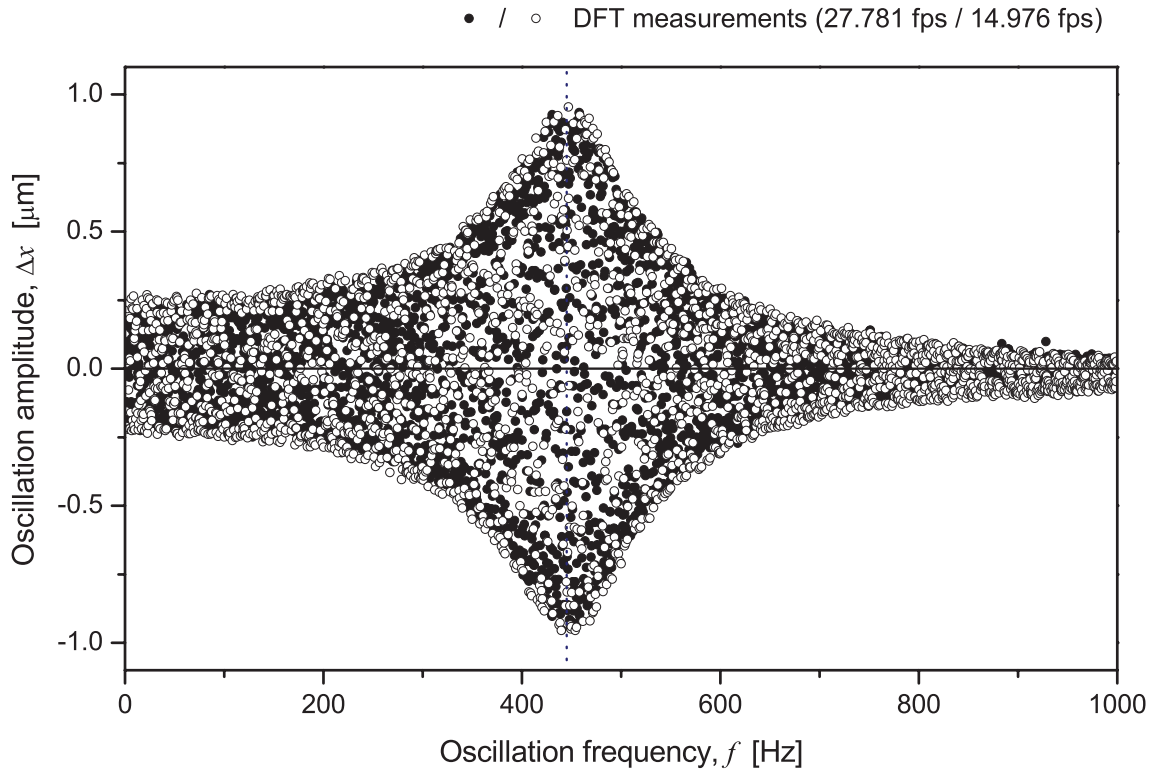


Figure 4.7: In-plane dynamic characterisation of a push-pull actuator. Video recorded with the Keyence VHX-600. Shutter set to 1/5000 sec, frame rate of 27.781 fps, sine sweep: 1 Hz to 1 KHz in 4 min.

The resulting data obtained does not allow the reconstruction of the signal but the amplitude of the oscillation is contained within envelope of the discrete sampled signal. With this information, the resonance frequency can be detected in the sweep of frequency. Of course, the “sweep duration”, $t_{sweep} = t_{start} - t_{stop}$, must be long enough to obtain a dense discrete signal in order to detect the envelop of the signal.

In order to perform the measurement above, the video recording must be synchronized with the camera in order to know to which excitation frequency the detected resonance frequency corresponds. There are two possibilities. Firstly, synchronize the camera and the function generator by a Labview program for example. This option needs an appropriate function generator and camera which can be synchronized. The other option is described in the lines below.

4.3.4 Signal and camera synchronization

A closer analysis of the discret signal from Figure 4.7 highlights node-like behavior at multiples of the Nyquist frequency $\frac{f_s}{2}$, as illustrated in Figure 4.8.

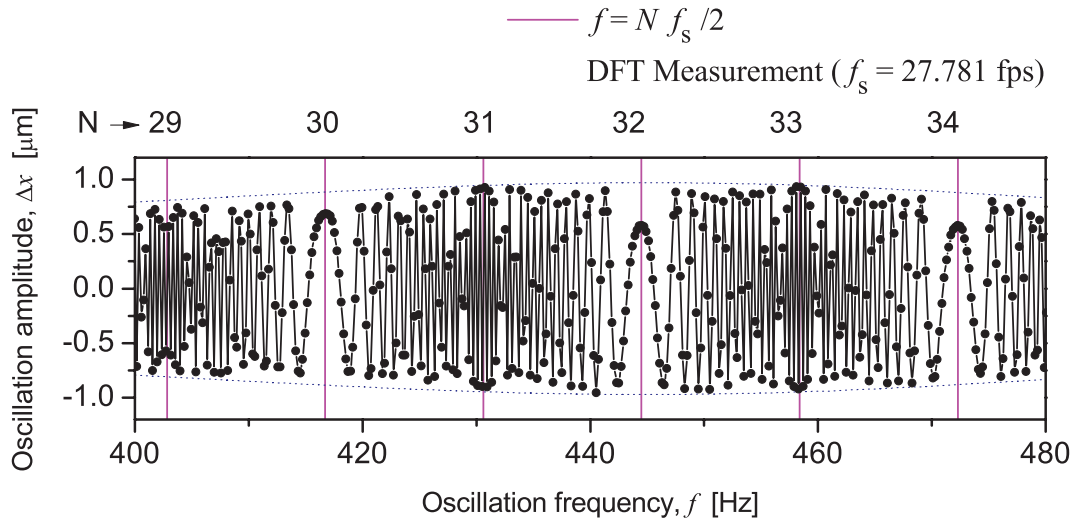


Figure 4.8: Stroboscopic freezing for $f = N \cdot \frac{f_s}{2}$

This is a form of stroboscopic freezing effect: for frequencies f that are multiple of the frequency $f = N \cdot \frac{f_s}{2}$, the apparent motion either appears as frozen (for $f = N \cdot \frac{f_s}{2}$, $N = 2, 4, 6, 8, \dots$) or as bistable (for $f = N \cdot \frac{f_s}{2}$, $N = 1, 3, 5, 7, \dots$). This effect is visible in Figures 4.9 and 4.10.

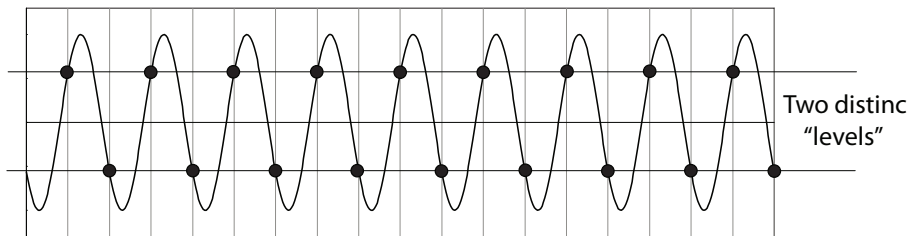


Figure 4.9: Apparent bistable state: the sampling frequency is of the form $f = N \cdot \frac{f_s}{2}$, $N = 1, 3, 5, 7, \dots$

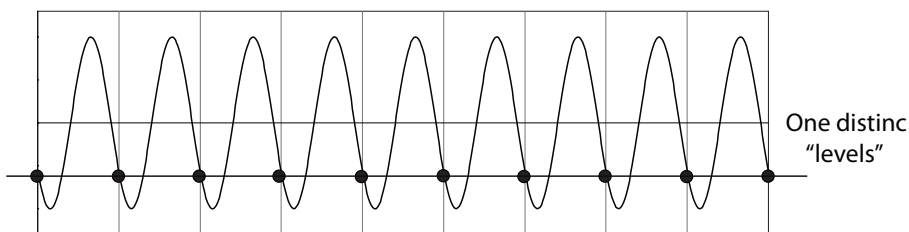


Figure 4.10: Apparent frozen state: the sampling frequency is of the form $f = N \cdot \frac{f_s}{2}$, $N = 2, 4, 6, 8, \dots$

This phenomenon can be used to synchronize the data obtained after image processing. This property can be problematic if the resonance peak to measure is exactly at the frequency of a node, but it can be avoided by choosing another frame rate.

Chapter 5

Dynamic characterization of the stepper micromotor

The experimental modal analysis presented in Chapter 2 has been performed by stroboscopic video microscopy using the Polytec Micro System Analyzer MSA-400¹. In this chapter, we complete the study of the micromotor presented in §2.2.2 with the following measurements:

- **Dynamic characterization** using the “temporally aliased video microscopy” method presented in Section 4.3. The motion of the device has been recorded with a standard CCD camera mounted on a Keyence VHX-600 microscope (see also Appendix A.4).
- Measurement of the **transient response** recorded with a high speed camera. Contrary to the “temporally aliased video analysis”, the motion of the device was recorded at a frame rate respecting the sampling theorem. Using the technique described in [29], the data extracted from the high speed camera have been used to measure the oscillation frequency and transient response.

In Section 5.1 and Section 5.2, we will compare these results with those obtained by stroboscopic video microscopy. In Section 5.3, we will demonstrate the “electrostatic stiffening”.

¹These measurements have been performed at the University of Twente, MESA+, The Netherlands. Therefore, no additional measurement with this method could be performed in the frame of this Master Project.

5.1 Case I: Sine excitation with a DC offset

5.1.1 Driving signals

We want to compare the stroboscopic MSA-400 measurements with the temporally aliased video microscopy. For that purpose, we have chosen identical driving signals to the one used during the previous MSA-400 measurements. The driving voltage $U_i(t)$ of phase i (the index i refers to the corresponding phase, $i = 1, 2, 3$) is of the form²:

$$\begin{aligned} U_1(t) &= 0; & U_2(t) &= U_{2,DC} + \hat{U}_{2,ac} \sin(\omega_{dr} t); & U_3(t) &= 0; \\ U_{2,DC} &= 1 \text{ V}, & \hat{U}_{2,ac} &= 1 \text{ V}, \end{aligned} \quad (5.1)$$

where the indexes DC and ac refers to constant voltages and alternatives voltages respectively. The actuators motion amplitude A is proportional to the electrostatic torque M_{el} and depends quadratically on the applied driving voltage U , see equation 2.8:

$$A \propto M_{el} \propto U^2.$$

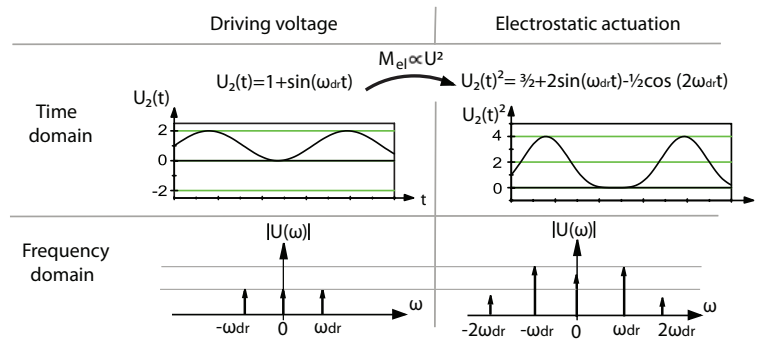


Figure 5.1: Signals: (left) Driving signal; (right) Excitation signal composed of two frequencies, see the equation 2.8.

Driving voltage	Electrostatic excitation	
$f_{dr} = \frac{\omega_{dr}}{2\pi}$	$f_{exc,1} = \frac{\omega_{dr}}{2\pi} = f_{dr}$	$f_{exc,2} = \frac{2\omega_{dr}}{2\pi} = 2f_{dr}$
$U(\omega_{dr}) = 2V_{pp}$	$U(\omega_{dr})^2 = 4V_{pp}^2$	$U(2\omega_{dr})^2 = 1V_{pp}^2$

Table 5.1: Driving signal frequency and excitation signal frequencies.

The electrostatic excitation signals are distinct from the driving voltage, composed of two frequencies, $f_{exc,1}$ and $f_{exc,2}$, see Table 5.1 and Figure 5.1. **For convenience, we will expose all the measurement in each figure depending on the electrostatic excitation frequencies.**

In Figure 5.2, the main excitation frequency $f_{exc,1}$ is the driving frequency f_{dr} . For this reason, this frequency is well suited for stroboscopic measurements. However, the second frequency $f_{exc,2}$, even with a lower amplitude, excites the device at twice the

²This driving signal is recommended by Polytec for its MSA-400.

driving frequency. The resulting oscillation can not be detected with the MSA-400, as discussed previously in chapter 4.

5.1.2 Experimental measurements

Figure 5.2 shows the experiments performed with the stroboscopic video microscopy and the temporally aliased video microscopy of the rotor (top) and the butterfly internal structure (bottom) for the excitation signal summarized in Table 5.1.

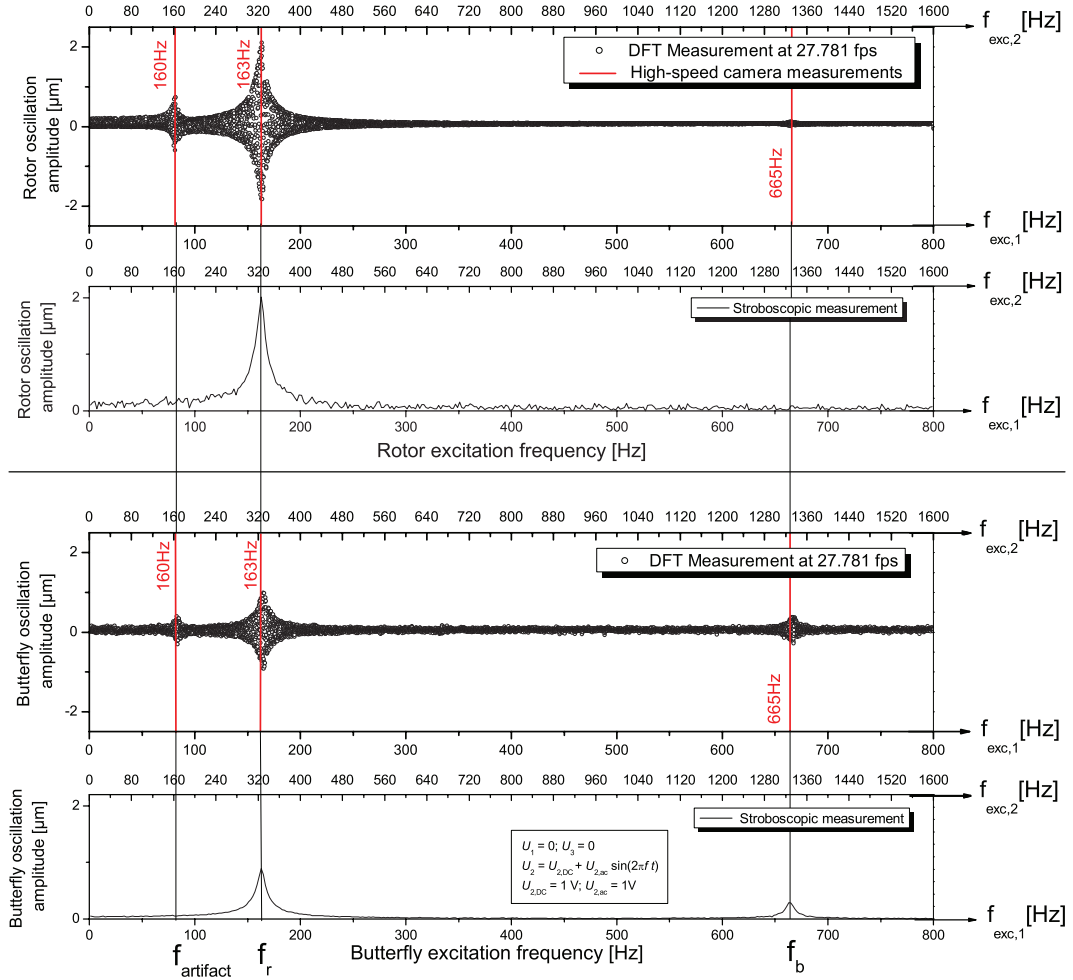


Figure 5.2: Comparison between the stroboscopic video microscopy and the temporally aliased video microscopy performed on the two-mask micromotor. Temporally aliased video microscopy: video recorded with the Keyence VHX-600. Shutter set to 1/5000 sec, frame rate of 27.781 fps, linear sine voltage chirp: $f_{dr} = 1$ Hz to 400 Hz in 5 min. In red are reported additional measurements performed with a high speed camera showing that the oscillations occurring driving voltage of $f_{dr} = 81.5$ Hz oscillate at $2f_{dr} = 163$ Hz (see also Figure A.5 and Appendix A.5).

We observe a good concordance of the two measurement methods concerning the amplitude of oscillation and in-plane resonant frequencies. However, the resonant frequency occurring at frequency $f_{artifact} = 81.5$ Hz is not detected by the MSA-400. Indeed, this resonant peak is an artifact that is excited by the frequency $f_{exc,2} = 2f_{dr} = 163$ Hz for a driving voltage frequency $f_{dr} = 81.5$ Hz. It is not detectable with the MSA-400 stroboscopic method described in §4.2, as the oscillation frequency is different from the driving

frequency. The amplitude of the artifact peak is smaller since the excitation amplitude $|U(2\omega_{dr})^2|$ is smaller than for the main excitation frequency $|U(2\omega_{dr})^2| = \frac{1}{4} |U(\omega_{dr})^2|$. The high speed camera measurement confirmed this hypothesis (see also Figure A.5 and Appendix A.5). We observe that the oscillation occurring for an excitation frequency of 81.5Hz are actually oscillating at $f_{exc,2} = 163Hz$.

This measurement highlights that the driving signal recommended by Polytec was not chosen judiciously, as it is composed of several excitation frequencies. However, it also illustrates that the temporally aliased method is more robust than the stroboscopic because it does detect the oscillation amplitude occurring at any frequency.

5.2 Case II: Pure sine excitation

5.2.1 Driving signals

In order to confirm the previous measurement interpretation, another driving voltage has been chosen to obtain an excitation signal composed of only one frequency. The sine driving voltage signal $U_i(t)$ is of the form:

$$\begin{aligned} U_1(t) &= 0; & U_2(t) &= \hat{U}_{2,ac} \sin(\omega_{dr} t); & U_3(t) &= 0, \\ & & \hat{U}_{2,ac} &= 2V, & & \end{aligned} \quad (5.2)$$

where $\hat{U}_{2,ac}$ was chosen so as to keep the same excitation amplitude as in §5.1. The electrostatic excitation, which depends on the square value of the driving voltage, is only composed of one frequency, $f_{exc,2} = 2f_{dr}$, with the same amplitude as for the previous excitation signal (see Table 5.1 and Figure 5.1).

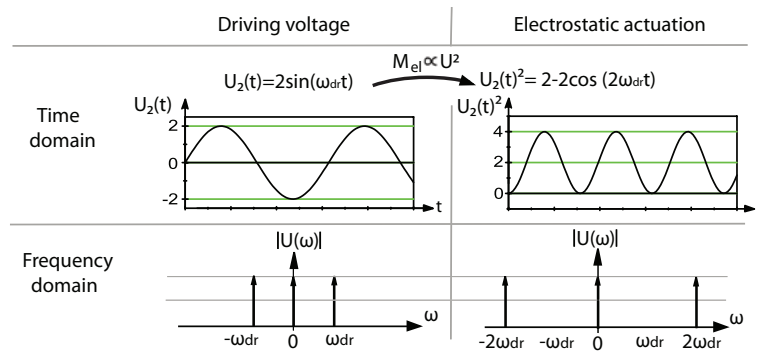


Figure 5.3: Signals: (left) Driving signal; (right) Excitation signal composed of one frequency.

Driving voltage	Electrostatic excitation
$f_{dr} = \frac{\omega_{dr}}{2\pi}$	$f_{exc,1} = \emptyset, \quad f_{exc,2} = \frac{2\omega_{dr}}{2\pi} = 2f_{dr}$
$U(\omega_{dr}) = 4V_{pp}$	$U(2\omega_{dr})^2 = 4V_{pp}^2$

Table 5.2: Driving signal frequency and excitation signal frequency.

5.2.2 Experimental measurements

Figure 5.4 shows the oscillation amplitude of the rotor (top) and butterfly internal structure (bottom) for a pure sine driving voltage signal recorded by “temporally aliased video microscopy”. The red lines show the measurement performed with a high speed camera.

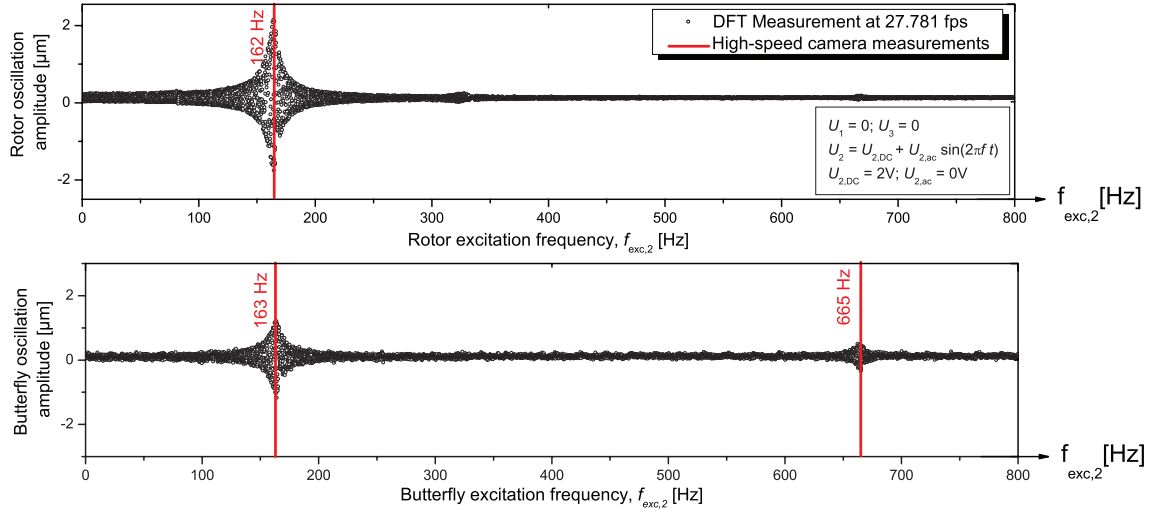


Figure 5.4: Frequency response of the two-mask micromotor. The oscillation amplitude of the rotor and butterfly internal structure have been measured using the temporally aliased video microscopy analysis measurement method recorded with the Keyence VHX-600, shutter set to 1/5000 sec, frame rate of 27.781 fps, linear sine voltage chirp: $f_{dr} = 1$ Hz to 400 Hz in 5 min. Red lines show the additional measurement performed with an high speed camera. For these recordings, the device oscillate at frequency equal to $f_{exc,2} = 2f_{dr}$.

These measurements confirm that the resonant frequency occurring at 81.5 Hz was actually an artifact of the actuation.

We can then conclude that the temporally aliased video analysis measure the amplitude of oscillation independently of the excitation frequency. For this reason, the excitation signal should be composed of only one frequency; otherwise the frequency response interpretation could be misled. (For example, the oscillation peak at 80Hz in Figure 5.2 could be wrongly interpreted as an eigenmode).

From §5.1 and §5.2 , we can conclude that the temporally aliased video analysis has the advantage of measuring the amplitude independently of the excitation frequency. With this property, the abnormal or unexpected frequencies can be observed.

5.2.3 Nonlinearities

After a carefully observation of Figure 5.4, we can notice small oscillation variations at excitation frequencies of $f_{exc} = 80$ Hz and $f_{exc} = 320$ Hz. This can be explain by the nonlinearities of the system. Indeed, as we will discuss in chapter 6, nonlinear systems can exhibit subharmonics and superharmonics oscillations [16]. The subharmonics oscillations involve oscillation of the device at frequencies $f_{sub,n}$ related to the excitation frequency f_{exc} by:

$$f_{sub,n} = \frac{f_{exc}}{n}, \quad (5.3)$$

where $n = 1, 2, 3, \dots$, and the superharmonic oscillations involve oscillations at frequencies $f_{sup,n}$, related to the excitation frequencies f_{exc} by:

$$f_{sup,n} = n \cdot f_{exc}. \quad (5.4)$$

In the case of our micromotor, a subharmonic of frequency $f_{sub,2} = \frac{f_{exc}}{2}$ and a superharmonic of frequency $f_{sup,2} = 2f_{exc}$ are visible, see Figure 5.5.

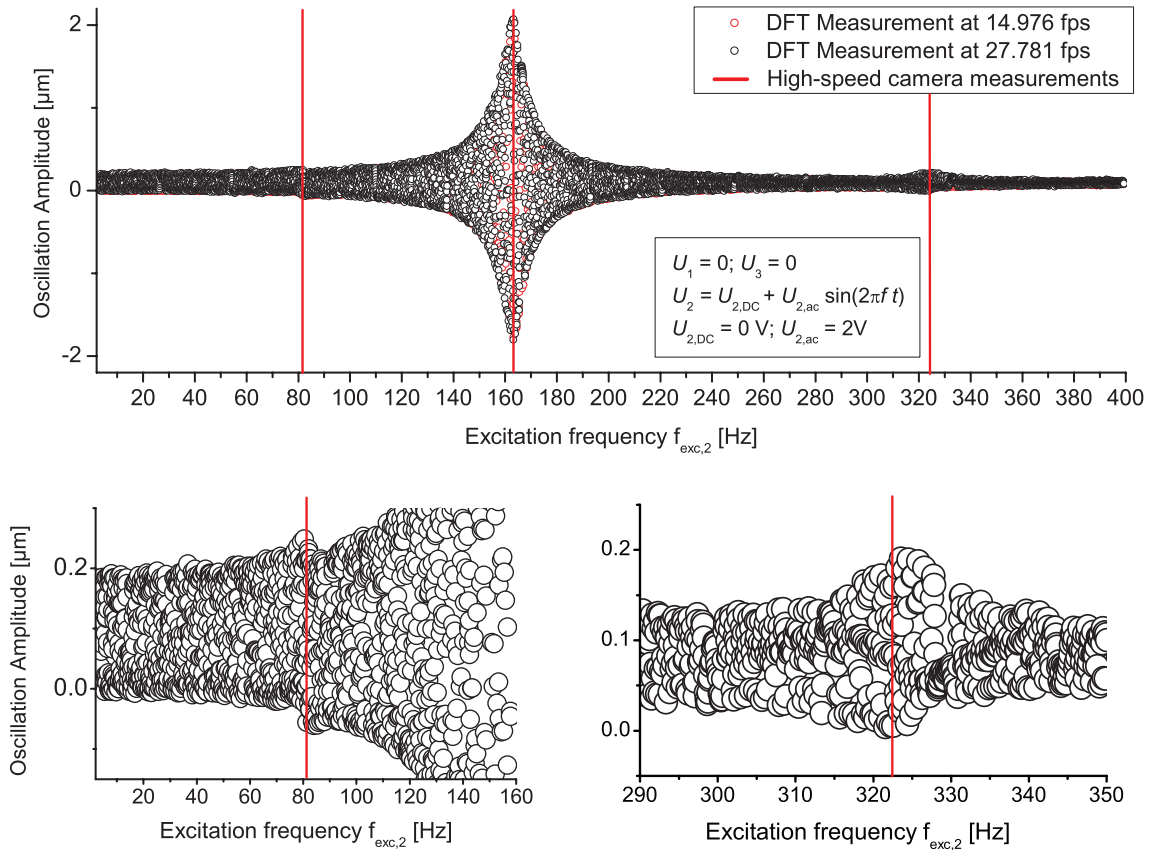


Figure 5.5: Nonlinearities observed with the temporally alised measurement video microscopy (recorded with the Keyence VHX-600. Shutter set to 1/5000 sec, frame rate of 27.781 fps and 14.976 fps, sine voltage sweep: $f_{dr} = 1$ Hz to 200 Hz in 5 min.). Oscillation variations occur at 81.5 Hz and 326 Hz.

This phenomenon was observed more clearly for higher voltage actuations (not shown in this report). We notice that these nonlinearities have not been detected by the Polytec MSA-400.

Chapter 6 will be devoted to the modeling of the micromotor, and the non-linearities will be discussed in more details and compared to the experimental results.

To complete these results, we show in Figure 5.6 the “folding frequency nodes” occurring at frequencies $N \cdot \frac{f_s}{2}$. This Figure illustrates the explanations given in §4.3.4.

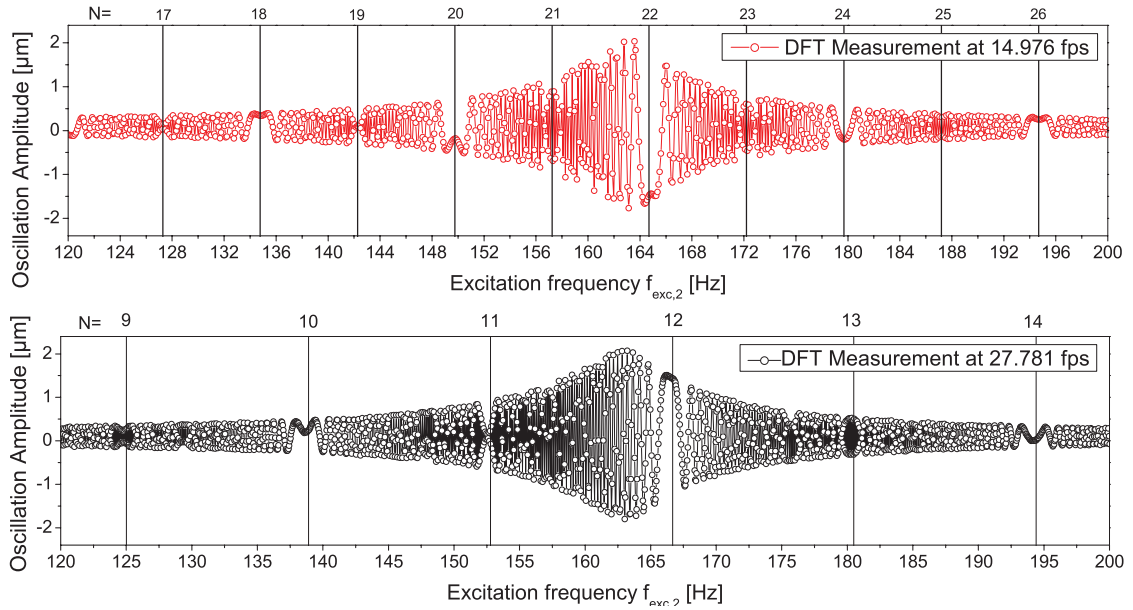


Figure 5.6: Temporally aliased video microscopy, detail of Figure 5.5: The “folding frequency nodes” occurring at $N \cdot \frac{f_s}{2}$ can be used as references for postprocessing of the data. The frame rate should be chosen appropriately so as to avoid superposition of the nodes with the eigenmode. (video recorded with the Keyence VHX-600. Shutter set to 1/5000 sec, frame rate of 27.781 fps and 14.976 fps, linear sine voltage chirp: $f_{dr} = 1$ Hz to 200 Hz in 5 min.)

5.3 Case III: Electrostatic stiffening

In §5.2, we have measured the frequency response in the case of an excitation on one phase only. Here, we performed a specific two phases actuation. The aim of this experiment was to observe the effect of a DC voltage applied on phase 1, while the phase 2 is activated with an AC voltage.

5.3.1 Driving signals

The driving voltage $U_i(t)$ is of the form:

$$\begin{aligned} U_1(t) &= U_{1,DC} = \text{const}; & U_2(t) &= \hat{U}_{2,ac} \sin(\omega : \text{drt}); & U_3(t) &= 0, \\ & & \hat{U}_{2,ac} &= 2 \text{ V}, & & \end{aligned} \quad (5.5)$$

5.3.2 Experimental measurements

Figure 5.7 exhibits the results extracted from a series of temporally aliased video analysis. The resonance frequencies of the rotor and butterfly structure is reported for various values of $U_{1,DC} = 0, 5, 10, 15, 20, 25$ and 30 V .

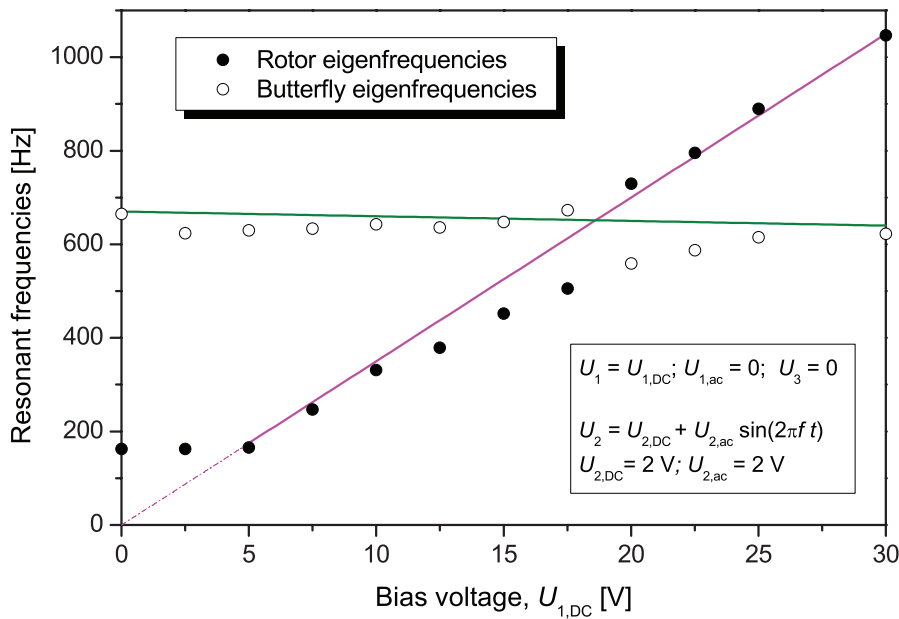


Figure 5.7: Electrostatic stiffening: The rotor eigenfrequency increases when a DC voltage is applied on phase 1. The eigenmode corresponding to the butterfly internal structure remains relatively constant. Figure reproduced from [22].

In Figure 5.7, we demonstrate that the first resonant frequency can be tuned by “electrostatic stiffening” [23]. The graph was obtained from data like those shown in Figure 5.4. When a DC voltage is applied on phase 1 ($U_{1,DC} = \text{const.}$) while the AC excitation is performed on phase 2, an electrostatic force tends to keep the rotor’s

teeth aligned with phase 1. The rotor is directly affected by the stiffening while the butterfly – which is mechanically connected with flexure beams to the rotor – keeps its own degree of freedom, even when the rotor is firmly blocked. As a result, the butterfly eigenmode remains relatively constant while the rotor eigenmode increases almost linearly with U_1 . This behavior is consistent with the FEA reported in §5.3.3.

5.3.3 FEA simulations

This behavior is well reproduced with the in-plane FEA simulations, see Figure 5.8. The butterfly’s resonant frequency is similar for a rotor completely free or firmly blocked. Here again, the electrostatic stiffening effect will be discussed and further understood in chapter 6. This effect is important as it influences the micromotor motion and transient response.

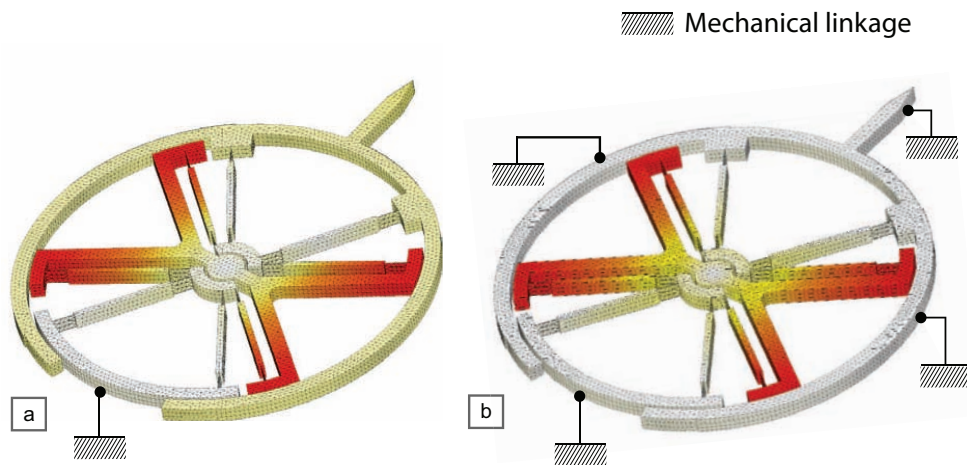


Figure 5.8: Electrostatic stiffening influence on the rotor resonant frequency. The color levels describe the displacement magnitude relative to the anchor. (a) FEA simulation with a rotor completely free: the 2nd mode corresponds to the butterfly resonant mode at 683Hz, reproduced from Figure 3.8 (b) FEA simulations with the rotor blocked, corresponding to an “infinite stiffening” of the rotor: the first resonant mode corresponds to the butterfly resonant mode at 657Hz.

Figure 2.17 particularly highlight the electrostatic effect in the micromotor displacement: the resting position at 9° is kept by the electrostatic stiffening occurring on phase 2 and 3. The transient oscillations are directly linked to the voltage applied and disturb the positioning of the micromotor.

Chapter 6

Mathematical model of the 3-phase stepper micromotor

In this chapter, we will establish a complete mathematical model that includes both the mechanical properties and the electrostatic actuation. We will focus on the following points:

- In Section 6.1, we will establish the complete **mathematical model**.
- In Section 6.2, using the software Maple 13, we will perform **numerical applications** corresponding to each of the cases presented in Chapter 5.

Under the assumption of small displacements, we will establish a simplified model of the micromotor. Moreover, the butterfly second resonant mode will not be considered, as its dynamic properties are known (see Section 5.3).

6.1 Modeling of the micromotor

6.1.1 Geometrical model

In order to establish an analytical model of the micromotor, we first introduce the simplified geometrical model. In this chapter, we will consider the butterfly pivot as a linear spring. In addition, the internal butterfly structure dynamic behavior will not be considered in this model.

As the model will be mainly used for dynamic modal analysis with very small displacement, the motion of the rotor can be simplified to a linear displacement. This model is valid for a circular motion with the proper substitution (see Appendix A.6).

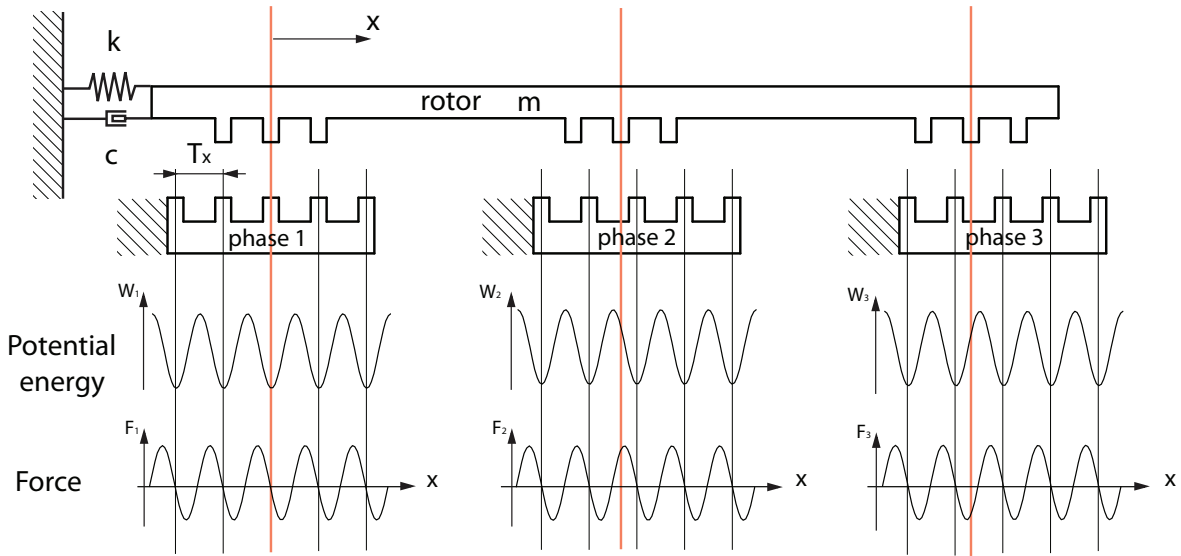


Figure 6.1: Model of a 3-phases linear stepper micromotor: the rotor of inertial mass m damped by a coefficient c and guided by a spring of stiffness k is actuated by three phases, each being composed of teeth separated with a period T_x . Each group of the stator teeth, corresponding to the phases 1, 2 and 3, are distributed with a respectively teeth misalignment of 0, $T_x/3$ and $2T_x/3$. The red vertical lines show resting position of each phase. The potential energy and the force acting on the rotor for each phase is shown under the corresponding phase for a given voltage $U_i = \text{const}$.

The rotor of inertial mass m damped by a coefficient c and guided by a spring of stiffness k is electrostatically actuated by three phases, each one composed of teeth of spacial period T_x . Each group of the stator teeth, corresponding to the phases 1, 2 and 3, are distributed with a respectively teeth misalignment of 0, $T_x/3$ and $2T_x/3$.

6.1.2 Actuation model

The driving force $F_{dr,i}$ of the stator phase i acting on the rotor is calculated below. From this equation, the expression of the global driving force of the three phases will be expressed.

The driving force $F_{dr,i}(x, t)$ of the stator phase i ($i=1,2,3$), acting on the rotor, is expressed as the derivation of the electrostatic potential energy W_i of the phase i , relative

to the linear displacement x of the rotor [25]:

$$F_{dr,i}(x,t) = -\frac{\partial W_i}{\partial x}, \quad (6.1)$$

where W_i depends on the capacitance $C_i(x)$ between the rotor and the stator phase i , and on the actuation voltage $U_i(t)$ [25]:

$$W_i = -\frac{1}{2}C_i(x)U_i(t)^2. \quad (6.2)$$

Substituting (6.2) in (6.1), we find:

$$F_{dr,i}(x,t) = \frac{1}{2} \frac{\partial C_i(x)}{\partial x} U_i(t)^2. \quad (6.3)$$

We observe from equation (6.2) that:

- The actuation voltage U_i is time dependent (driving signal).
- The capacitance depends on the position x of the rotor, as shown in Figure 6.2.

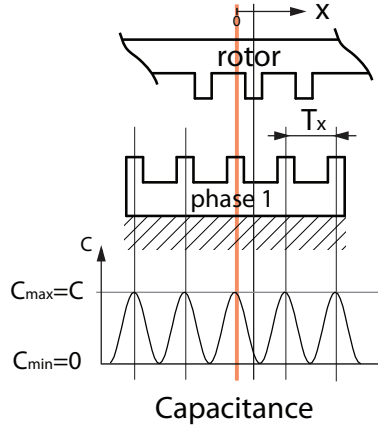


Figure 6.2: Capacitance between the rotor and the stator: the capacitance varies from C_{min} (teeth completely misaligned) to C_{max} (teeth completely aligned). In our model, the variation of capacitance is assumed to be sinusoidal.

The capacitance variations is $C_{max} - C_{min} = C$ and the minimum capacitance $C_{min} = 0$. The approximation of a null capacitance when the teeth are misaligned has no influence on the following calculations, as only the amplitude variations are considered. We will consider a sine approximation in order to keep the model simple; more complex expression of the capacitance are possible, see for example [20].

The expression of the capacitance is:

$$C_i(x) = C \left(\frac{1}{2} + \frac{1}{2} \cos(\omega_x x - \varphi_i) \right) + C_{min}, \quad \varphi_i = \frac{2\pi}{3}(i-1), \quad \omega_x = \frac{2\pi}{T_x}, \quad C_{min} = 0. \quad (6.4)$$

Where φ_i is the geometric phase difference between the phases and T_x is the geometric period of the teeth.

From (6.4), we find the partial derivative $\frac{\partial C_i(x)}{\partial x}$:

$$\frac{\partial C_i(x)}{\partial x} = -\frac{C\omega_x}{2} \sin(\omega_x x - \varphi_i). \quad (6.5)$$

Introducing (6.5) in (6.3), we have:

$$F_{dr,i}(x, t) = -\frac{C\omega_x}{4} \sin(\omega_x x - \varphi_i) U_i(t)^2. \quad (6.6)$$

Using this last expression, we can easily deduce the global driving force F_{dr} : it is the sum of three forces acting on the rotor:

$$\boxed{F_{dr}(x, t) = -\sum_{i=1}^3 \frac{C\omega_x}{4} \sin(\omega_x x - \varphi_i) U_i(t)^2} \quad (6.7)$$

6.1.3 Equation of motion

The equation of motion gives the time dependent position $x(t)$ of the rotor. We use the convention $\dot{x} = \frac{dx}{dt}$, $\ddot{x} = \frac{d^2x}{dt^2}$ to alleviate notation. The expression of the equation of motion is (see Appendix A.7):

$$m\ddot{x} + c\dot{x} + kx = F_{dr}(x, t). \quad (6.8)$$

To write this equation in a more common form, we introduce the undamped natural frequency ω_0 and the damping ratio ζ [16]:

$$\omega_0 = \sqrt{\frac{k}{m}}, \quad \zeta = \frac{c}{2\sqrt{mk}}. \quad (6.9)$$

The driven harmonic oscillator equation can be rewritten [26]:

$$\ddot{x} + 2\zeta\omega_0\dot{x} + \omega_0^2 x = \frac{F_{dr}(x, t)}{m}. \quad (6.10)$$

With the expression of the driving force $F_{dr}(x, t)$ (6.7), the resulting equation of motion is:

$$\boxed{\ddot{x} + 2\zeta\omega_0\dot{x} + \omega_0^2 x = -\sum_{i=1}^3 \frac{C\omega_x}{4m} \sin(\omega_x x - \varphi_i) U_i(t)^2} \quad (6.11)$$

6.1.4 Dynamic model

Equation (6.11) can be completed in order to obtain the model of the micromotor actuated with a three phases sinusoidal signal.

The driving voltage applied on each phase i is defined by:

$$U_i(t) = U_i \sin(\Omega t + \psi_i), \quad \psi_i = \frac{2\pi}{3}(i-1) \quad (6.12)$$

where Ω is the time dependent pulsation of the actuation voltage, and ψ_i the time phase difference of the phase i .

With this excitation voltage, the equation of motion of the micromotor is:

$$\ddot{x} + 2\zeta\omega_0\dot{x} + \omega_0^2x = - \sum_{i=1}^3 \frac{C\omega_x U_i^2}{4m} \sin(\omega_x x - \varphi_i) (\sin(\Omega t + \psi_i))^2 \quad (6.13)$$

6.1.5 Energetic representation

The micromotor can be studied from the point of view of its potential energy. The potential energy representation of the system is well suited to understand the behavior of a system. Indeed, considering the minimum of energy principle, the system will tend to stay in the minimum energy position at equilibrium (it can be represented by a ball in the graph of its potential energy).

This representation is only correct at equilibrium. So the inertia and the damping forces are neglected, and the representation is correct for quasi-static states.

The potential energies involved are the driving force potential W_{dr} , and the spring potential W_k . The global potential energy W is:

$$W = W_{dr} + W_k, \quad (6.14)$$

and the spring potential energy is:

$$W_k = \frac{1}{2}kx^2. \quad (6.15)$$

The driving force potential energy W_{dr} , for phase i , is calculated from equation (6.2), (6.4) and (6.12):

$$W_{dr,i} = -\frac{1}{2}C \left(\frac{1}{2} + \frac{1}{2} \cos(\omega_x x - \varphi_i) + C_{min} \right) (U_i \sin(\Omega t + \psi_i))^2. \quad (6.16)$$

In the case of the potential energy representation, the minimal capacitance C_{min} is supposed to be null. It will only move the whole potential energy up or down depending on the time. It is then not interesting in our representation, and will not be considered in the potential energy graph.

With $C_{min} = 0$, the global potential energy W is:

$$W = \frac{1}{2}kx^2 - \frac{1}{4} \sum_{i=1}^3 C(1 + \cos(\omega_x x - \varphi_i)) (U_i \sin(\Omega t + \psi_i))^2. \quad (6.17)$$

Figure 6.3 shows the potential energy, depending on the position, considering equation (6.17) with $U_1 = U_3 = 0$, $U_2 = U$.

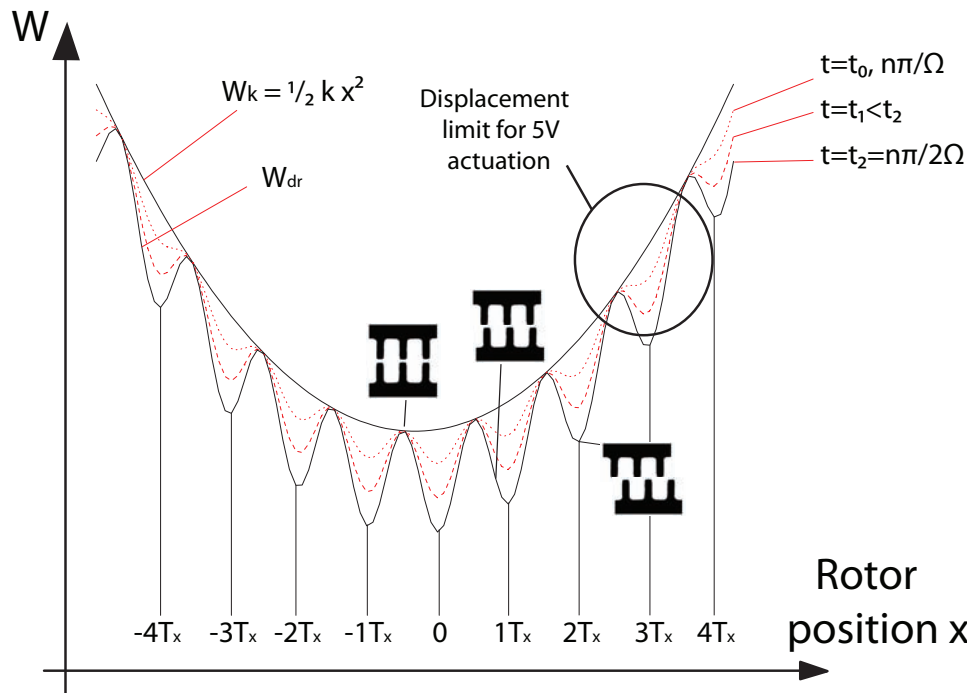


Figure 6.3: Potential energy representation of the stepper micromotor for one phase: the quasi-static potential, equation (6.17), for phase 2 is shown in red. The rotor teeth highlight in black is attracted in the potential well.

This particular case (only phase 2 is represented) is well suited to understand the working principle of the micromotor:

- Considering the minimum energy principle, each teeth of the rotor will stay in the minimum energy position. For this reason, the teeth illustrated in Figure 6.3 will stay in the potential well and moves the rotor to the right.
- By altering the phases actuated, the 3-phase actuation is the successive repetition of this previous step.
- The micromotor will move as long as the potential well is “deep enough”. From eqrefglobal potential2, we observe that the potential wells depend on the applied voltage.

For a given actuation voltage, the spring potential will overcome the actuation digging of the potential at a certain position, and the rotor will not continue its motion. This is visible in Figure 6.3: At $t = t_0$, the potential well is not deep enough and the ball (rotor) rolls back. Then, as expected, the motion range depends on the applied voltage [18] p. 341, equation (8).

6.2 Interpretation of the model using Maple 13

In this section, we will perform simulations of the dynamic response, by setting similar parameters to the experimental measurements performed in Chapter 5, and using the software Maple 13. In §6.2.1, we will establish the equation of motion corresponding to the experimental conditions. In §6.2.2, a variable substitution will be performed in order to enable the simulations using Maple. The simulation results will be exposed in §6.2.3 - §6.2.6. An interpretation of the results will be given in §6.2.7.

6.2.1 Equation of motion

In the experimental measurement, shown in preventive Chapter 5, we have been confronted to three cases depending on the driving voltage:

- §5.1 Case I: a sine voltage with a DC offset on phase 2. Phase 1 and 3 grounded.
- §5.2 Case II: a pure sine voltage on phase 2. Phase 1 and 3 grounded.
- §5.3 Case III: a pure sine voltage on phase 2, a DC voltage on phase 2 and the phase 3 grounded.

In this section, we will perform the calculations details for Cases II and III. (Notice that Case II is a particular case of Case III where $U_1(t) = 0$). Case I will be derived from Case II.

To simulate Case III, we need to define the actuation voltage $U_i(t)$ of the equation of motion (6.11). Referring to §5.3, the driving voltage is:

$$U_1(t) = U_1 = const, \quad U_2(t) = U_2 \sin(\Omega t), \quad U_3(t) = 0. \quad (6.18)$$

The resulting equation of motion corresponding to Case III is:

$$\ddot{x} + 2\zeta\omega_0\dot{x} + \omega_0^2 x + \frac{C\omega_x U_1^2}{4m} \sin(\omega_x x) = -\frac{C\omega_x U_2^2}{4m} \sin(\omega_x x - \frac{2\pi}{3}) \sin(\Omega t)^2 \quad (6.19)$$

6.2.2 Nondimensionalization

Equation (6.19) has several parameters which need to be measured in order to complete the equation:

- The damping ratio ζ is known from the transient response, see Figure 2.17.
- The first resonant pulsation ω_0 is also known from the transient response, see Figure 2.17.
- The capacitance C is highly dependent on the fabrication process.
- The geometric period of the teeth T_x ($\omega_x = 2\pi/T_x$) is known from the design.
- The inertial mass m of the motor can be estimated from the design, but also depends on the process.

U_1, U_2, Ω are chosen parameters.

The parameters C and m are particularly hard to measure. For this reason, we will perform a variable substitution known as “Nondimensionalization”. This method, described in [26], enables a transformation of the equation to another form. We briefly expose it below, and we refer the reader to [26] and Appendix A.8 for more details.

Nondimensionalization:

The idea of the nondimensionalization is to perform a variable substitution, and express a value by a coefficient (a Greek letter) times a characteristic “unit” (denoted with an index c). For example, a mass of $m = 6$ kg can be expressed using:

$$m = \mu m_c,$$

where m is the value to express, $\mu = 6$ is the coefficient, and $m_c = 1$ kg such as the characteristic unit. However, it may be expressed with another characteristic unit, as the ounce [oz]: $m = 211.6$ oz. ($\mu' = 211.6$ is the coefficient and $m'_c = 1$ oz the characteristic unit). Nondimensionalization is a variable substitution to an other unit/yardstick.

(6.19) Rewritten using nondimensionalization with the convention $\frac{d\chi}{d\tau} = \dot{\chi}$, $\frac{d^2\chi}{d\tau^2} = \ddot{\chi}$, becomes:

$$\boxed{\ddot{\chi} + 2\zeta\dot{\chi} + \chi + a\sin(\omega_x x_c \chi) = -\sin(\omega_x x_c \chi - \frac{2\pi}{3})(\sin(\Omega t_c \tau))^2} \quad (6.20)$$

For the calculations details, see Appendix A.8.

The following substitution definition have been performed:

$$t = \tau t_c, \quad x = \chi x_c, \quad (6.21)$$

the characteristic unit t_c and x_c are proper to the system:

$$t_c = \sqrt{\frac{m}{k}} = \frac{1}{\omega_0} [s]; \quad x_c = \frac{C\omega_x U_2^2}{4k} [m], \quad (6.22)$$

and τ, χ are the corresponding coefficient of these values. The amplitude χ is then expressed by multiplying χ by the characteristic unit x_c [m]. The time t is expressed by multiplying τ by the characteristic unit t_c [s].

The coefficient a is defined as the ratio:

$$a = \left(\frac{U_1}{U_2}\right)^2, \quad (6.23)$$

where the parameter a corresponds to the “electrostatic stiffening”, see §5.3 [23].

Nondimensionalization takes all its sense when a closer look is taken at equation (6.20). Indeed, in equation (6.20), the parameters to introduce are:

- ζ , the damping ratio, which is measurable via the step response (Figure 2.17).
- ω_x (or T_x) is a known geometrical parameter.
- $x_c = \frac{C\omega_x U_2^2}{4k} = \frac{\hat{F}_{dr2}}{k}$ is the driving force amplitude \hat{F}_{dr2} , divided by the stiffness k . In other words, it is the maximum amplitude displacement at low frequencies (at DC actuation). It is easily measurable in Figure 5.4.
- $t_c = \sqrt{\frac{m}{k}} = \frac{1}{\omega_0}$, the resonant frequency of the rotor is easily measurable.

All these parameters are easily measurable with good accuracy. We notice that Ω is the pulsation of the driving frequency which can be chosen to simulate the corresponding oscillation frequency.

6.2.3 Numerical application

In our model, we have used the following parameters:

- From Figure 2.19 and Figure 5.4, $\omega_0 = 2\pi 163$ $t_c = \frac{1}{2\pi 163}$ s .
- From Figure 5.5, $x_c = 0.2 \cdot 10^{-6}$ m .
- From Appendix A.1, $\omega_x = \frac{2\pi}{T_x} = \frac{2\pi}{10.838 \cdot 10^{-6}}$ m⁻¹.
- From Figure 2.17, the exponential decrease of the transient response λ is $\lambda = 22$ s⁻¹. With:

$$\lambda = \zeta\omega_0; \quad \zeta = \frac{\lambda}{\omega_0} = \frac{22}{2\pi 163} = 0.0215,$$

(6.20) becomes:

$$\ddot{\chi} + 0.043\dot{\chi} + \chi + a \sin\left(\frac{0.2 \cdot 2\pi}{10.838}\chi\right) = \sin\left(\frac{0.2 \cdot 2\pi}{10.838}\chi - \frac{2\pi}{3}\right) \left(\sin\left(\Omega \frac{1}{2\pi 163}\tau\right)\right)^2 \quad (6.24)$$

6.2.4 Case II: Nonlinearity simulation

The driving voltage corresponding to Case II, see §5.2, is:

$$U_1(t) = U_1 = 0, \quad U_2(t) = U_2 \sin(\Omega t), \quad U_3(t) = 0. \quad (6.25)$$

Phase 1 is grounded. $U_1 = 0$ hence $a = 0$. Equation (6.24) can be rewritten:

$$\ddot{\chi} + 0.043\dot{\chi} + \chi = \sin\left(\frac{0.2 \cdot 2\pi}{10.838}\chi - \frac{2\pi}{3}\right) \left(\sin\left(\Omega \frac{1}{2\pi 163}\tau\right)\right)^2 \quad (6.26)$$

To perform the simulations, we define the time pulsation of the sine actuation voltage Ω as a linear sine chirp, since it was used in the experimental results:

$$\Omega(t) = 2\pi \left(f_{start} + \frac{f_{end} - f_{start}}{t_{sweep}} \tau \right), \quad (6.27)$$

with f_{start} the initial frequency, f_{end} the ending frequency, and t_{sweep} the chirp time. We calculate the amplitude response of the system for a sine actuation voltage chirp from $f_{start} = 1\text{Hz}$ to $f_{end} = 200\text{ Hz}$ in a time $t_{sweep} = 10\text{ s}$. The calculation results do not differ for a chirp time of 10 seconds or 5 minutes.

Equation (6.26), with the pulsation definition described above, has been calculated using Maple 13 and the code exposed in Appendix A.9.

To respect the convention set in Chapter 5, we show in Figure 6.4 the amplitude response of the system depending on the excitation frequency $f_{exc} = 2f_{dr} = 2 \cdot \frac{\Omega}{2\pi}$. The amplitude is expressed by χ . With the relation $x = \chi x_c$, the amplitude in Figure 6.4 is relative to $x_c = 0.2\mu\text{m}$.

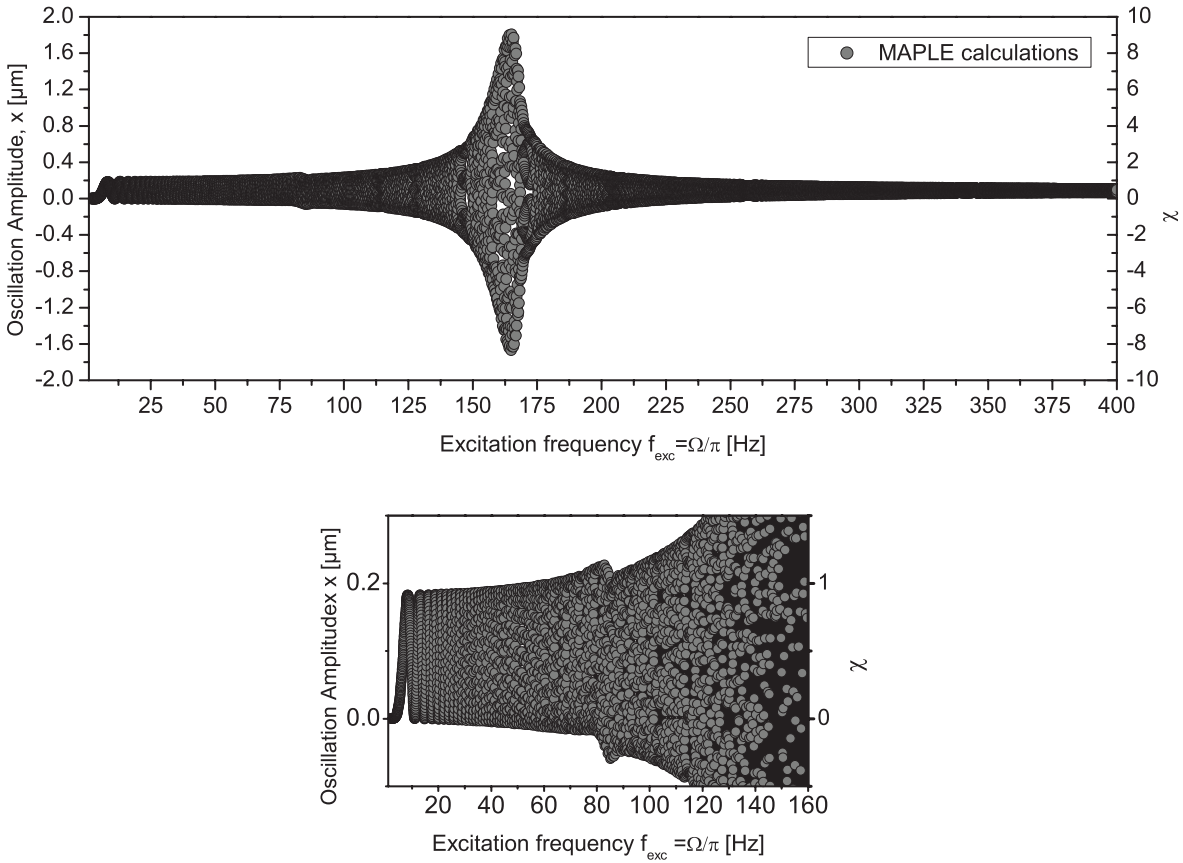


Figure 6.4: Maple simulation results of a linear sine chirp with a driving voltage corresponding to Case II: $x = \chi x_c, x_c = 0.2\mu\text{m}$. To be compared with the experimental results of Figure 5.5.

We notice that the second nonlinear peak, occurring at $\approx 326\text{ Hz}$ in our experiments, is not observed in the simulations.

6.2.5 Case III: Simulation of the electrostatic stiffening effect

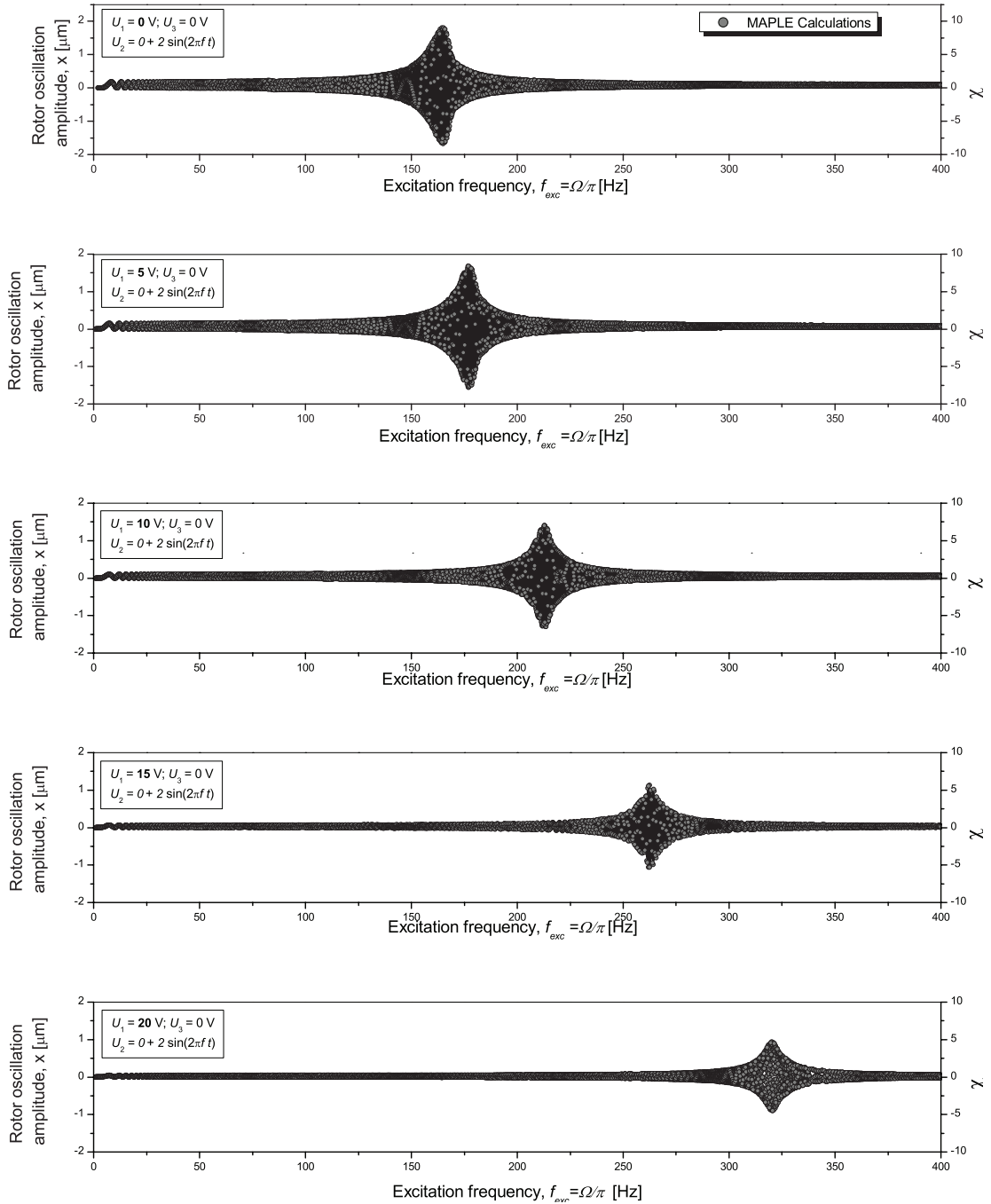


Figure 6.5: Maple simulation results of a linear sine chirp excitation. The driving voltage corresponds to the case III in §5.3.

The driving voltage corresponding to Case III, see §5.2, is:

$$U_1(t) = U_1 = \text{const} \neq 0, \quad a = \left(\frac{U_1}{U_2}\right)^2 \neq 0 \quad U_2(t) = U_2 \sin(\Omega t), \quad U_3(t) = 0. \quad (6.28)$$

Hence equation (6.24) can be rewritten:

$$\ddot{\chi} + 0.043\dot{\chi} + \chi + a \sin\left(\frac{0.2 \cdot 2\pi}{10.838}\chi\right) = \sin\left(\frac{0.2 \cdot 2\pi}{10.838}\chi - \frac{2\pi}{3}\right) \left(\sin\left(\Omega \frac{1}{2\pi 163}\tau\right)\right)^2, \quad (6.29)$$

where a is a variable set depending on U_1 and U_2 (6.23).

Figure 6.5 shows the simulations results of a sine chirp from an excitation frequency $f_{start} = 1$ Hz to $f_{end} = 400$ Hz in a time $t_{sweep} = 10$ s. The calculations do not differ for a chirp time of 10 seconds or 5 minutes.

6.2.6 Case I: Driving voltage simulation results

The actuation voltage (equation(6.18)) can be change in order to correspond to Case III in §5.1:

$$U_1(t) = U_1 = 0. \quad \text{so } a = 0, \quad U_2(t) = U_2\left(\frac{1}{2} + \frac{1}{2}\sin(\Omega t)\right), \quad U_3(t) = 0. \quad (6.30)$$

With the same calculations performed in §6.2, §6.2.2 and §6.2.3, we find:

$$\ddot{\chi} + 0.043\dot{\chi} + \chi = \sin\left(\frac{0.2 \cdot 2\pi}{10.838}\chi - \frac{2\pi}{3}\right) \left(\frac{1}{2} + \frac{1}{2}\sin\left(\Omega \frac{1}{2\pi 163}\tau\right)\right)^2 \quad (6.31)$$

Figure 6.6 shows the simulations results of a sine chirp from an excitation frequency $f_{start} = 1$ Hz to $f_{end} = 400$ Hz in a time $t_{sweep} = 10$ s. The calculations do not differ for a chirp time of 10 seconds or 5 minutes.

Exactly as in the case I (§5.1), $f_{exc,1} = \Omega/2\pi$ and $f_{exc,2} = 2\Omega/2\pi$. The amplitude χ in Figure 6.6 is relative to $x_c = 2\mu m$.

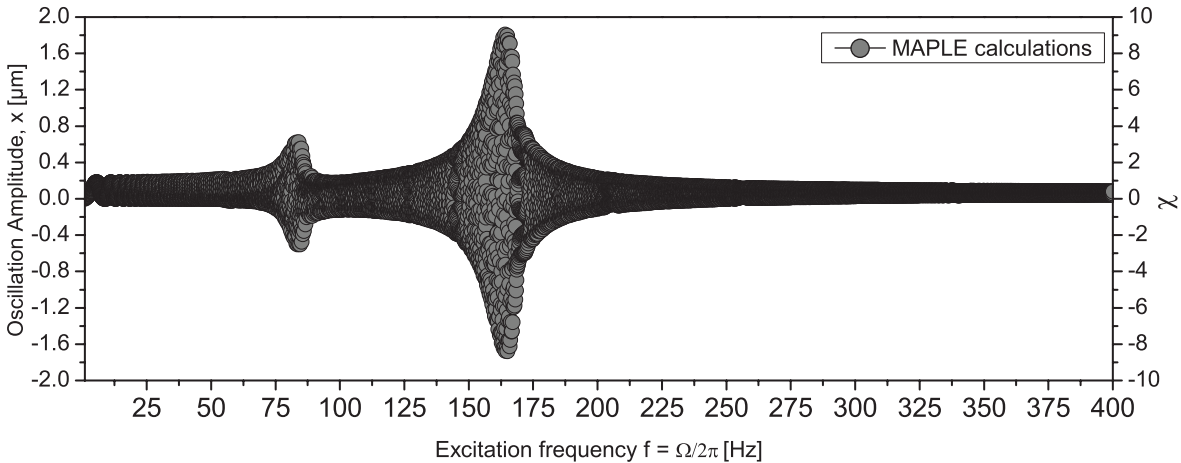


Figure 6.6: Maple simulation results of a linear sine chirp excitation with a driving voltage corresponding to the case I. $f_{exc,1} = \Omega/2\pi$, $f_{exc,2} = 2\Omega/2\pi$.

Figure 6.6 shows that the simulations are in good agreement with the experimental results of Figure 5.5 (top).

6.2.7 Interpretation of the results

The dynamic behavior of the micromotor in Case II and III can be discussed and understood through the potential energy representation (Case I is already understood, see §5.1, as it depends only on the actuation voltage).

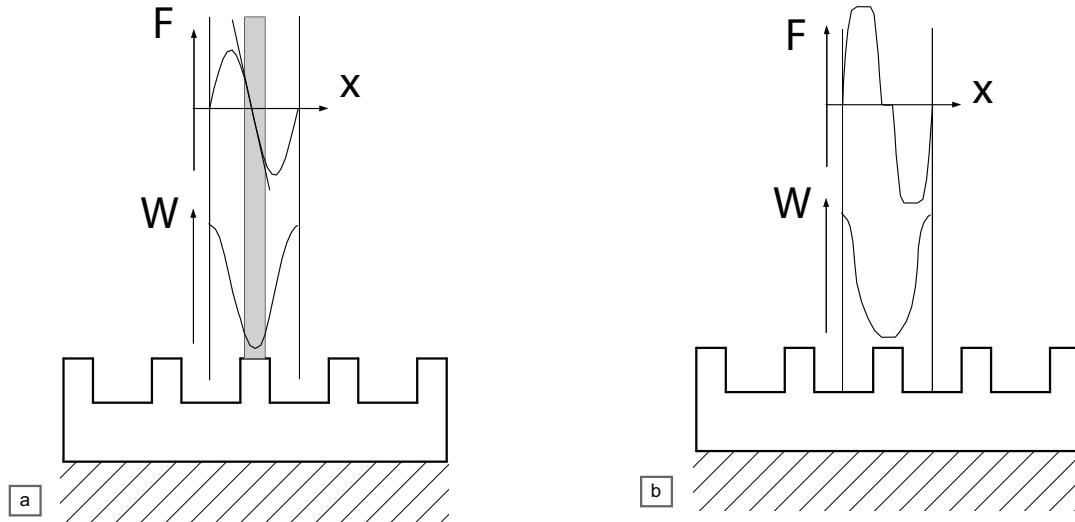


Figure 6.7: Potential energy representation of the stepper micromotor for one tooth: (a) sine approximation of the potential W and the resulting force F ; (b) Pseudo sine potential W and the resulting force F .

In Figure 6.7 (a), we show the potential energy W and the force F corresponding to a single tooth. With the approximation of a sine potential, the force for small displacement is linear (grey area in Figure 6.7). Indeed, the Taylor series of a sine function is:

$$\sin(x) = x + \frac{x^3}{3!} + \dots \quad (6.32)$$

However, if the oscillations exceed small displacement, the larger force is not linear and the system becomes nonlinear.

Figure 6.7 (b) highlights the importance of the potential shape. Indeed, for another potential shape, the reasoning fundamentals (described above) are correct, but the resulting force is modified. Figure 6.7 (b) is an example of an other potential voluntarily chosen excessively different. The force F is no more linear, and the behavior of the system differs significantly.

The experimental results compared to the simulations highlight a good validity of the sine approximation. However, a more precise capacitance expression will increase the model value and the accuracy of the simulations (see [20]).

Notice also that the damping and inertial effects are not considered in this representation.

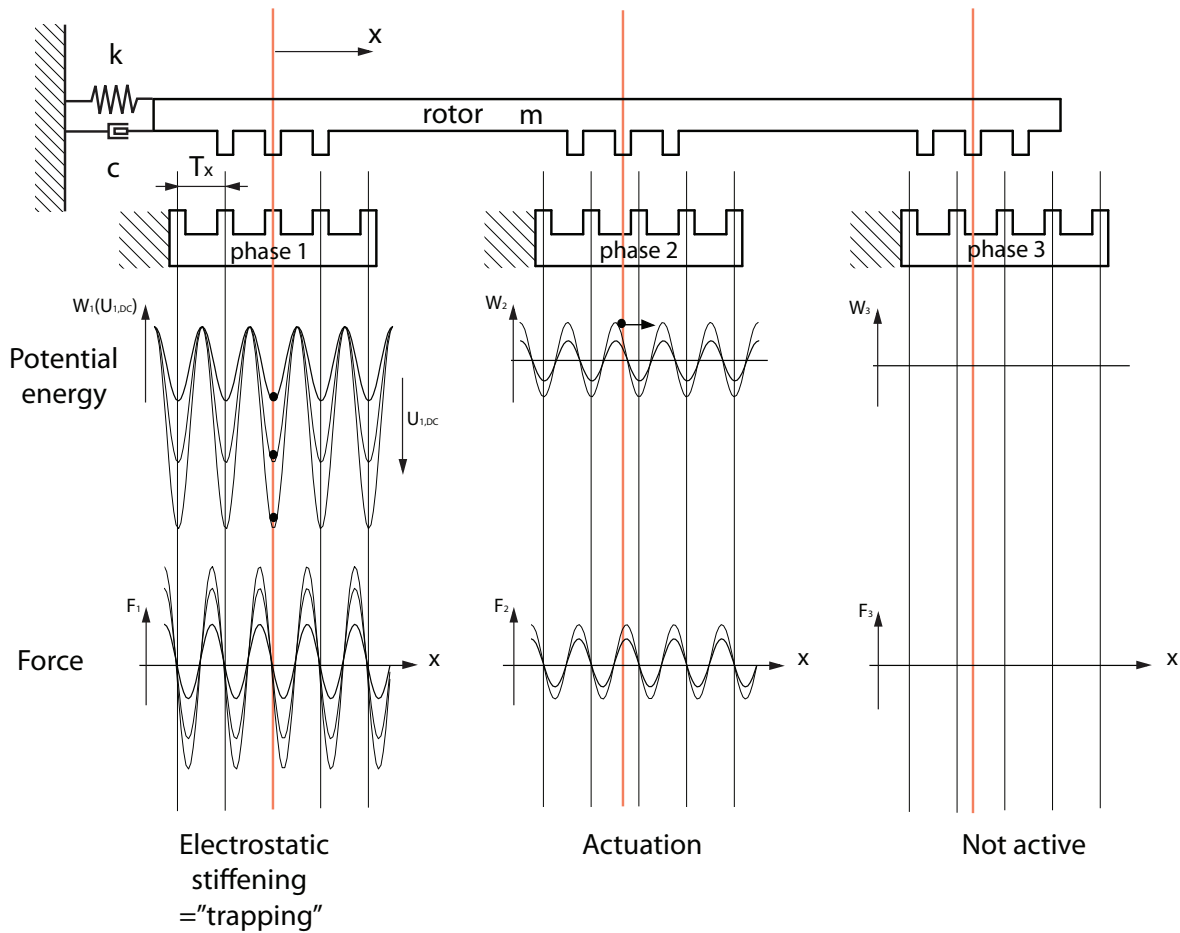


Figure 6.8: Potential energy representation of the stepper micromotor stiffening effect: The phase 1 potential well $W_1(U_{1,DC})$ is dug by the DC voltage $U_{1,DC}$ and the phase one rotor teeth are trapped in the potential. The actuation is performed on phase 2.

Figure 6.8 illustrates the stiffening effect. The Phase one potential $W_1(U_{1,DC})$ traps the rotor depending on the DC voltage $U_{1,DC}$. It results in an apparent stiffening of the rotor.

6.3 Modeling conclusion

This chapter, joined with the experimental results, forms a good understanding of the micromotor studied. The experimental results concord with the model, which can be represented by its potential energy, and intuitively understood. Each case presented in Chapter 5 has its respective correct model.

Chapter 7

Design and fabrication of a micromotor with a differential capacitive sensor

In this chapter, we expose the design improvements and the fabrication results of the prototypes. This chapter is kept succinct voluntary as it is only an overview of the work performed in the CMi cleanroom. The details of the design and the fabrication process data are included in the CD-ROM¹ of the Master Project. We will only summarize the important main points:

- In Section 7.2, we will explain the design modifications and expose the improved versions of the micromotor.
- In Section 7.4, after a presentation of several potential applications, we will expose the design of a microrobotic demonstrator.
- Section 7.3 will finally provide a brief summary of the fabrication results.

Although this chapter is brief, it is not representative of the amount of time invested in the fabrications of the micromotors and in the optimization of the fabrication process.

¹The CD-ROM will be available after the Master Project's oral defense.

7.1 Versions of the micromotors

We present here the work performed in the cleanroom. Several iterations of the designs have been necessary and they are presented here for convenience. We will explain in more details their designs in the following sections.

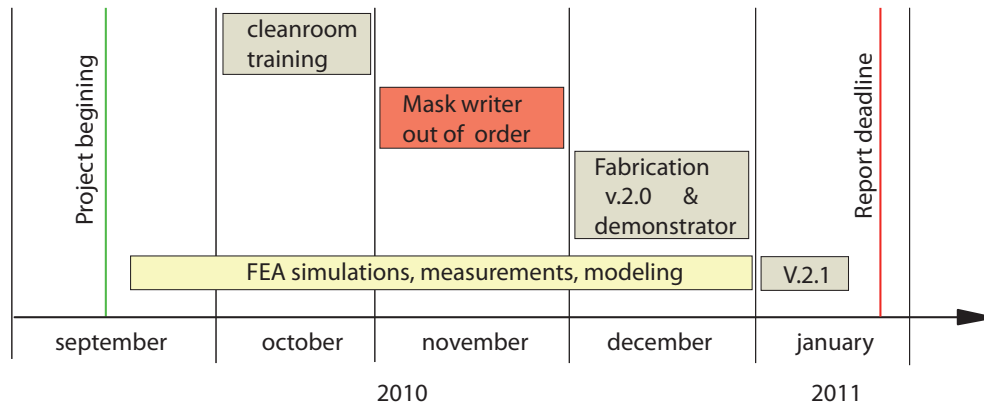


Figure 7.1: Gantt diagram of the Master Project.

7.1.1 Micromotor v.1

The micromotor v.1 is the “single-mask” process version of the previously “two-mask” process micromotors described in §2.2.2, [21]. The mobile elements have been perforated (mesh-like structure) in order to allow the release of the structure by HF vapor etching of SiO_2 sacrificial layer, see Appendix A.15. The design is illustrated in Figure A.8.

7.1.2 Micromotor v.2.0

The micromotors v.2.0 and v.2.1 have three main improvements in their designs: (i) the implementation of a differential capacitive sensor, see §7.2.1; (ii) an increase of the electrostatic torque, see §7.2.2; and (iii) the integration of AFM-like probes sensor for force measurement, see §7.2.3. The micromotors v2.0 and 2.1 have been realized with a needle hand or with a AFM-like probe sensor, see Appedix A.11 and A.12.

7.1.3 Micromotor v.2.1

The micromotor v.2.1 is similar to the v.2.0 but some modifications have been performed in order to increase the fabrication process yield to the HF etching. The anchored parts (*e.g.* the stator phases) are larger and more robust to the etching rate variations that caused a limited yield of the v.2.0 after vapor HF etching.

7.2 Design modifications

7.2.1 Capacitive measurement of the angular position

In order to measure the position, we have implemented an angular differential capacitive sensor, see Figure A.11. The capacitance varies theoretically between 120 [fF] and 580 [fF].

Sensor mechanical design - In Figure 7.2, we have simulated the deformation of the rotor due to the radial electrostatic force in the capacitive sensor region. The radial electrostatic force $F(x)$ is expressed by:

$$F(x) = -\frac{\partial W}{\partial g},$$

where W is the electrostatic potential of phase 1, g the rotor/stator gap.

$$W = -\frac{1}{2}C(g)U^2,$$

where $C(g)$ is the capacitance between the rotor and the stator phase 1 depending on the gap g and the voltage U applied.

$$C(x) = \epsilon_0 \epsilon_r \frac{A}{g},$$

where ϵ_0 , the vacuum permittivity, ϵ_r the relative permittivity of air and A the capacitance surface. Then:

$$F(x) = \epsilon_0 \epsilon_r \frac{AU^2}{2g^2}. \quad (7.1)$$

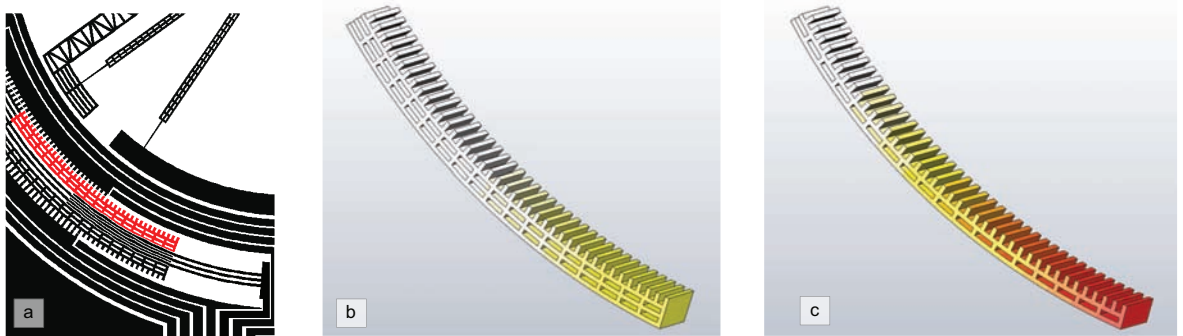


Figure 7.2: Rotor buckling simulation in the capacitance sensor region: the simulations has been performed using the miromotor parameters listed in Appendix A.2 with the equation (7.1). (a) Mechanical structure tested (b) Rotor with simple meshed structure (c) Rotor with double meshed structure

Figure 7.2 illustrates the deformation simulation of the rotor structure in the capacitive sensor (see Figure A.11) depending on the rotor type. The simulations highlight a buckling of the rotor with simple meshed structures and a low deformation of the double meshed structure. The second design has been kept for the micromotor.

7.2.2 Design modification studies in order to increase the torque

The two-mask micromotor has limited actuation torque. For this reason, version 2 has been improved in order to reach a higher torque. This micromotor is illustrated in Appendix A.12 and is composed of the same butterfly pivot, as in the previous design. However, the stator is composed of an internal stator ring. The rotor is composed of a double-sided ring with teeth distributed on its internal and external radius.

Using equations (2.5), (2.6), (2.3) and (2.1) with the micromotors dimensions given in Appendix A.10.1, we calculate the butterfly pivot stiffness $K_{\otimes,r} = 7.74 \cdot 10^{-8}$ Nm/rad and its maximum angle of rotation $\theta_{\otimes,r,adm} = 46.0^\circ$ before plastic deformation. They are similar for all the micromotors.

For each version of the micromotor, we calculate the electrostatic torque M_{el} applied by the stator on the rotor. The results are summarized in Table 7.1.

Electrostatic torque	version 1	version 2.0	version 2.1
M_{el}	$4.6 \cdot 10^{-8} Nm$	$10.2 \cdot 10^{-8} Nm$	$11.5 \cdot 10^{-8} Nm$

Table 7.1: Micromotors electrostatic torque M_{el} for the different version of the micromotor.

We note that micromotors v. 2.0 and v.2.1 have a torque corresponding approximatively to twice that obtained in v.1. For this reason, the micromotor version 2 should reach a $30^\circ (\pm 15^\circ)$ rotational range at lower voltage compared to version 1. This is an interesting point considering the electrostatic sticking effect.

Comparison of the micromotors

In quasi-static state, the actuator torque M_{motor} depending on the angle θ and on the reinforced butterfly pivot stiffness $K_{\otimes,r}$ of the micromotor can be calculated using the following equation:

$$M_{motor}(\theta) = M_{el} - \theta K_{\otimes,r}$$

F_{hand} , corresponding to the force developed by a micromotor hand at a distance $d = 1$ mm from the micromotor center can be calculated with:

$$F_{hand}(\theta) = \frac{M_{el} - \theta K_{\otimes,r}}{d}$$

These calculations must be considered as an approximation since the orthotropic properties of silicon are not considered, (see §3.1.3).

In Figure 7.3 are compared the two micromotors properties. It is obvious that the micromotor's second version is much more powerful.

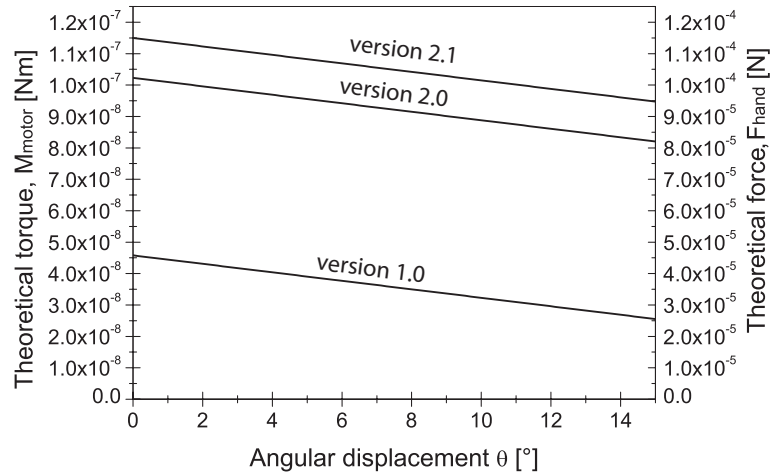


Figure 7.3: Comparison of the micromotor versions. The theoretical torque $M_{motor}(\theta)$ of the micromotor and the force at the extremity of a hand of length $d = 1\text{mm}$ from the micromotor center is reported depending on the angular displacement.

7.2.3 AFM-like torque measurement

In order to quantify the micromotor torque, we implemented AFM-like probes in the micromotors second version, see Appendix A.12. The sensor is simply composed of a beam, deflected by the micromotor motion and measured by microscopy. The force can be deduced by the material strength theory (see [6] and [9]).

Figure 7.4 illustrates the sensor working principle. The motor torque can be deduced at the equilibrium between the motor torque and the beam reaction force.

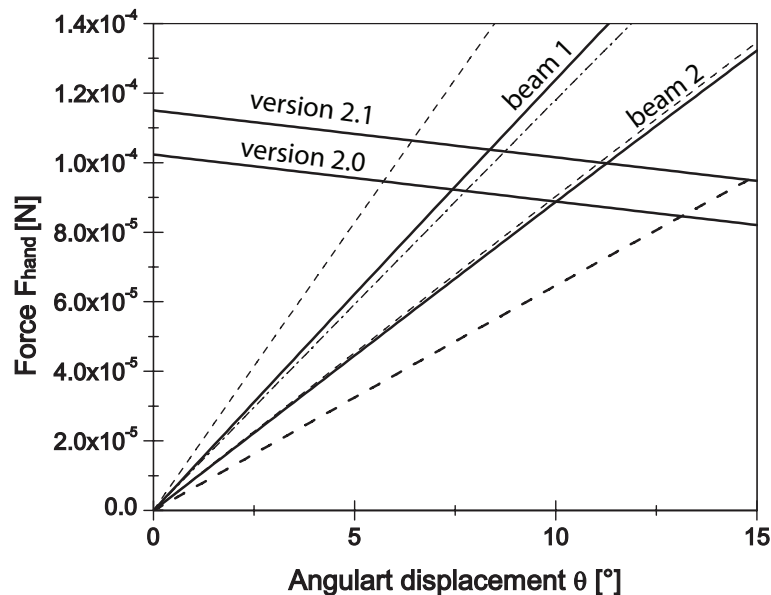


Figure 7.4: Force sensor: Two silicon beams are bended depending on the micromotor rotation. The beam stiffness depends on the fabrication process. The graph exposes the two beams stiffness with their respective incertitude of fabrication. The micromotor torques depending on the version are reported.

The beam sensor dimensions, *i.e.* the width b , must be measured after fabrication in order to perform a precise measurement.

7.3 Potential applications and design of a demonstrator

In this section, we briefly present some possible applications in different fields of MEMS. From these applications, we will design and fabricate a demonstrator, see §7.3.4.

7.3.1 Optical MEMS

As stated by X. M. Zhang *et al.* [30], variable optical attenuators can be realized by tuning the position of micromirrors retro-reflectors position. The design presented in Figure 7.5 does not need a large rotation angle. However, the $\pm 15^\circ$ rotational angle of our micromotor could open paths for new designs in MOEMS (Micro Opto Electro Mechanical Systems). An example of application is an optical switches, illustrated Figure 7.6. The large rotational angle is used to move a mirror which reflects an optical signal from an optical fiber to another one.

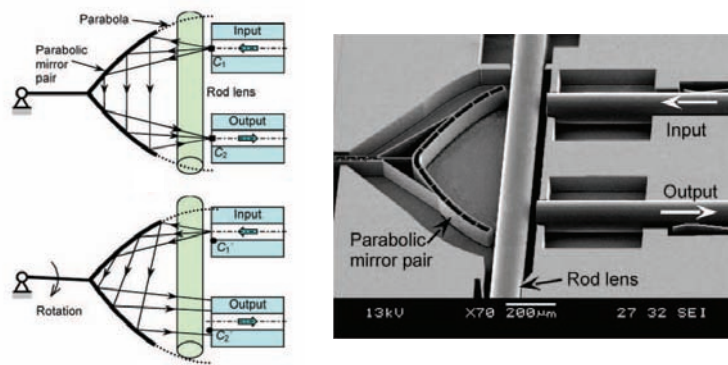


Figure 7.5: Example of application: Retro-axial attenuator. (top) Initial state; (bottom) increasing the attenuation level by rotating the mirror pair (right) SEM picture of the device realized. Figure reproduced from [30]

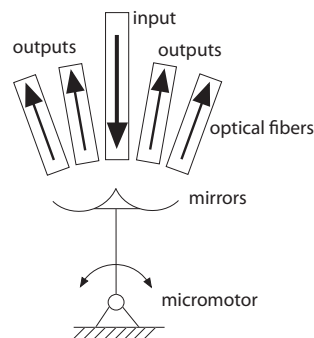


Figure 7.6: Example of a potential application: Optical switch using micromirrors guided by the $\pm 15^\circ$ rotational angle of a micromotor.

This application has not been realized as the optic applications are not in the research domains of the Laboratory of Microsystems LMIS2.

7.3.2 Vertical stage for a profilometer

The micromotor could be implemented as a pseudo vertical stage in profilometers, as illustrated in Figure 7.7. Indeed, a precise positioning of a microrobotic arm with a large motion range could be advantageously used in profilometers. This design, proposed by E. Sarajlic, has not been considered as its assembly is complex in the frame of a Master Project.

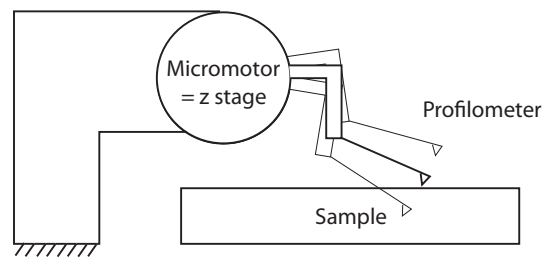


Figure 7.7: Micromotor application in the vertical stage of a profilometer

7.3.3 Monolithic planar 3-DOF parallel micromanipulator

Inspired from the Ph. D. Thesis of B. R. de Jong [7], we have studied the implementation of the micromotor in 3 DOF micromanipulators, as illustrated in Figure 7.8. The large rotation angle of the micromotor is well suited in such an application (for further details, refer to [12] and [27]). After discussing with R. Clavel, Professor in Robotics at EPFL (LSRO), we chose not to consider this application, since the complete model of the structure deformation is complex in the case of monolithic structure. Furthermore, the simultaneous driving of the 3 micromotors would have been complicated and not realizable in the given time for the Master Project.

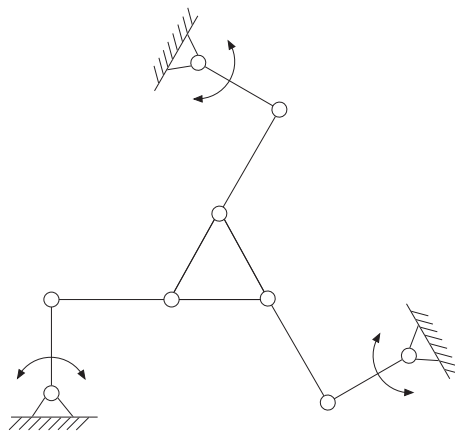


Figure 7.8: 3 DOF micromanipulator.

7.3.4 Microgripper: Design of a demonstrator

Inspired from the microgripper of F. Beyler ([4] and [3]), a microgripper has been designed in order to expose the performance of the micromotor, see Appendix A.13. The microgripper structure is composed of a parallelogram with two active micromotors in its anchoring points and two butterfly pivots in the mobile element. This mobile element performs a circular translation depending on the length l of the links, see Figure 7.9.

After discussion with R.Clavel, this design has been chosen for its simplicity. The device is a 1 DOF gripper with two micromotors driven by a identical signal. Compared to the 3 DOF parallel micromanipulator, the structure has only four pivots, two of which are micromotors. The number of active joints compared to the passive ones is higher and the motion range bigger. In addition, the deformation of the parallelogram is easily predictable.

The microgripper demonstrators have been realized in two versions: one with capacitive sensors and a second one without capacitive sensor, see Appendix A.15.

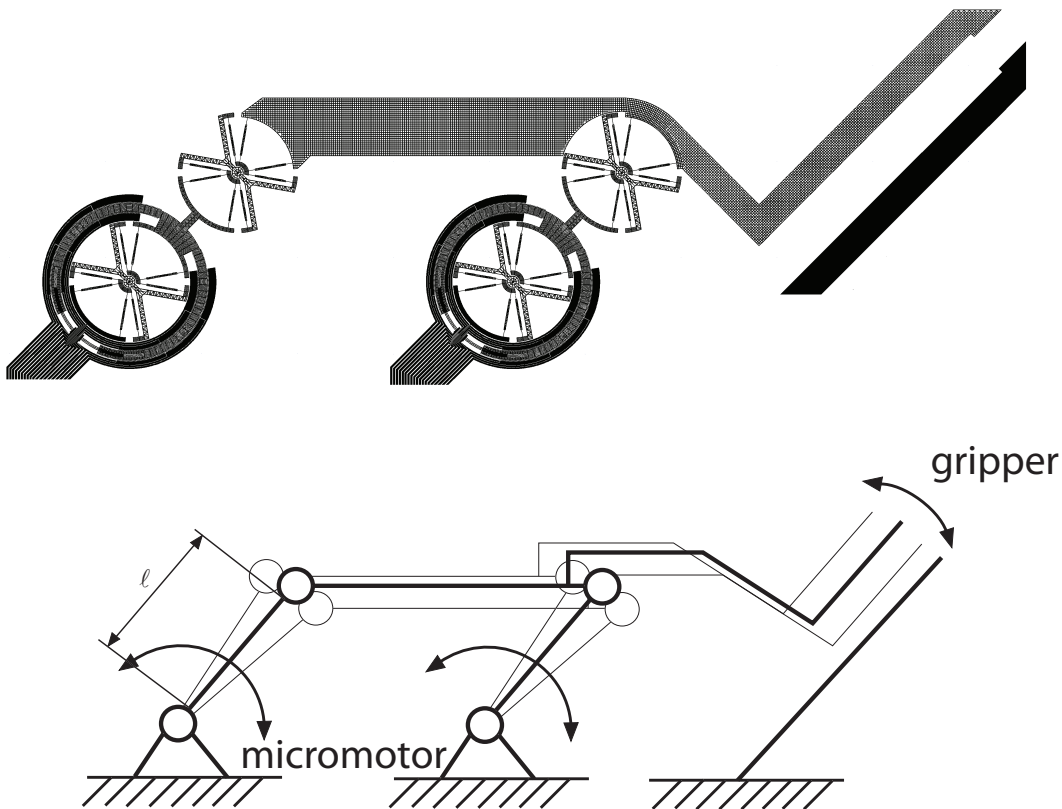


Figure 7.9: Microgripper design: (a) Design realized, a parallelogram structure with two active micromotors in its anchoring points and two butterfly pivots in the mobile element. (b) The mobile element performs a circular translation depending on the length l of the links.

7.4 Fabrication results

7.4.1 Micromotor v.1

These micromotors have been realized on a wafer with a $4\mu\text{m}$ oxide thickness (SOI 380-4-50 wafer). The results highlight a very poor quality of the oxide layer: the $4\mu\text{m}$ oxide thickness etched by HF presents porous zones due to HF infiltrations, see Figure A.10. It results in a delamination of the micromotor, see Figure A.9, which is completely out of order.

After discussing with the CMi cleanroom staff, we figure out that the supplier of SOI wafer has changed. This type of SOI wafer oxide is frequently porous after HF etching. We consequently chose not to consider this solution anymore.

Then, we considered the problem from another point of view. The electrostatic sticking is due to the capacitance between the two layers. It depends on the difference of voltage between the rotor and the bulk. We chose to perform a better grounding of the bulk, as illustrated in Figure 7.10.

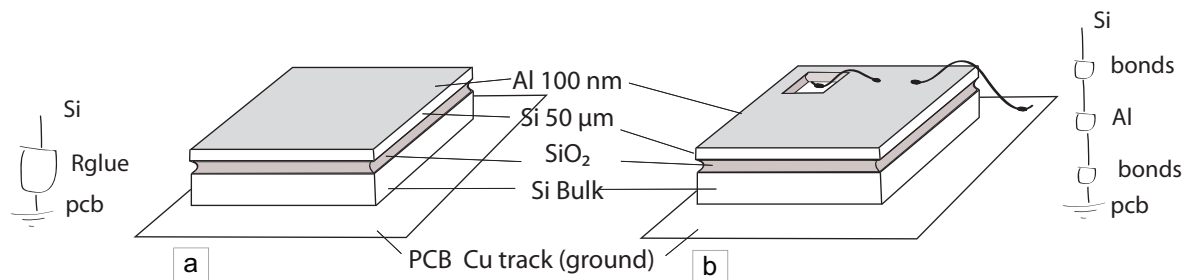


Figure 7.10: Grounding of the silicon bulk: (a) Grounding of the silicon bulk to the PCB grounded track via a conductive glue; (b) Grounding of the silicon bulk to the PCB grounded track via bonds: silicon bulk - silicon working layer - PCB grounded track.

After measurement, we observed that the glue used to contact the chip was resistive (even with the most conductive glue) and the bulk was not properly grounded. The bypass of the glue via the bonds avoids this problem and the bulk is then correctly grounded.

This simple modification performed on single-mask micromotors has increased the threshold voltage level from 30 V to 75 V and opened the path to single-mask processes. Version 2.0 and 2.1 have been grounded using this principle.

7.4.2 Micromotor v.2.0

As illustrated in Figure A.18, the realization of micromotors version 2.0 on $2\mu\text{m}$ oxide thickness (SOI 380-4-50) wafers have been stopped by HF etching problems. The etching rate, which is of $2\mu\text{m}/\text{hour}$ in normal conditions, was abnormally unstable. All the micromotors realized have been over etched as the etch rate was in the range of $60\mu\text{m}/\text{hour}$.

7.4.3 Microrobot fabrication results

The microrobots have been realized with in the same period of time as the micromotor version 2.0. However, the etching rate has been carefully measured during the process. The designs fabricated were not functional as the oxide under the capacitive comb sensors has not been etched, see Figure A.15. We can conclude that the $1\ \mu\text{m}$ gap between the capacitance comb is not a sufficiently large access for the vapor HF. This has been taken into account in the version 2.1 of the design, see Figure A.20. In addition, test structures have been added on the micromotor chip to quantify more easily the HF etching rate.

7.4.4 Micromotor v.2.1

The micromotor version 2.1 have been successfully fabricated. However, the under-etching occurring during the whole process was much lower than expected. For this reason, the beam widths of the butterfly pivot are larger than expected. The resulting reinforced butterfly pivot has a much higher stiffness, since $K_{\otimes,r} \propto b^3$.

The motion of the micromotor is then much lower than expected (about $\pm 3^\circ$) but this version of the micromotor does not suffer from electrostatic sticking and this limitation has been solved. Concerning the limited performances of this design, the adaptation of the mask to the process should be considered in the next design.

7.4.5 Discussion of the fabrication results

The main conclusions of the fabrication results, for further reliable fabrication process are:

- The use of $4\ \mu\text{m}$ oxide layer wafers is not appropriate, since the HF etching step is not reliable.
- The $2\ \mu\text{m}$ oxide layer wafers could be used for the fabrication but with a particular care of the etching rate (test structures recommended).
- The critical dimension for HF etching access is of $5\ \mu\text{m}$.
- The bulk must be grounded by a wire bonding via the top Si layer.

With this considerations, we are confident that the success of the fabrication of the proposed prototypes is in a close future.

Chapter 8

Conclusion and Outlook

We have performed a thorough experimental modal analysis of a 3-phase electrostatic stepper micromotor. Through the comparison of the experimental results obtained from different optical characterization methods, we have analyzed the dynamic behavior of the system. In parallel, using SolidWorks Simulation software, we have computed static and dynamic FEA simulations of its mechanical properties. Furthermore, we have established a complete mathematical model and verified its validity through numerical calculations with Maple. The whole study is consistent and provides a global understanding of the micromotor's properties.

We have also brought several modifications to the design of the rotary stepper micromotor. The most notable improvements are the increase of the electrostatic torque and the inclusion of a differential capacitive angular sensor. The implementation of this micromotor in a microgripper has been studied and designed. Throughout this project, we have realized the different prototypes in the EPFL cleanroom and validated our single-mask fabrication process.

We are confident that the success of the fabrication of the proposed prototypes will be reached a close future. It should then be possible to demonstrate angular sensing with the differential capacitance and to quantify the micromotor's torque with AFM-like probes. Finally, further analysis of the nonlinearity of the micromotor could be carried out to enhance the mathematical model.

The intermediate results of this Master Project have led to a publication in *Proc. 24th IEEE Int. Conf. on Micro Electro Mechanical Systems (MEMS)*: M. Stranczl *et al.*, "Modal Analysis and Modeling of a Frictionless Electrostatic Rotary Stepper Micromotor", pp. 1257-1260, Cancún, Mexico, January 23-27, 2011.

As I write these lines, the Laboratory of Microsystems has offered to hire me for 6 months in order to finalize this research. It is with great interest that I will pursue this project as a Scientific Assistant.

Acknowledgment

I gratefully acknowledge the valuable discussions and encouragements from Dr. Edin Sarajlic and Prof. Remco Wiegerink (MESA+ Research Institute, The Netherlands) for helping with the experimental characterization of the motor and the capacitance sensor design.

Particular thanks to the CMi staff for their technical support in the cleanroom and to the ACI staff for the PCB design and the wire bonding of the chips. Sincere gratitude to Prof. Max-Olivier Hongler for his valuable advices concerning the nonlinear systems and to Prof. Raymond Clavel for his advices concerning the design of the microgripper. This Master thesis would not have been possible without the valuable help from my assistant, Dr. Christophe Yamahata, whom I specially thank for his support. I am also grateful to his colleague Damien Joss for his support and advices in the cleanroom. I would like to thank Prof. Martin Gijs, for this project that I have been pursuing for one year.

I am also grateful to Shirin and Shahin Tavakoli for their support, as well as all my family, in particular my parents.

Bibliography

- [1] Design of flexure hinges. <http://www.tribology-abc.com/abc/flexure.htm>, consulted on November 23, 2010.
- [2] A. Al Kharfane. Fabrication et caractérisation de micropincette en SOI, Autumn 2010. EPFL Semester Project.
- [3] F. Beyeler, D. J. Bell, B. J. Nelson, Y. Sun, A. Neild, S. Oberti, and J. Dual. Design of a micro-gripper and an ultrasonic manipulator for handling micron sized objects. In *Proceedings of the IEEE/RSJ International Conference on Intelligent Robots and Systems (IROS)*, pages 772–777, October 9-15, 2006.
- [4] F. Beyeler, A. Neild, S. Oberti, D. J. Bell, Y. Sun, J. Dual, and B. J. Nelson. Monolithically fabricated microgripper with integrated force sensor for manipulating microobjects and biological cells aligned in an ultrasonic field. *Journal of Microelectromechanical Systems*, 16(1):7–15, 2007.
- [5] A. Bosseboeuf and S. Petitgrand. Characterization of the static and dynamic behaviour of M(O)EMs by optical techniques: Status and trends. *Journal of Micromechanics and Microengineering*, 13(4):S23–S33, 2003.
- [6] J. Botsis. *Introduction à la mécanique des solides et des structures*. Presses Polytechniques et Universitaires Romandes, Lausanne, Switzerland, 2004.
- [7] B. R. de Jong, D. M. Brouwer, M. J. de Boer, H. V. Jansen, H. M. J. R. Soemers, and G. J. M. Krijnen. Design and fabrication of a planar three-DOFs MEMS-based manipulator. *Journal of Microelectromechanical Systems*, 19(5):1116–1130, 2010.
- [8] Polytec GmbH. Polytec tutorial: 3-D vibration and motion analysis of microstructures. <http://www.polytec.com/us/company/technologies/>, consulted on January 19, 2011.
- [9] S. Henein. *Conception des guidages flexibles*. PhD thesis, École Polytechnique Fédérale de Lausanne (EPFL), Lausanne, Switzerland, 2004.
- [10] S. Henein, P. Spanoudakis, S. Droz, L. I. Myklebust, and E. Onillon. Flexure pivot for aerospace mechanisms. In *Proceedings of the 10th European Space Mechanisms and Tribology Symposium, European Space Agency (Special Publication, ESA SP)*, number 524, pages 285–288, San Sebastian, Spain, September 24-26, 2003.

-
- [11] M. A. Hopcroft, W. D. Nix, and T. W. Kenny. What is the Young's modulus of silicon? *Journal of Microelectromechanical Systems*, 19(2):229–238, 2010.
- [12] P. A. Liu, Y. F. Fang, and T.-F. Lu. Classification and general kinematic models of 3-DOF planar parallel manipulators. In *Proceedings of the 7th International Conference on Computer-Aided Industrial Design and Conceptual Design (CAIDCD)*, November 17-19, 2006. art. no. 4127065.
- [13] R. Longchamp. *Commande numérique de systèmes dynamiques: Cours d'automatique*. Presses Polytechniques et Universitaires Romandes, Lausanne, Switzerland, 2006.
- [14] X. Pei, J. Yu, G. Zong, S. Bi, and H. Su. The modeling of cartwheel flexural hinges. *Mechanism and Machine Theory*, 44(10):1900–1909, 2009.
- [15] K. E. Petersen. Silicon as a mechanical material. *Proceedings of the IEEE*, 70(5):420–457, 1982.
- [16] S. S. Rao. *Mechanical Vibrations*. Pearson / Prentice Hall, 4th edition, 2004.
- [17] E. Sarajlic, C. Yamahata, M. Cordero, and H. Fujita. An electrostatic 3-phase linear stepper motor fabricated by vertical trench isolation technology. *Journal of Micromechanics and Microengineering*, 19(7): art. no. 074001, 2009.
- [18] E. Sarajlic, C. Yamahata, M. Cordero, and H. Fujita. Three-phase electrostatic rotary stepper micromotor with a flexural pivot bearing. *Journal of Microelectromechanical Systems*, 19(2):338–349, 2010.
- [19] E. Sarajlic, C. Yamahata, M. Cordero, L. Jalabert, T. Iizuka, and H. Fujita. Single mask 3-phase electrostatic rotary stepper micromotor. In *Proceedings of the 15th International Conference on Solid-State Sensors, Actuators and Microsystems (Transducers)*, pages 1505–1508, Denver, CO, USA, June 21-25, 2009.
- [20] J. Sone, T. Mizuma, M. Masunaga, S. Mochizuki, E. Sarajic, C. Yamahata, and H. Fujita. Analysis of the characteristics of a rotary stepper micromotor. *IEEE Transactions on Sensors and Micromachines*, 130(7):310–316, 2010.
- [21] M. Stranczl. A monolithic microrobotic arm in silicon, Autumn 2009. EPFL Semester Project.
- [22] M. Stranczl, E. Sarajlic, G. J. M. Krijnen, H. Fujita, M. A. M. Gijs, and C. Yamahata. Modal analysis and modeling of a frictionless electrostatic rotary stepper micromotor. In *Proceedings of the 24th IEEE International Conference on Micro Electro Mechanical Systems (MEMS)*, pages 1257–1260, Cancún, Mexico, January 23-27, 2011.
- [23] W. C. Tang, M. G. Lim, and R. T. Howe. Electrostatic comb drive levitation and control method. *Journal of Microelectromechanical Systems*, 1(4):170–178, 1992.

-
- [24] B. P. Trease, Y.-M. Moon, and S. Kota. Design of large-displacement compliant joints. *Journal of Mechanical Design, Transactions of the ASME*, 127(4):788–798, 2005.
- [25] W. S. N. Trimmer and K. J. Gabriel. Design considerations for a practical electrostatic micro-motor. *Sensors and Actuators*, 11(2):189–206, 1987.
- [26] E. van Groesen and J. Molenaar. *Continuum modeling in the physical sciences*, chapter Dimensional analysis and scaling. Society for Industrial and Applied Mathematics, 2007.
- [27] J. Wu, J. Wang, L. Wang, and Z. You. Performance comparison of three planar 3-DOF parallel manipulators with 4-RRR, 3-RRR and 2-RRR structures. *Mechatronics*, 20(4):510–517, 2010.
- [28] C. Yamahata. Temporally aliased video analysis: An undersampling method for modal analysis of linear and nonlinear systems. Unpublished results (internal presentation, LMIS2, EPFL), December 8, 2010.
- [29] C. Yamahata, E. Sarajlic, G. J. M. Krijnen, and M. A. M. Gijs. Subnanometer translation of microelectromechanical systems measured by discrete Fourier analysis of CCD images. *Journal of Microelectromechanical Systems*, 19(5):1273–1275, 2010.
- [30] X. M. Zhang, A. Q. Liu, H. Cai, A. B. Yu, and C. Lu. Retro-axial VOA using parabolic mirror pair. *IEEE Photonics Technology Letters*, 19(9):692–694, 2007.

Appendix A

A.1 Influence of the rigid element on the butterfly stiffness

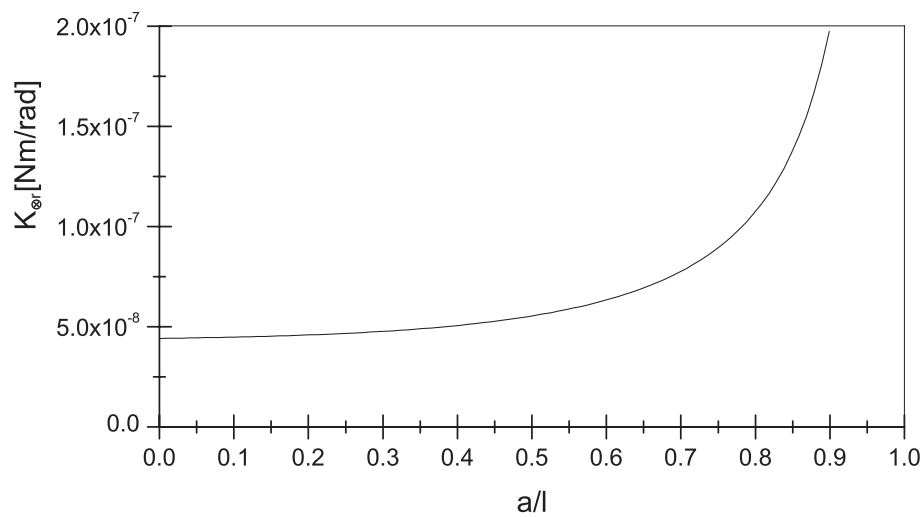


Figure A.1: Stiffness of the reinforced butterfly pivot $K_{\otimes r}$ depending on the ratio of reinforced element length a over the total beam length l for a beam width b of $2 \mu\text{m}$. The other dimensions are similar as for the design v.1.0.

A.2 Reinforced RCC pivot stiffness

The reinforced RCC pivot stiffness $K_{RCC,r}$ can be calculated using the conservation of energy principle: The energy stored in the butterfly pivot is similar to the energy stored in the four RCC pivot.

$$\frac{1}{2}K_{\otimes,r}(\theta_{\otimes,r})^2 = 4 \cdot \frac{1}{2}K_{RCC,r}(\theta_{RCC,r})^2$$

Where the index RCC refers to the RCC pivot, $\theta_{\otimes,r}$ is the reinforced butterfly pivot rotation, $\theta_{RCC,r}$ the reinforced RCC pivot rotation, $K_{\otimes,r}$ the reinforced butterfly pivot stiffness and $K_{RCC,r}$ reinforced RCC pivot stiffness. As:

$$\theta_{RCC,r} = \frac{\theta_{\otimes,r}}{4}$$

Then:

$$\frac{1}{2}K_{\otimes,r}(\theta_{\otimes,r})^2 = 4 \cdot \frac{1}{2}K_{RCC,r}\left(\frac{\theta_{\otimes,r}}{4}\right)^2$$

Then:

$$K_{\otimes,r} = \frac{K_{RCC,r}}{4}$$

With the same calculations:

$$K_{\otimes} = \frac{K_{RCC}}{4}$$

A.3 Silicon properties

	Yield Strength (10^{10} dyne/cm ²)	Knoop Hardness (kg/mm ²)	Young's Modulus (10^{12} dyne/cm ²)	Density (gr/cm ³)	Thermal Conductivity (W/cm°C)	Thermal Expansion ($10^{-6}/^{\circ}\text{C}$)
*Diamond	53	7000	10.35	3.5	20	1.0
*SiC	21	2480	7.0	3.2	3.5	3.3
*TiC	20	2470	4.97	4.9	3.3	6.4
*Al ₂ O ₃	15.4	2100	5.3	4.0	0.5	5.4
*Si ₃ N ₄	14	3486	3.85	3.1	0.19	0.8
*Iron	12.6	400	1.96	7.8	0.803	12
SiO ₂ (fibers)	8.4	820	0.73	2.5	0.014	0.55
*Si	7.0	850	1.9	2.3	1.57	2.33
Steel (max. strength)	4.2	1500	2.1	7.9	0.97	12
W	4.0	485	4.1	19.3	1.78	4.5
Stainless Steel	2.1	660	2.0	7.9	0.329	17.3
Mo	2.1	275	3.43	10.3	1.38	5.0
Al	0.17	130	0.70	2.7	2.36	25

*Single crystal. See Refs. 8, 9, 10, 11, 141, 163, 166.

Figure A.2: Silicon properties. Figure reproduced from [15].

ELASTIC MODULUS VALUES FOR SILICON

Load Case	Symbol	Appropriate Value for Silicon
Axial or narrow beam bending loads <110> directions ("X or Y axis") <100> directions ("45° off-axis")	E	169 GPa 130 GPa
Plate bending, $\nu = 0.064$ for <110> in (100)	E'_{110}	170 GPa
Thin film biaxial stress/strain, (100) plane	B_{100}	180 GPa
Shear load, twisting a <110> ("X" or "Y") beam	G	50.9 GPa
Stress concentrations	E_V	166 GPa
Hydrostatic loads	B	97.8 GPa
Temperature Coefficient of E	TCE	~ -60 ppm/ $^{\circ}\text{C}$
Orthotropic material model properties for a standard (100) silicon wafer		$E_x = E_y = 169$ GPa, $E_z = 130$ GPa $\nu_{yz} = 0.36$, $\nu_{zx} = 0.28$, $\nu_{xy} = 0.064$ $G_{xy} = G_{zx} = 79.6$ GPa, $G_{xy} = 50.9$ GPa

Figure A.3: Silicon properties. Figure reproduced from [11].

A.4 Region of interest (ROI), temporally aliased video microscopy

The measurements have been performed using the temporally aliased video analysis. Figure A.4 illustrate the micromotor's ROI recorded using a Keyence VHX-600 microscope. The motion of the rotor and the butterfly internal structure depending on the excitation frequency have been extracted from the two corresponding zones observed.

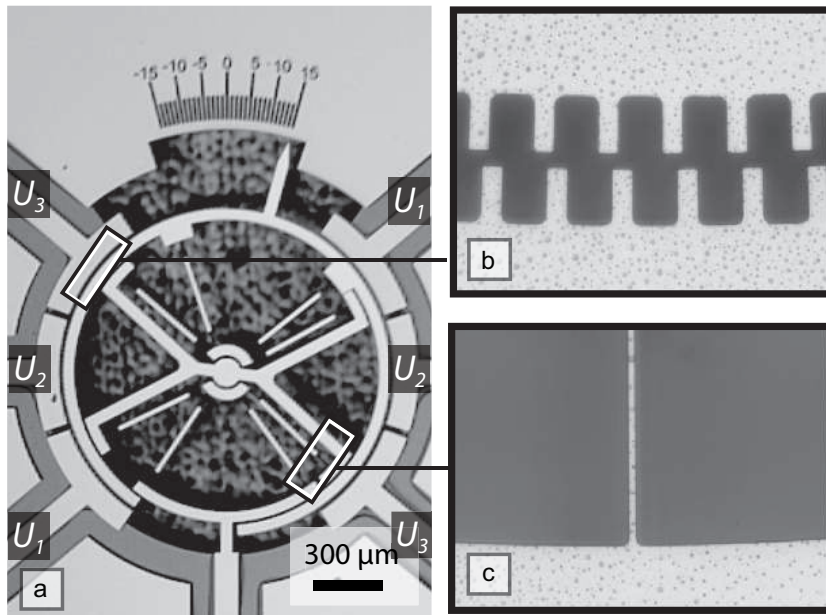


Figure A.4: Region of interest (ROI): (a) Schematic of the micromotor with the zone recorded: the butterfly internal structure and the rotor (b) micrograph of the micromotor with the zone recorded. (c) Rotor periodic pattern used for temporally aliased video analysis (d) corresponding zone on butterfly (beam)

A.5 High-speed camera measurement

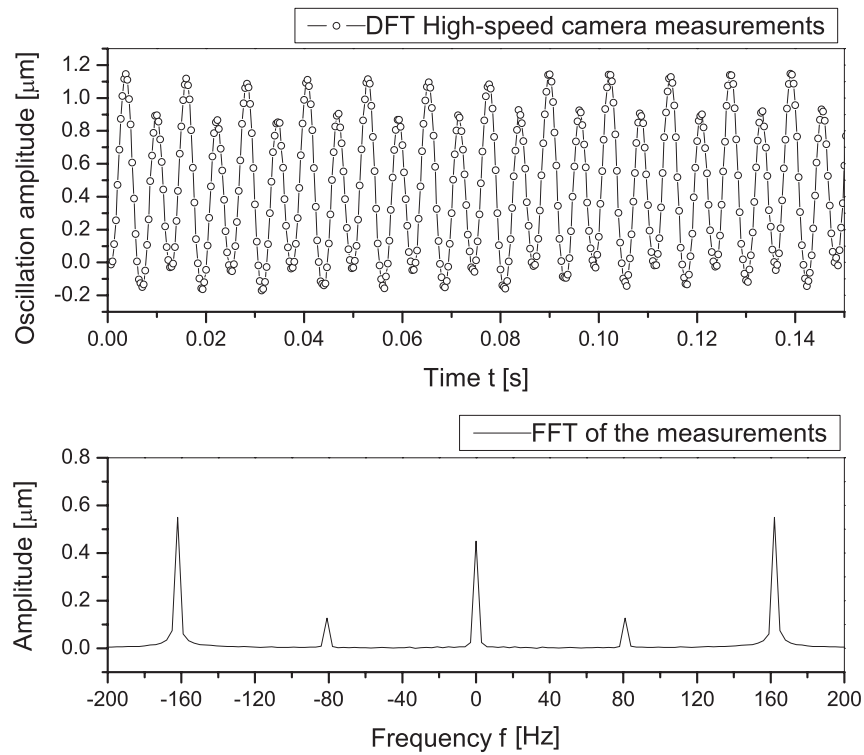


Figure A.5: High-speed camera measurement for a 81 Hz excitation frequency: (top) Data obtained with a high-speed camera recording analyzed by DFT; (bottom) FFT of the high-speed camera data. The main oscillations are at twice the excitation frequency f_{exc}

A.6 Variable substitution from linear to rotational model

With the following substitutions, the linear model can be adapted to circular model:

- The position x must be substituted with the angular position θ .
- The inertial mass m must be substituted with the inertial I .
- The geometric periode of the teeth must be substituted with the corresponding angle periode Γ_x .
- The linear spring constant k must be substituted with the corresponding angular stiffness k_θ .

A.7 Newton's law equation

Considering the rotor as an isolated component of the system, the second law of Newton states that the inertial force, $m \ddot{x}$, equals the sum of the external forces acting on the rotor. They are: the driving force $F_{dr}(t)$, the spring force F_s , which is linearly proportional to the displacement x , and the frictional forces F_f , which is supposed to be linearly dependent to the velocity of the rotor and acting reversely to its motion [16].

$$m\ddot{x} = F_{dr}(t) - F_f(t) - F_s \quad (\text{A.1})$$

Which can be written, with $F_f(t) = c\dot{x}$; $F_s = kx$:

$$m\ddot{x} + c\dot{x} + kx = F_{dr}(x, t) \quad (\text{A.2})$$

A.8 Nondimensionalization

We define:

$$t = \tau t_c, \quad x = \chi x_c, \quad (\text{A.3})$$

with t_c x_c , dimensional characteristic unit which have to be fixed and τ and χ coefficient of these unit.

Then, for convenient reason, we expose the following relations:

$$\begin{aligned} dt &= t_c d\tau, & \frac{d\tau}{dt} &= \frac{1}{t_c} \\ \frac{d}{dt} &= \frac{d\tau}{dt} \frac{d}{d\tau} = \frac{1}{t_c} \frac{d}{d\tau}; & \frac{d^2}{dt^2} &= \frac{1}{t_c^2} \frac{d^2}{d\tau^2}. \end{aligned} \quad (\text{A.4})$$

With (6.21) and (A.4), the equation (6.19) can be rewritten:

$$\frac{x_c}{t_c^2} \frac{d^2 \chi}{d\tau^2} + \frac{2\zeta w_0 x_c}{t_c} \frac{d\chi}{d\tau} + w_0^2 x_c \chi + \frac{C_0 \omega_x U_1^2}{4m} \sin(w_x x_c \chi) = -\frac{C_0 \omega_x U_2^2}{4m} \sin(w_x x_c \chi - \frac{2\pi}{3}) (\sin(\Omega \tau t_c))^2.$$

We divide by the first term coefficient and with the convention $\frac{d\chi}{d\tau} = \dot{\chi}$; $\frac{d^2 \chi}{d\tau^2} = \ddot{\chi}$:

$$\ddot{\chi} + 2\zeta w_0 t_c \dot{\chi} + t_c^2 w_0^2 \chi + \frac{C_0 \omega_x U_1^2 t_c^2}{4m x_c} \sin(w_x x_c \chi) = -\frac{C_0 \omega_x U_2^2 t_c^2}{4m x_c} \sin(w_x x_c \chi - \frac{2\pi}{3}) (\sin(\Omega \tau t_c))^2.$$

We define the coefficient a as the ratio of the phase one voltage report to the phase two:

$$a = \left(\frac{U_1}{U_2} \right)^2$$

Then:

$$\ddot{\chi} + 2\zeta w_0 t_c \dot{\chi} + t_c^2 w_0^2 \chi + \frac{C_0 \omega_x a U_2^2 t_c^2}{4m x_c} \sin(w_x x_c \chi) = -\frac{C_0 \omega_x U_2^2 t_c^2}{4m x_c} \sin(w_x x_c \chi - \frac{2\pi}{3}) (\sin(\Omega \tau t_c))^2.$$

We chose t_c x_c in order to simplify the third and then the fifth coefficient:

$$t_c = \frac{1}{w_0} = \sqrt{\frac{m}{k}}; \quad x_c = \frac{C_0 \omega_x U_2^2}{4k}.$$

Then:

$$\boxed{\ddot{\chi} + 2\zeta \dot{\chi} + \chi + a \sin(w_x x_c \chi) = -\sin(w_x x_c \chi - \frac{2\pi}{3}) (\sin(\Omega t_c \tau))^2}$$

A.9 Maple code

A.9.1 Case I

```

restart;
with(plots) : with(DEtools) :
dif1 := diff((x(t)), t) = y(t) :
xlim := 4.5 : ylim := 3 : tstart := 0 : tlim := 10000 : steptime := 1 :
x0 := 0 : y0 := 0 :
f0 := 0 : flim := 400 :
a :=  $\frac{0^2}{4^2}$  :
w :=  $2 \pi \cdot \left( f0 + \frac{flim - f0}{tlim} \cdot \frac{t}{2} \right)$  :
dif2 := diff((y(t)), t) = -0.043 · y(t) - 1 · x(t) - sin $\left( \frac{0.2 \cdot 2 \cdot \pi}{10.838} \cdot x(t) - \frac{2 \cdot \pi}{3} \right)$  ·  $\left( \frac{1}{2} \right)$ 
+  $\frac{1}{2} \sin\left( \frac{w \cdot 1}{2 \pi \cdot 163} \cdot t \right)^2$  - a · sin $\left( \frac{0.2 \cdot 2 \cdot \pi}{10.838} \cdot x(t) \right)$  :
sys := [dif1, dif2] :
window := x = -xlim .. xlim, y = -ylim .. ylim :
Pendulum := DEplot(sys, [x(t), y(t)], t = tstart .. tlim, {[0, x0, y0]}, stepsize = steptime, scene = [t,
x(t)], linecolor = 'blue', maxfun = 5000000) :
display({Pendulum}, title = "Pendulum forced oscillation", font = [Times, Bold, 12]);
z := -0.043 · y(t) - 1 · x(t) - sin $\left( \frac{0.2 \cdot 2 \cdot \pi}{10.838} \cdot x(t) - \frac{2 \cdot \pi}{3} \right)$  ·  $\left( \frac{1}{2} + \frac{1}{2} \sin\left( \frac{w \cdot 1}{2 \pi \cdot 163} \cdot t \right) \right)^2$  - a
· sin $\left( \frac{0.2 \cdot 2 \cdot \pi}{10.838} \cdot x(t) \right)$  :
dsys :=  $\left\{ \frac{d}{dt} x(t) = y(t), \frac{d}{dt} y(t) = z, x(0) = x0, y(0) = y0 \right\}$  :
steps :=  $\left[ \text{seq}\left( i \cdot \text{steptime}, i = tstart .. \frac{tlim}{\text{steptime}} \right) \right]$  :
dsn1 := dsolve(dsys, numeric, output = Array(steps), maxfun = 5000000);

```

Figure A.6: Maple code corresponding to Case I.

A.9.2 Case II

```

restart;
with(plots) : with(DEtools) :
dif1 := diff((x(t)), t) = y(t) :
xlim := 4.5 : ylim := 3 : tstart := 0 : tlim := 10000 : steptime := 1 :
x0 := 0 : y0 := 0 :
f0 := 0 : flim := 200 :
a :=  $\frac{0^2}{4^2}$  :
w :=  $2\pi \cdot \left( f0 + \frac{flim - f0}{tlim} \cdot \frac{t}{2} \right)$  :
dif2 := diff((y(t)), t) = -0.043 · y(t) - 1 · x(t) -  $\sin\left(\frac{0.2 \cdot 2 \cdot \pi}{10.838} \cdot x(t) - \frac{2 \cdot \pi}{3}\right) \cdot \sin\left(\frac{w \cdot 1}{2 \pi \cdot 163} \cdot t\right)^2 - a$ 
·  $\sin\left(\frac{0.2 \cdot 2 \cdot \pi}{10.838} \cdot x(t)\right)$  :
sys := [dif1, dif2] :
window := x = -xlim .. xlim, y = -ylim .. ylim :
Pendulum := DEplot(sys, [x(t), y(t)], t = tstart .. tlim, {[0, x0, y0]}, stepsize = steptime, scene = [t,
x(t)], linecolor = 'blue', maxfun = 5000000) :
display({Pendulum}, title = "Pendulum forced oscillation", font = [Times, Bold, 12]);
z := -0.043 · y(t) - 1 · x(t) -  $\sin\left(\frac{0.2 \cdot 2 \cdot \pi}{10.838} \cdot x(t) - \frac{2 \cdot \pi}{3}\right) \cdot \sin\left(\frac{w \cdot 1}{2 \pi \cdot 163} \cdot t\right)^2 - a \cdot \sin\left(\frac{0.2 \cdot 2 \cdot \pi}{10.838}$ 
· x(t) ) :

dsys :=  $\left\{ \frac{d}{dt} x(t) = y(t), \frac{d}{dt} y(t) = z, x(0) = x0, y(0) = y0 \right\}$  :
steps :=  $\left[ seq\left(i \cdot steptime, i = tstart .. \frac{tlim}{steptime}\right) \right]$  :
dsn1 := dsolve(dsys, numeric, output = Array(steps), maxfun = 5000000);

```

Figure A.7: Maple code corresponding to Case II.

A.10 Micromotor dimensions

A.10.1 v.1

Parameters	Symbol	Value
Rotor radius	r	$690\mu m$
Beam length	l	$465\mu m$
Reinforced beam length	a	$325\mu m$
Beam width	b	$2\mu m$
Beam height	h	$50\mu m$
Distance to virtual pivot	p	$115\mu m$
Tooth width	w	$4\mu m$
Tooth height	h_p	$50\mu m$
Rotor/stator gap	g	$1.5\mu m$
Number of active teeth per phase	n	80
Angular teeth pitch	α	0.9°

Table A.1: Geometrical parameters: micromotor v.1.

A.10.2 v.2.0

Parameters	Symbol	Value
Rotor internal radius	r_1	$720\mu m$
Rotor external radius	r_2	$821\mu m$
Beam length	l	$465\mu m$
Reinforced beam length	a	$325\mu m$
Beam width	b	$2\mu m$
Beam height	h	$50\mu m$
Distance to virtual pivot	p	$115\mu m$
Tooth width	w	$4\mu m$
Tooth height	h_p	$50\mu m$
Rotor/stator gap	g	$1.5\mu m$
Number of active teeth per phase per radius	n	80
Angular teeth pitch	α	0.9°

Table A.2: Geometrical parameters: micromotor v.2.0.

A.10.3 v.2.1

Parameters	Symbol	Value
Rotor internal radius	r_1	$810\mu m$
Rotor external radius	r_2	$923\mu m$
Beam length	l	$465\mu m$
Reinforced beam length	a	$325\mu m$
Beam width	b	$2\mu m$
Beam height	h	$50\mu m$
Distance to virtual pivot	p	$115\mu m$
Tooth width	w	$4\mu m$
Tooth height	h_p	$50\mu m$
Rotor/stator gap	g	$1.5\mu m$
Number of active teeth per phase per radius	n	80
Angular teeth pitch	α	0.9°

Table A.3: Geometrical parameters: micromotor v.2.1.

A.11 Micromotor v.1

A.11.1 Micromotor v.1

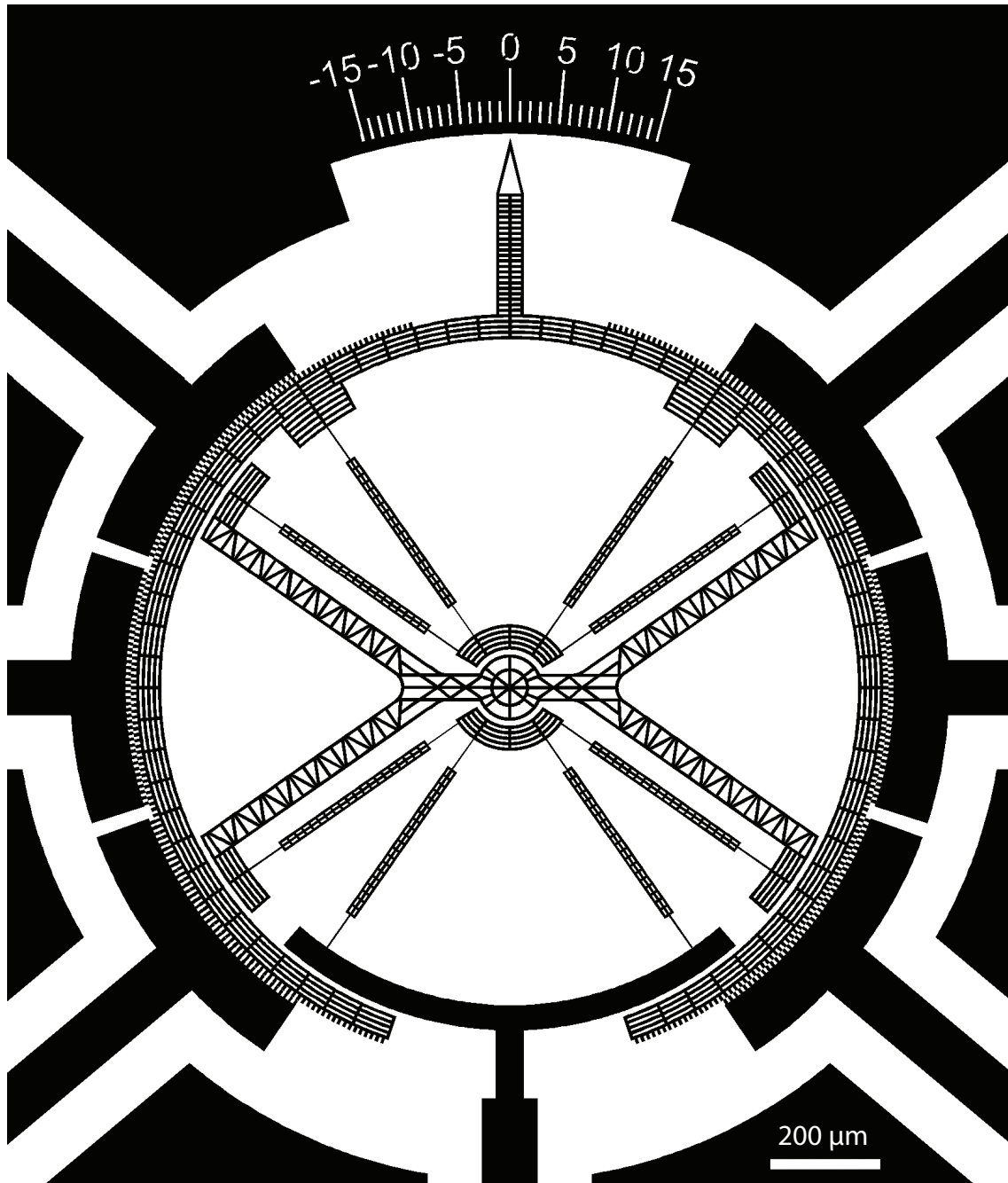


Figure A.8: Design of the micromotor v.1

A.11.2 Fabrication process considerations

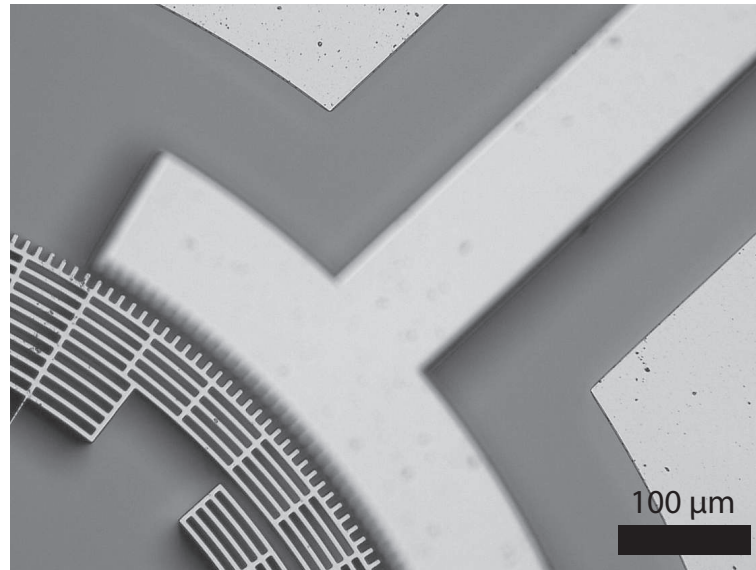


Figure A.9: Delamination of the SOI wafer: the phase 1 is out-of-plane.

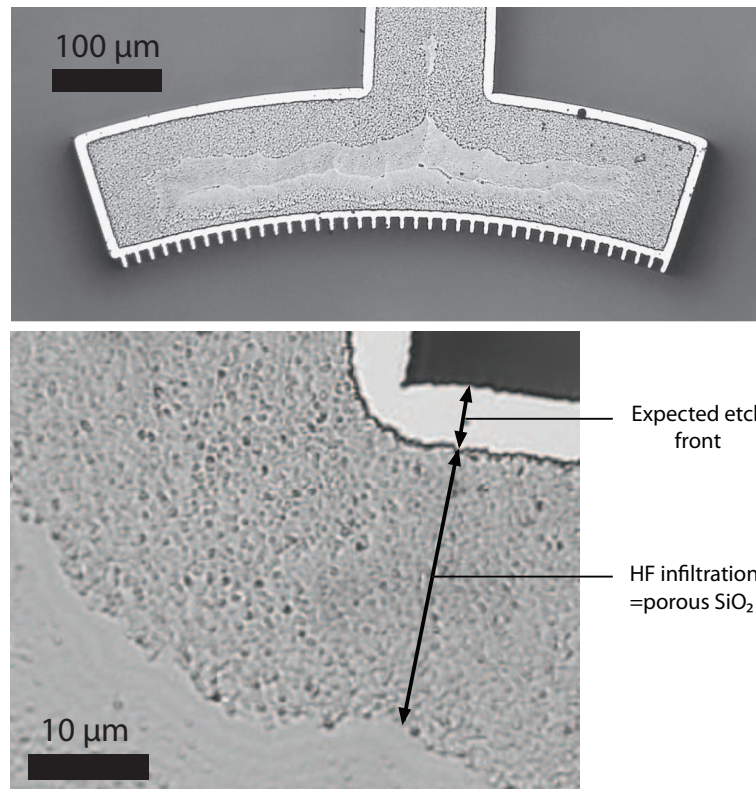


Figure A.10: HF etching of the SiO₂ oxide. The observation of the oxide reveals a HF diffusion zone which makes the sacrificial layer porous.

A.12 Motor v.2

A.12.1 Micromotor v.2.0

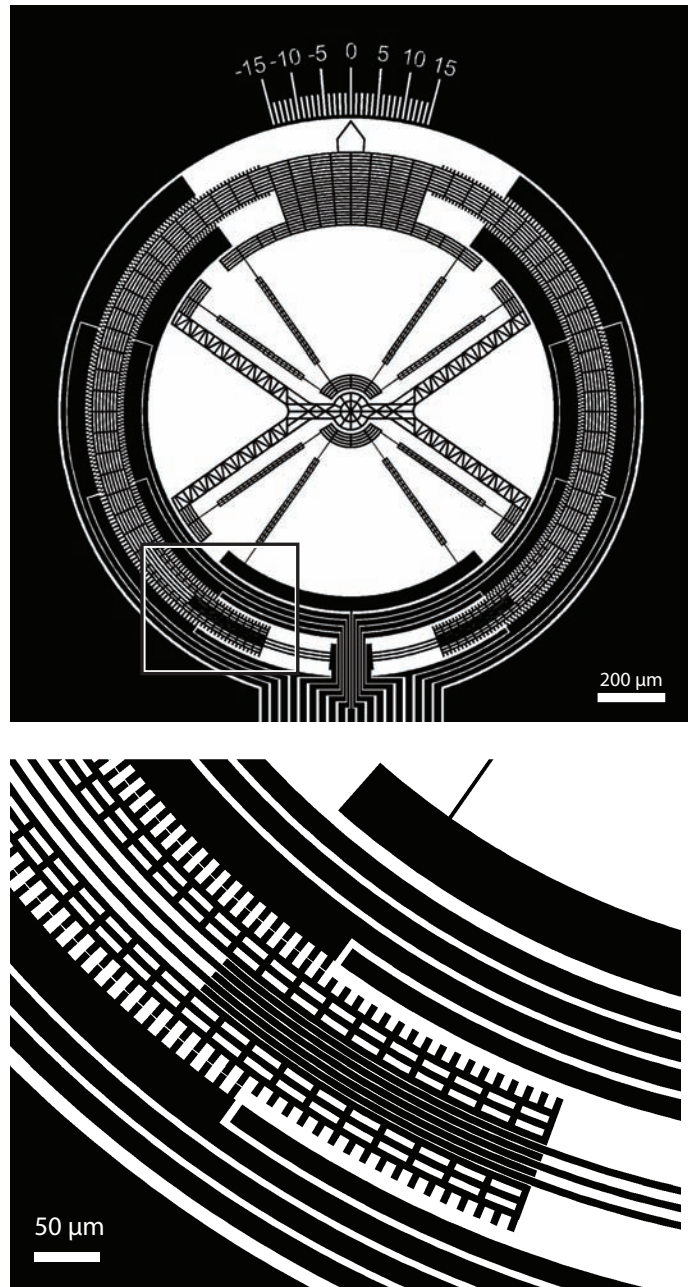


Figure A.11: Micromotor v.2.0: (top) Design of the micromotor v.2.0; (bottom) Detail of the capacitive sensor.

A.12.2 Micromotor v.2.0 with a torque sensor

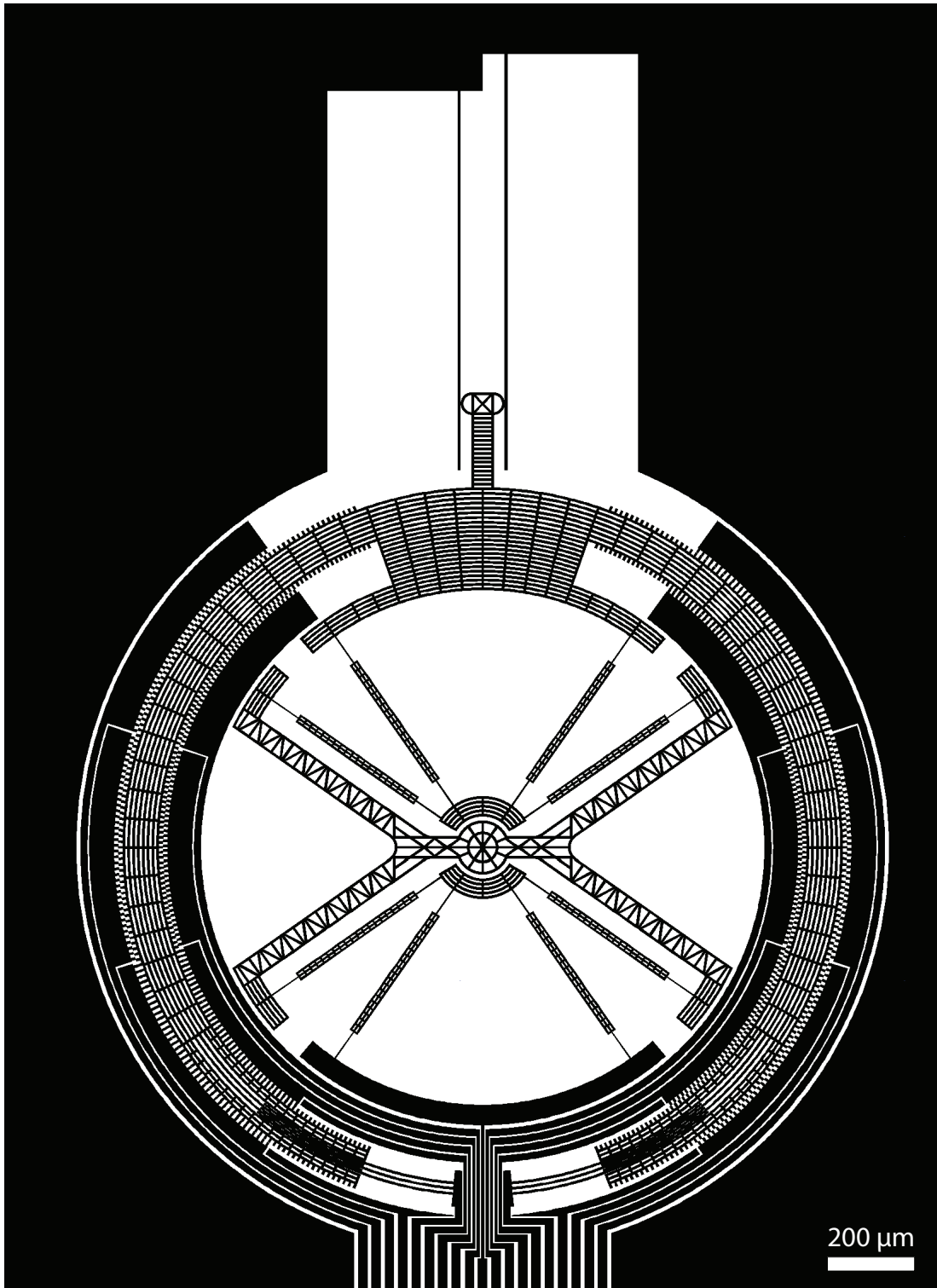


Figure A.12: Micromotor version 2.0: Micromotor with an AFM-like probe sensor for torque measurement.

A.12.3 Fabrication process considerations

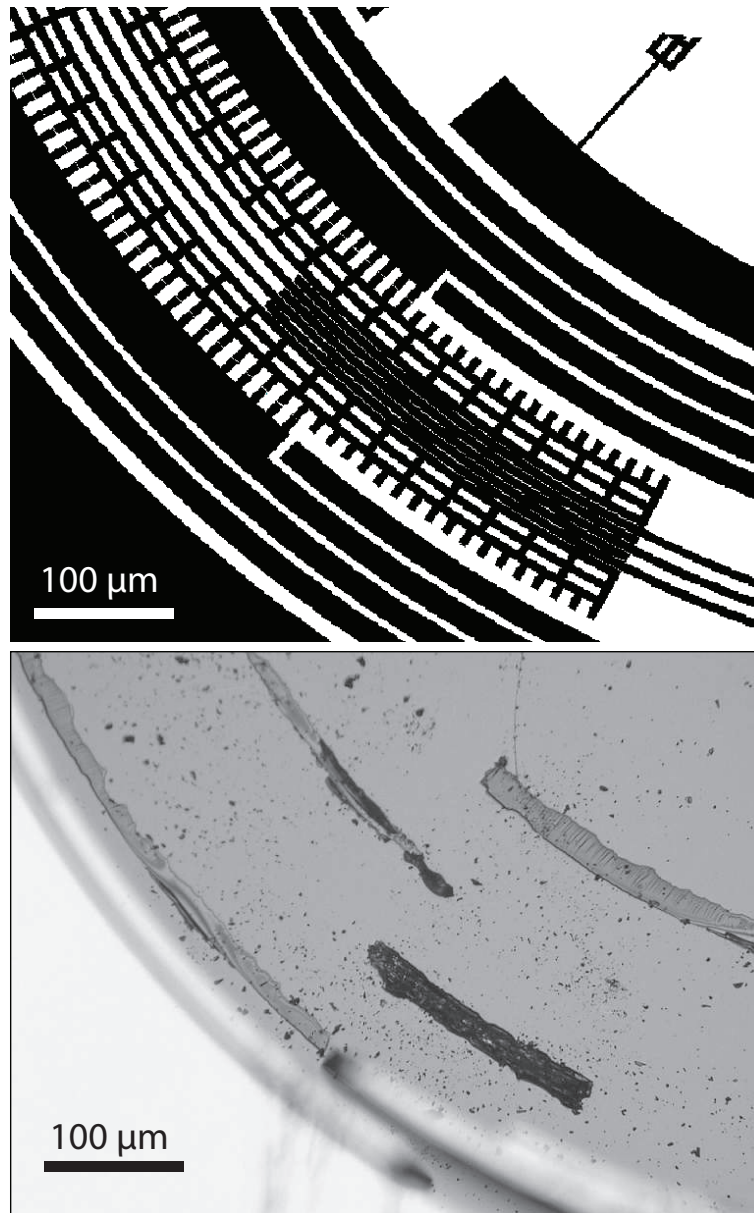


Figure A.13: Micromotor version 2.0: (top) Detail of the capacitive sensor; (bottom) Corresponding sacrificial oxide layer region after HF etching: The top Si layer has been scratched. It reveals that the capacitive comb is not etched as the HF vapor does not diffuse into the 1 μm gap of the comb.

A.13 Demonstrator

A.13.1 Demonstrator design

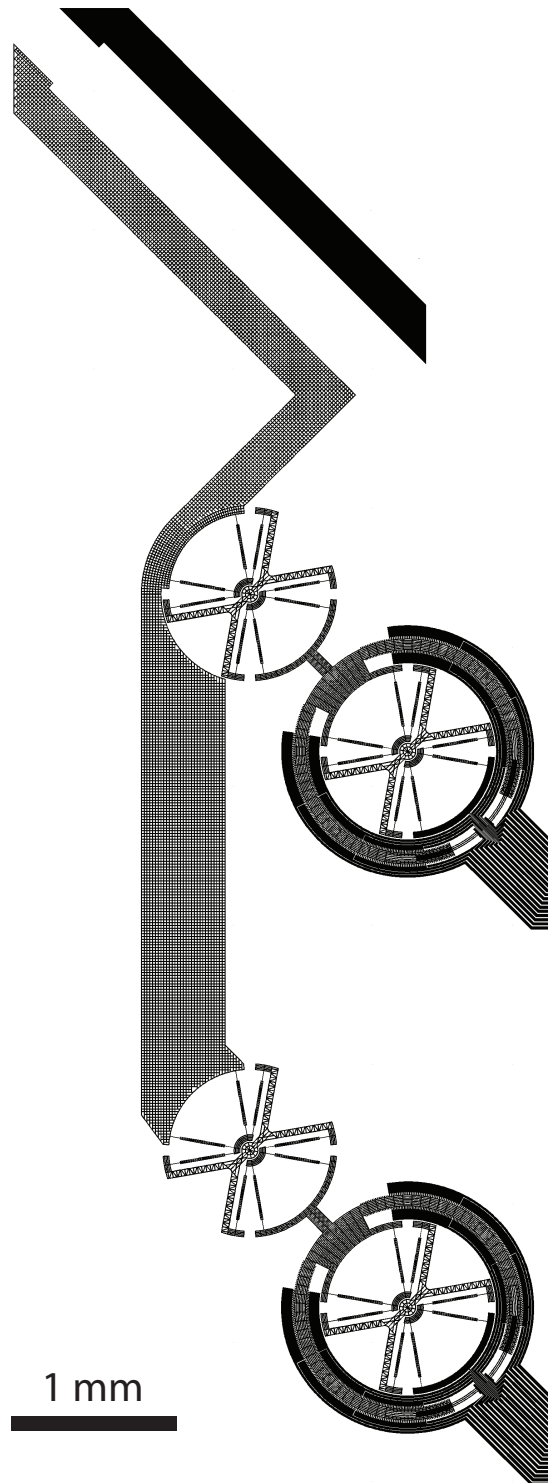
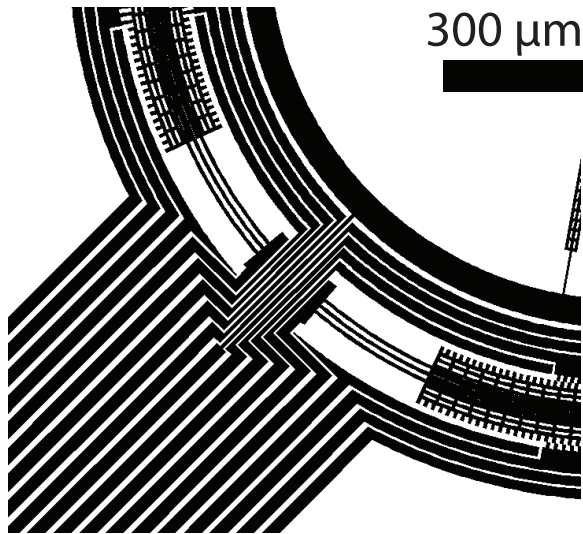
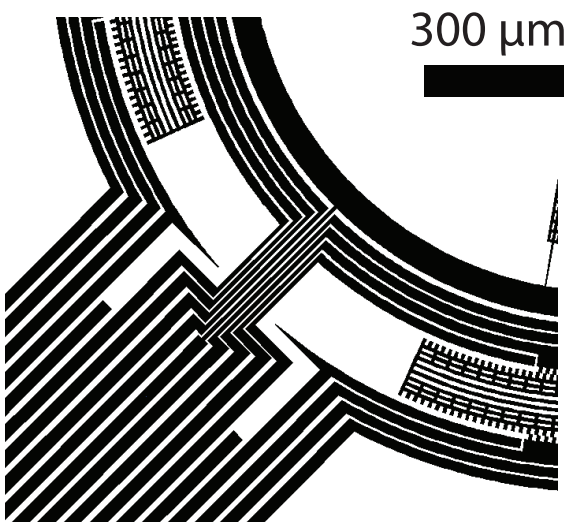


Figure A.14: Microgripper demonstrator design.



Design with
a differential
capacitive sensor



Design without
a differential
capacitive sensor

Figure A.15: Microgripper demonstrator design: detail of the capacitive sensor region: (top) Design with a capacitive sensor; (bottom) Design without a capacitive sensor.

A.13.2 Fabrication process considerations

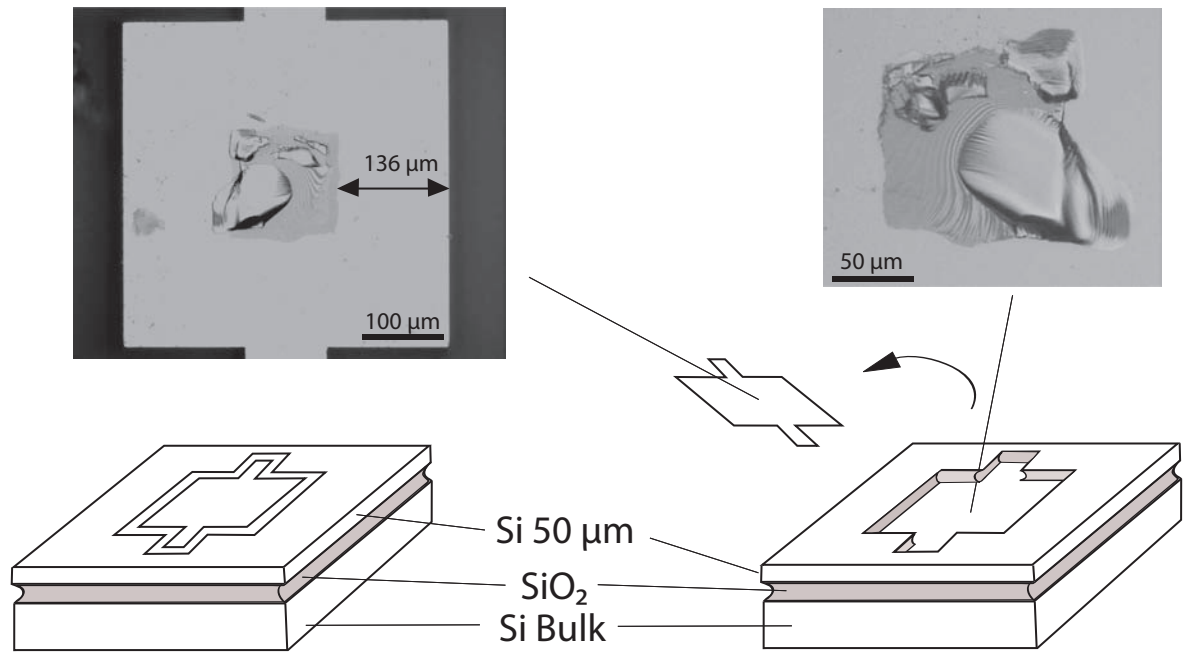


Figure A.16: Details of the microrobot after HF etching: the scratched top Si layer can be observed to measure the SiO₂ etching depth.

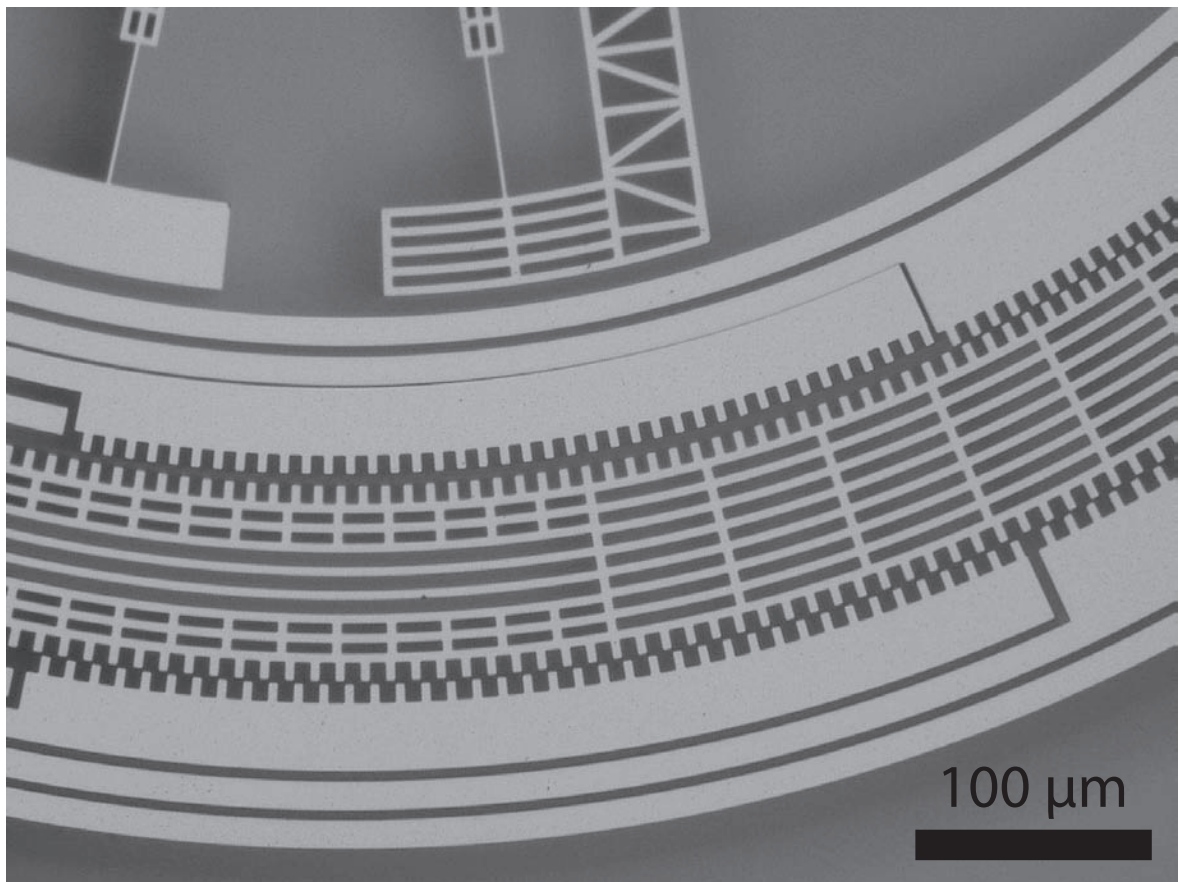


Figure A.17: Details of the microrobot after HF etching: the stator phases are over etched.

A.14 Micromotor v.2.1

A.14.1 Micromotor v.2.1

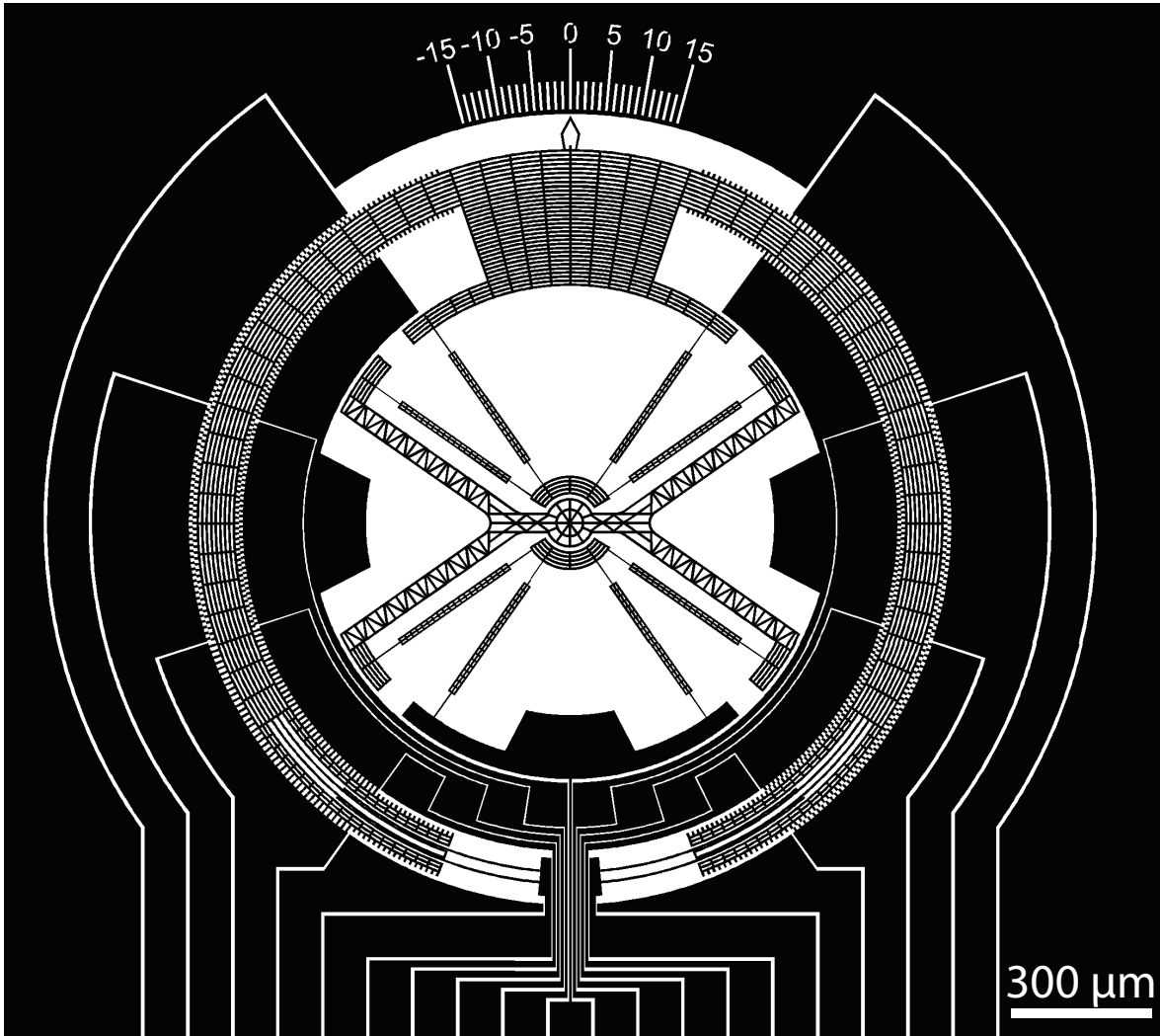


Figure A.18: Micromotor version 2.1: Design with a needle hand

A.14.2 Micromotor v.2.1 with a torque sensor

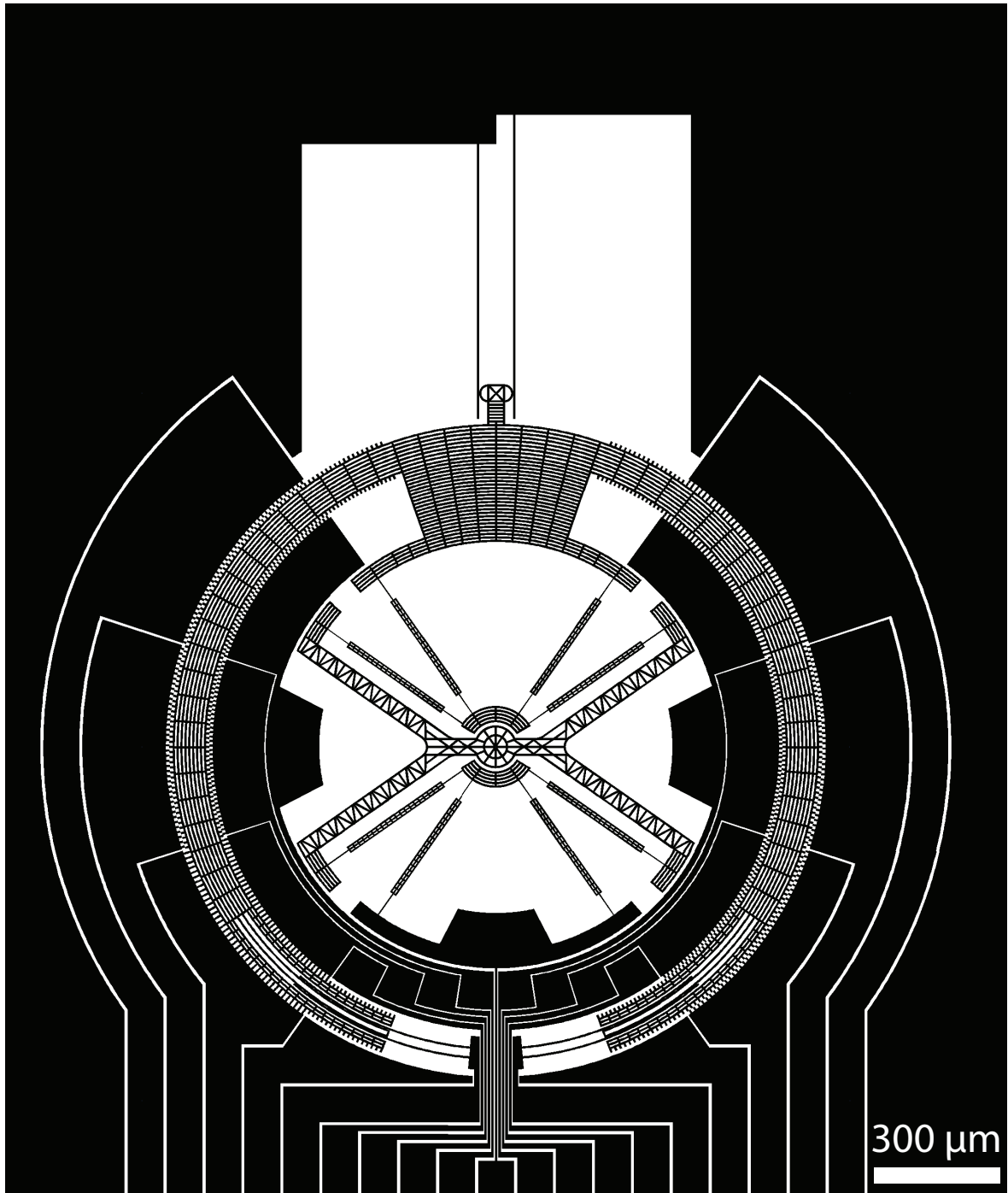


Figure A.19: Micromotor version 2.1: Design with an AFM-like torque sensor.

A.14.3 Differential capacitive

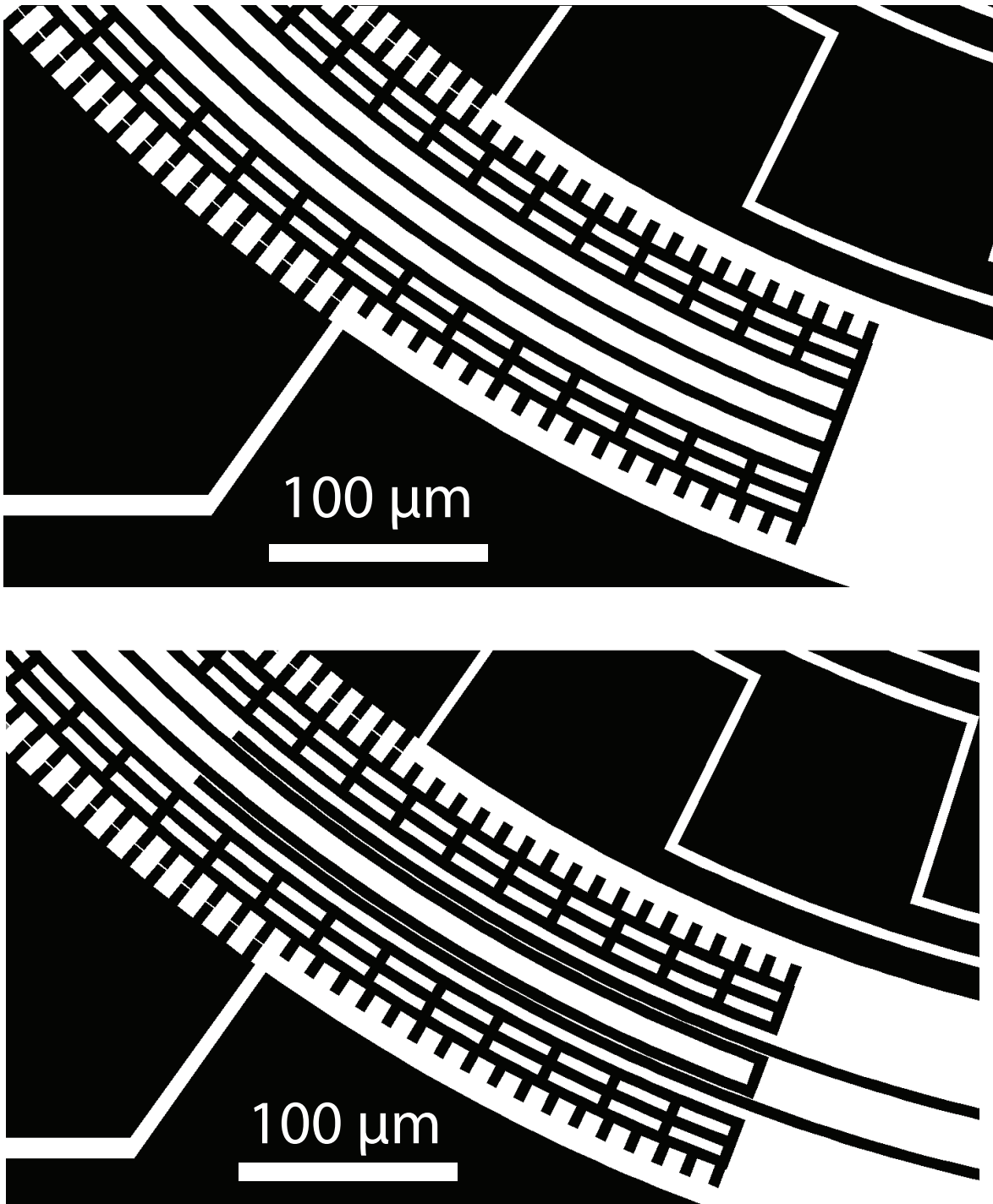


Figure A.20: Micromotor version 2.1: Detail of the capacitive sensor: (top) Design without capacitive sensor; (bottom) Design of the capacitive sensor with enlarged gap for HF vapor diffusion.

A.15 Process flow and Runcard

Semester Project Master Project Thesis Other

A monolithic microrobotic arm in silicon

Description

We have developed a 3-phase electrostatic rotary stepper micromotor based on SOI technology [1]. The motor employs flexural pivot bearing for suspension of the rotor to avoid mechanical friction during operation. We improve the design in order to reach a one mask process using deep Reactive Ion Etching in a SOI wafer [2]. Figure 1 is a SEM micrograph of the previous fabricated micromotor.

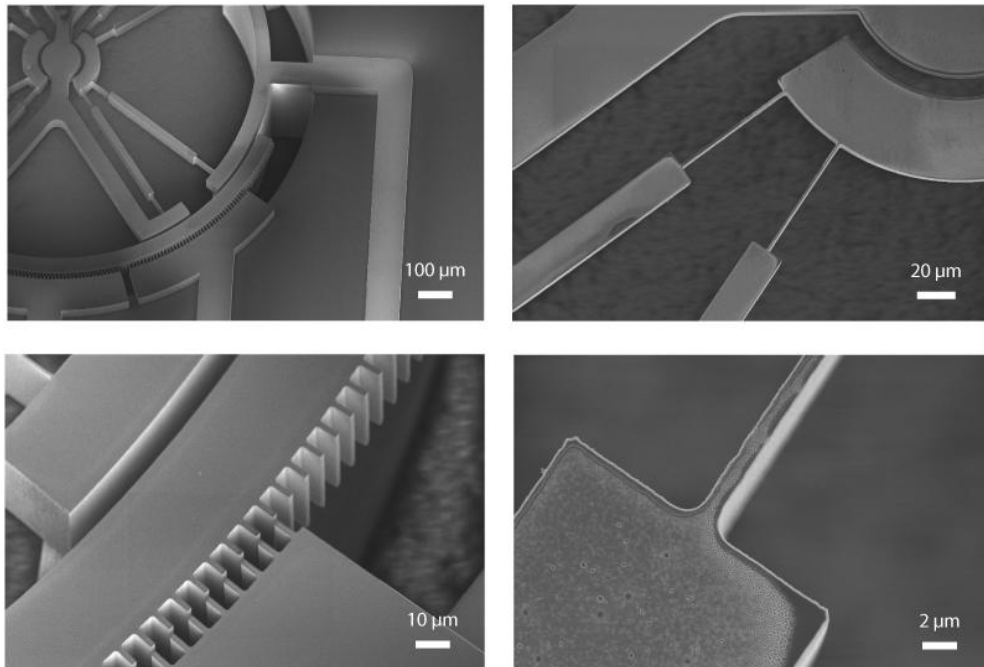


Figure 1: SEM micrograph of a rotary stepper micromotor fabricated with SOI technology.




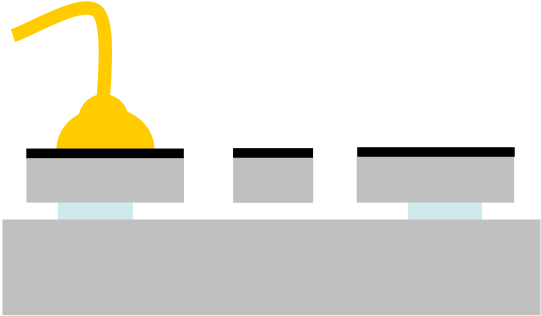
[1] E. Sarajlic, C. Yamahata, M. Cordero, L. Jalabert, T. Iizuka, H. Fujita, "Single mask 3-phase electrostatic rotary stepper micromotor," *Proc. 15th Int. Conf. on Solid-State Sensors, Actuators and Microsystems (Transducers 2009)*, Denver, Colorado, USA, June 21 - 25, 2009.

[2] M. Stranczl, C. Yamahata, "A monolithic microrobotic arm in silicon", Semester project, EPFL, January 2010.

Technologies used			
Mask fabrication, evaporation, positive resist, Dry etching, Wet etching, SEM			
Photolith masks			
Mask #	Critical Dimension	Critical Alignment	Remarks
1	1 – 1.5 μm	–	Silicon structuration (device layer of the SOI) Smallest feature: gap between rotor and stator teeth
1	50 μm	–	High aspect ratio etching of the device layer
Mask #1: For the frontside (microstructures)			
Substrate Type			
SOI, 50 μm device layer, 0.1-0.5 Ohm.cm / 4 μm buried oxide layer / 380 μm thick handling wafer, \varnothing 100 mm (4" wafer), Double Side polished >1000 Ohm.cm. Ultrasil SOI-380-4-50			

Process outline

Step	Process description	Cross-section after process
01	Substrate : SOI <i>Metal Evaporation</i> Machine: LAB600H Metal: Al Thickness : 100 nm	
02	<i>Photolitho – frontside</i> Machine: Rite Track 88 Series PR : AZ 92xx ; 2 μm Mask : #1 ; CD = 1 μm No EBR	
03	<i>Dry Etch</i> Material: Al Machine: STS Multiplex ICP	

<p>04</p>	<p><i>Dry Etch – frontside</i> Material : <i>Si</i> Machine: <i>Alcatel AMS 200</i> Depth : <i>50 μm (device layer thickness)</i></p>	
<p>05</p>	<p><i>Resist stripping</i> Wet bench + Plasma O₂ Machines: <i>UFT Resist + Tepla</i></p>	
<p>06</p>	<p><i>Vapor HF – frontside</i> Material : <i>SiO₂</i> Machine: <i>Idonus HF VPE-100</i> Depth : <i>4 μm (BOX underetching)</i></p>	
<p>07</p>	<p><i>Automatic dicing saw or Manual wafer cutting</i> + <i>Wire bonding</i> Machine: <i>Al wedge-wedge (ACI) or Au ball-wedge (LPM)</i></p>	<p>Packaging achieved out of the CMI. (<i>PCB fabricated at ACI / wire bonding at ACI or LPM</i>)</p> 

Remarks concerning the wire bonding: The ball-wedge bonding will be performed manually at LPM (ultrasonic ball-wedge bonding with \varnothing 35 μm gold wire).

- An epoxy resin is used for PCB / Si bonding. Curing @ 150° for 15 min. A similar resin is used for globe-top packaging (protection of the wire bondings). The resin is dispensed with a syringe pump.
- Minimum size for the pads: 100 μm \times 100 μm .
- Pitch between the pads: > 100 μm (distance between pad centers).
- The ball has typically a diameter of \varnothing 50 μm .
- The PCB/silicon contact area should be at least 3 mm \times 5 mm. It is also possible to design a PCB with a shape that fits that of the silicon device.

Project : Micromotor
 Operator : Marc Stranczi / LMIS2
 Created : 26.06.2009 Last revision : 13.12.2010
 Substrates : SOI diam 100mm double side polished (Laser marking on the backside), orientation <100>, 50um Si / 2um oxide / 380um Si

Step N°	Description	Equipment	Program / Parameters	Target	Actual	Remarks	Name	Date
1 Metal Evaporation (FS)								
1.1	Aluminium evaporation	a) Leybold Optics LAB600H (Z4) or b) Alcatel EVA 600 (Z4)	100nm (1.000 kA°), a) HRN35 std recipe;239, b) electron beam configuration, crucible n°1 for Al, rotation speed 5, quartz program n° for Al thickness	Aluminium		Evaporation on the frontside with a Si thickness of 50um (laser mark on the backside, Si thickness of 350um) b) load the samples and wait min 3 hours for vacuum (about 1*10-6mbar)		
2 Photolithography Mask 1 (FS)								
2.1	Thermal dehydration	Memmert, gray oven on the right (Z6)	t=15min at 150°C			Used for metal dehydration		
2.2	Spin coat	Rite track 88 Series (Z1)	Thickness 2um; Recipe:C_AZ_92xx_2um_BSRonly			NO EBR (Edge Bead Removal)		
2.3	Photoresist Exposure	Süss MA6 double side mask aligner (Z6)	Mask 1, t=6.5sec; Al gap= 25um;Expose type=hard;Hard contact= 10um;WEC type=Contact;N2 purge=no;WEC offset= off			Best time exposure is 7 s with Ci1 source		
2.4	PR Develop	Rite track 88 Series (Z1)	Dev_AZ_92xx_2um			Process needs to be done with one wafer at a time to avoid the developer problem on te backside		
2.5	DI spin rinse and dry	Plade solvent wet bench (Z1)				Rinse directly after development to stop KOH effect on Si		
2.6	Microscope inspection							
3 Dry Etching Al (FS)								
3.1	Aluminium	STS Multiplex ICP (Z2)	t=40sec; 100nm etching of Al			Do not wait too much time before stripping to avoid Al migration or DI rinse and dry if stripping has to be done later		
3.2	Microscope inspection							

3.3	DI rinse and dry (optional)	UFT remover (Z2)	Rinse QDR bath, Dry in SRD				Do this step only if wafer is not clean	
4	Dry etching of Si (FS)							
4.1	Si etching	Alcatel AMS200 (Z2)	Depth:50um; t= 20min; SOI accurate ---- (Receipe)				Check website for etch rate, as etch rate of SiO2 is 20nm/mn it is better to add some time (about 2mn) to be sure to etch all Si (overetch)	
4.2	Microscope inspection							
5	Resist stripping							
5.1	Resist stripping	Wet bench (Z2)	remove new bath t=10min;old bath t= 10min					
5.2	Plasma O2	Tepla 300 (Z5)	t=5min at 500 W					
5.3	DI rinse and dry (optional)	UFT remover (Z2)	Rinse QDR bath, Dry in SRD				Do this step only if wafer is not clean	
6	Vapour HF (FS)							
6.1	SiO2 etching	Idonus HF VPE100 (Z5)	Depth / under etching : 4um, 35°C				(Box under etching), front side esposed to vapour, about 1h for 2um	
6.2	Microscope inspection						Blow N2 to check that structures are released	

MODAL ANALYSIS AND MODELING OF A FRICTIONLESS ELECTROSTATIC ROTARY STEPPER MICROMOTOR

M. Strancz¹, E. Sarajlic², G.J.M. Krijnen³, H. Fujita⁴, M.A.M. Gijs¹, and C. Yamahata¹

¹Laboratory of Microsystems, Ecole Polytechnique Fédérale de Lausanne (EPFL), SWITZERLAND,

²SmartTip B.V., Enschede, THE NETHERLANDS,

³MESA+, University of Twente, Enschede, THE NETHERLANDS,

⁴CIRMM, Institute of Industrial Science, The University of Tokyo, Tokyo, JAPAN

ABSTRACT

We present the design, modeling and characterization of a 3-phase electrostatic rotary stepper micromotor. The proposed motor is a monolithic device fabricated using silicon-on-insulator (SOI) technology. The rotor is suspended with a frictionless flexural pivot bearing and reaches an unprecedented rotational range of 30° ($\pm 15^\circ$) at 65 V. We have established a mechanical model of the deformation structure and performed finite element analysis (FEA) simulations of the dynamic properties. These studies are consistent with the extensive experimental characterization performed in the quasi-static, transient, and dynamic regimes.

INTRODUCTION

We have recently developed a piggyback stepper micromotor aimed at skew angle compensation in hard disk drives [1]. The mechanism of this frictionless motor is based on the monolithic “butterfly” pivot devised by Henein *et al.* [2,3]. With a reachable rotational range of $\pm 15^\circ$, this type of microactuator can be advantageously used in many MEMS applications. In this perspective, we have developed a mechanical model to optimize the static and dynamic responses of the motor. With this model, we have designed a new flexural bearing with a lower inertia and a higher out-of-plane stiffness. The improved design results in a very large displacement range, and an opening in the stator enables the inclusion of an arm required for microrobotic applications. In Figure 1, the arm is represented by a needle that indicates the angular displacement.

WORKING PRINCIPLE

The left schematic in Figure 1 shows the working principle and the main elements of the SOI electrostatic stepper micromotor. The motor consists of a 3-phase stator and a grounded rotor which is suspended by a flexural mechanism [2]. This frictionless bearing enables a rotational degree of freedom with a certain torsional stiffness. The stator electrodes are grouped into three pairs that are symmetrically located around the rotor (see the photograph in Figure 1). Each phase can be activated independently (voltages U_1 , U_2 and U_3). In the initial position, the electrodes of the first phase are perfectly aligned with the opposite electrodes on the rotor. The stator electrodes of the two other phases have a misalignment which is equal to $1/3$ of the pitch of the rotor electrodes.

MODELING

Flexural pivot stiffness

Using material mechanics theory, with the assumption that the material deformation is purely elastic and isotropic, we find that the stiffness of the 4-beam flexural pivot shown in Figure 1(right) is given by:

$$K_\theta = EI \frac{a^2 + al + 4(l^2 + 3lp + 3p^2)}{(l-a)(a^2 + al + l^2)}, \quad I = \frac{hb^3}{12}, \quad (1)$$

where E is the Young’s modulus of the beam material, h is the vertical height, b is the width of the flexure hinges, a is the length of the central reinforced structure, l is the total length of the beam elements, and p is their distance to the virtual center of rotation.

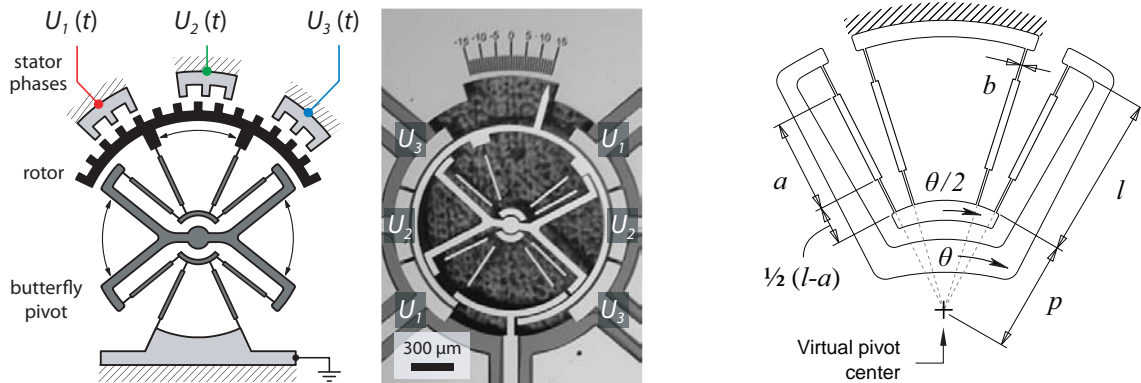


Figure 1: (left) Schematic principle of the 3-phase electrostatic stepper motor (actuated with voltages U_1 , U_2 , U_3). The internal “butterfly” structure mechanically connects the rotor to the chassis. (center) Micrograph of the fabricated SOI micromotor rotated clockwise by $+15^\circ$. (right) Schematic of a flexural pivot element consisting of four reinforced beams.



Figure 2: SolidWorks finite element modal analysis of the rotor's mechanical structure. The color levels describe the displacement magnitude relative to the anchor. From left to right, we show the first eigenmodes occurring at 170 Hz, 683 Hz and 2810 Hz, respectively. The first mode corresponds to the in-plane vibration of the rotor ring, while the second mode corresponds to the in-plane vibration of the internal butterfly pivot.

We verify that, in the case of thin flexure beams of length l ($a = 0$), equation (1) can be rewritten as [1,2]:

$$K_{\theta}|_{a=0} = \frac{4EI}{l} \left(1 + 3 \frac{p}{l} + 3 \frac{p^2}{l^2} \right). \quad (2)$$

On the other hand, when $p \rightarrow \infty$, one can find the stiffness of a folded-beam flexure with reinforced beams. Defining the tangential displacement $x \equiv p\theta$, we find the stiffness of the folded-beam linear guiding [3]:

$$K_x = \lim_{p \rightarrow \infty} \frac{K_{\theta}}{p^2} = \frac{12EI}{(l-a)(a^2 + al + l^2)}. \quad (3)$$

Finite element analysis

For the dynamic analysis of the mechanical structure, we have performed FEA simulations with SolidWorks Simulation software (SolidWorks 2009 SP5.0). Because of the crystallographic nature of silicon, the material has orthotropic elasticity. In our simulations, we have therefore used the orthotropic matrix representation of single-crystal silicon, using the parameters recommended by Hopcroft *et al.* [4]. The results of the modal analysis study are shown in Figure 2. For these simulations, we have considered flexure beams with a width of $1.15 \mu\text{m}$. This dimension, which is within the optical measurement uncertainty, was chosen so as to obtain the best match between the simulated result and the experimental data for the first eigenfrequency. With this

parameter, the first mode occurs around 170 Hz and corresponds to the in-plane vibration of the rotor ring, while the second mode occurs around 683 Hz and corresponds to the in-plane vibration of the internal butterfly pivot.

MICROFABRICATION RESULTS

The micromotor was fabricated in a two-mask process using standard SOI micromachining. Figure 3 shows scanning electron microscopy micrographs of a fabricated device. The fabrication process was performed on a (100)-oriented SOI wafer with a device layer of $50 \mu\text{m}$, a buried oxide layer of $2 \mu\text{m}$, and a handling substrate of $380 \mu\text{m}$. On the device layer, a 100 nm -thick aluminum layer was evaporated, then patterned by ICP (Surface Technology Systems, STS Multiplex ICP Etch). Subsequently, the device layer and the handling wafer were etched by DRIE (Adixen Dielectric and Silicon Etcher, AMS 200 DSE) using the Bosch process. After etching, the buried oxide beneath the rotor was removed using vapor HF (Idonus HF Vapor Phase Etcher, VPE-100). Finally, the silicon chip was mounted on a Printed Circuit Board and wire-bonded.

Note that the fabrication process could be straightforwardly simplified using a single-mask process, as we have demonstrated in an earlier paper [5]. However, such a fabrication process implies the use of honeycomb-like structures. Here, the selection of a two-mask process was motivated by the need for massive structures that can be

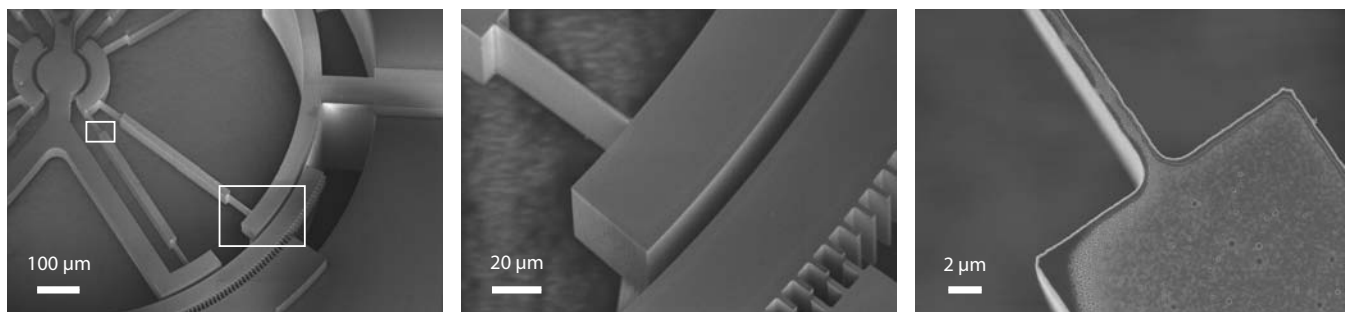


Figure 3: Scanning electron microscopy micrographs of a 3-phase electrostatic stepper micromotor fabricated with SOI technology. The dimensions of the flexure beams were estimated from these observations.

easily modeled analytically and simulated with FEA software.

EXPERIMENTAL RESULTS

Quasi-static and transient responses

In Figure 4, we show quasi-static measurements performed with a 3-phase sinusoidal driving sequence at 1 Hz. The maximum angular displacement increases quadratically with the applied voltage, as is expected for an electrostatic actuator [1].

Figure 5 is the transient response obtained by releasing the rotor from a small angle to its resting position. The damping coefficient and the first in-plane resonant frequency have been extracted from these data. Figure 6 exhibits a typical motion of the rotor rotated from 0° to $+9^\circ$. An angular speed of $1^\circ/\text{ms}$ could be reached with a driving signal of 600 Hz and 70 V amplitude. The measurements shown in Figures 5 and 6 were performed with a high-speed camera (Mikrotron CMOS high-speed camera, EoSens MC1363), using the algorithm described in [6].

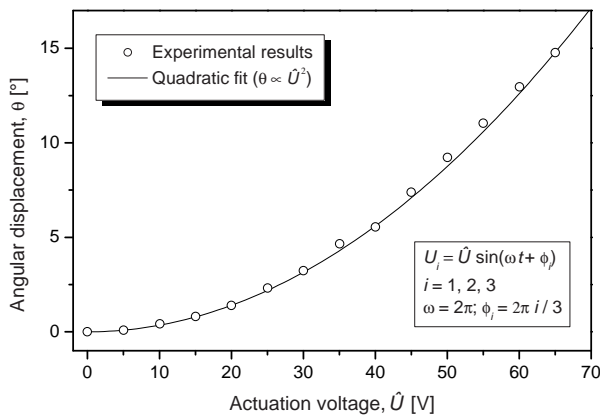


Figure 4: Maximum angular displacement of the stepper motor as a function of the driving voltage (3-phase sinusoidal excitation of 1 Hz). Data are for positive displacements only: The displacement range is double.

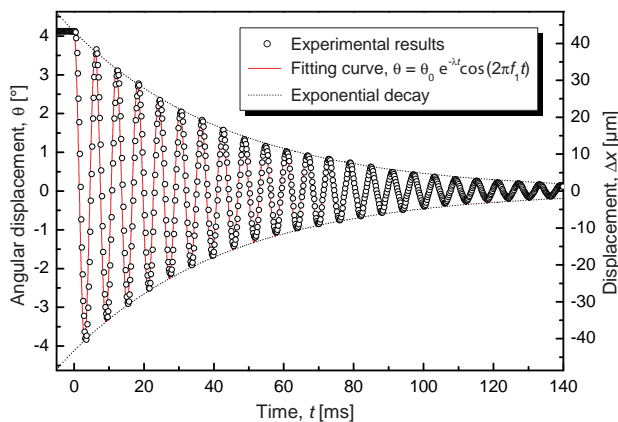


Figure 5: Step response of the rotor. The measurements were performed on the rotor's external ring. The first resonant frequency of 163 Hz can be extracted from the Fourier transform of these data.

Experimental modal analysis

We have performed a thorough in-plane and out-of-plane modal analysis of the structure with the Polytec Micro System Analyzer MSA-400. Figure 7 shows the in-plane data recorded by stroboscopic video microscopy under application of a swept excitation voltage on phase 2. The out-of-plane response (not shown in this abstract) was obtained by Laser-Doppler vibrometry. The results of the FEA simulations and the experimental modal analysis are summarized in Table 1. This table highlights the high conformity of the simulations for the first 5 modes (with a discrepancy lower than 10 %).

DISCUSSION

From the in-plane experimental modal analysis, we could retrieve the first two resonant frequencies f_1 and f_2 of the motor, which correspond to the eigenfrequencies of the rotor (f_1) and of the “butterfly” internal structure (f_2), as shown in the simulations of Figure 2.

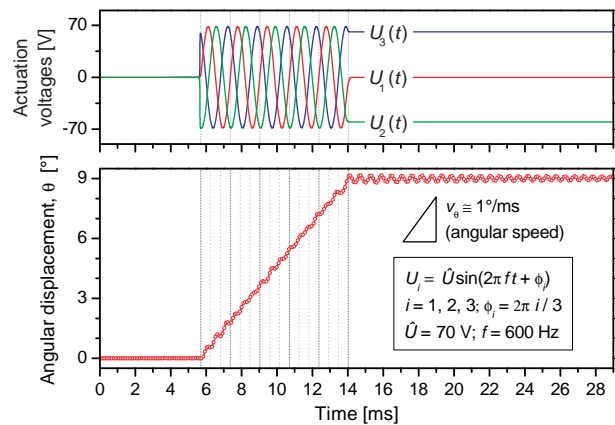


Figure 6: Typical recording of the angular displacement as a function of time. A 3-phase sinusoidal driving signal at 600 Hz and 70 V was applied, as illustrated in the upper part of the graph. With these settings, an angular speed of $1^\circ/\text{ms}$ was reached.

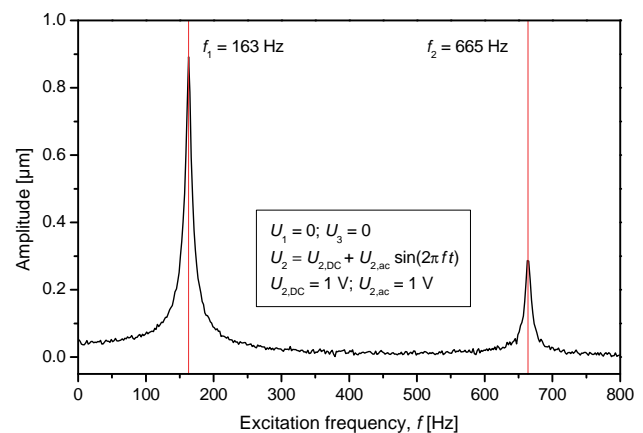


Figure 7: In-plane modal analysis of the micromotor recorded by stroboscopic video microscopy (Polytec MSA-400). These results are in line with the transient measurement of Figure 5.

Table 1: Design parameters and main modal properties of the micromotor. FEA simulations were obtained with SolidWorks Simulation software. Measurements were performed with the Polytec Micro System Analyzer MSA-400.

Main geometric characteristics		Modal analysis			
		Mode	FEA simulations	Experimental results	Remarks
SOI: (100) orientation*; 50 μm / 2 μm / 380 μm		1	170 Hz	163 Hz \pm 1 Hz	In-plane
Rotor diameter	1.4 mm	2	683 Hz	665 Hz \pm 1 Hz	In-plane
Flexure hinge width	$b = 1.5 \mu\text{m} \pm 0.4 \mu\text{m}$ **	3	2810 Hz	2616.4 Hz	Out-of-plane
No. of teeth per phase	80	4	5350 Hz	5018.0 Hz	Out-of-plane
Rotor / stator gap	2 $\mu\text{m} \pm 0.4 \mu\text{m}$	5	6110 Hz	5726.6 Hz	Out-of-plane

* The reader is referred to Table VI in [4] for the elastic modulus values of single-crystal silicon material.

** In the FEA simulations, we have used a beam width of 1.15 μm .

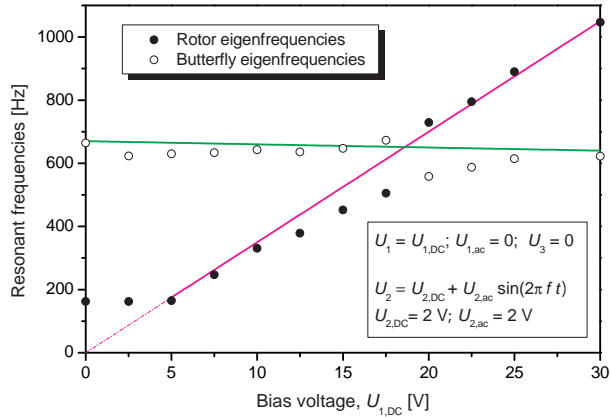


Figure 8: Illustration of the electrostatic stiffening. The rotor eigenfrequency increases when a DC voltage is applied on phase 1.

In Figure 8, we demonstrate that the first resonant frequency can be tuned by “electrostatic stiffening” [7]. The graph was obtained from data like those shown in Figure 7. When a DC voltage is applied on phase 1 ($U_1 = \text{const.}$) while the ac excitation is performed on phase 2, an electrostatic force tends to keep the rotor’s teeth aligned with phase 1. The rotor is directly affected by the stiffening while the butterfly – which is mechanically connected with flexure beams to the rotor (see Figure 1) – keeps its own degree of freedom, even when the rotor is firmly blocked. As a result, f_2 remains relatively constant while f_1 increases almost linearly with U_1 . This linear behavior is consistent with the equation of motion (see calculation of the electrostatic spring stiffness in [7]).

CONCLUSION AND OUTLOOK

With a displacement range of $\pm 15^\circ$, our micromotor opens perspectives in reliable and frictionless micrometer-scale displacement applications. It is a suitable candidate for a micromanipulator (e.g. bio-MEMS tweezers). Furthermore, the well understood and tunable dynamic response enables accurate micropositioning in microrobotics.

In Lausanne, we are currently working towards the optimization and implementation of several stepper motors for microrobotic applications. On the other side, in Tokyo, a

numerical analysis of the complete system consisting of the mechanical structure and the variable-capacitance actuation is performed [8].

ACKNOWLEDGMENTS

This research was partially supported by the Swiss National Science Foundation through its *Ambizione* funding program (Grant No. PZ00P2_121827).

The microfabrication was performed by Meena Kulkarni in the cleanroom of the EPFL Center of MicroNanoTechnology (CMi). The authors are thankful to the CMi staff for their technical and scientific support.

REFERENCES

- [1] E. Sarajlic, C. Yamahata, M. Cordero, H. Fujita, “Three-Phase Electrostatic Rotary Stepper Micromotor with a Flexural Pivot Bearing”, *J. Microelectromech. Syst.*, vol. 19, pp. 338-349, 2010.
- [2] S. Henein, P. Spanoudakis, S. Droz, L.I. Myklebust, E. Onillon, “Flexure Pivot for Aerospace Mechanisms”, in *Proc. 10th European Space Mechanisms & Tribology Symposium*, San Sebastián, Spain, 2003, pp. 285-288.
- [3] S. Henein, *Conception des guidages flexibles*, PPUR, Lausanne, Switzerland, 2004.
- [4] M.A. Hopcroft, W.D. Nix, T.W. Kenny, “What is the Young’s Modulus of Silicon?”, *J. Microelectromech. Syst.*, vol. 19, pp. 229-238, 2010.
- [5] E. Sarajlic, C. Yamahata, M. Cordero, L. Jalabert, T. Iizuka, H. Fujita, “Single Mask 3-Phase Electrostatic Rotary Stepper Micromotor”, in *Proc. 15th Int. Conf. on Solid-State Sensors, Actuators and Microsystems (Transducers ’09)*, Denver, USA, 2009 pp. 1505-1508.
- [6] C. Yamahata, E. Sarajlic, G.J.M. Krijnen, M.A.M. Gijs, “Subnanometer Translation of Microelectromechanical Systems Measured by Discrete Fourier Analysis of CCD Images”, *J. Microelectromech. Syst.*, vol. 19, pp. 1273-1275, 2010.
- [7] W.C. Tang, M.G. Lim, R.T. Howe, “Electrostatic Comb Drive Levitation and Control Method”, *J. Microelectromech. Syst.*, vol. 1, pp. 170-178, 1992.
- [8] J. Sone, T. Mizuma, M. Masunaga, S. Mochizuki, E. Sarajlic, C. Yamahata, H. Fujita, “Analysis of the Characteristics of a Rotary Stepper Micromotor”, *IEEEJ Trans. Sens. Micromach.*, vol. 130, pp. 310-316, 2010.